Simulations for the explosion and granular impact problems using the SPH method

by

Jian-Yu Chen

A thesis
presented to the University of Waterloo
in fulfillment of the
thesis requirement for the degree of
Doctor of Philosophy
in
Mechanical and Mechatronics Engineering

Waterloo, Ontario, Canada, 2019

Examining Committee Membership

The following served on the Examining Committee for this thesis. The decision of the Examining Committee is made by majority vote.

External Examiner	Dr. Luc Bauwens Professor, Mechanical and Manufacturing Engineering University of Calgary
Supervisor	Dr. Fue-Sang Lien Professor, Mechanical Engineering University of Waterloo
Internal Member	Dr. Duane Cronin Professor, Mechanical Engineering University of Waterloo
	Dr. Jean-Pierre Hickey Assistant Professor, Mechanical Engineering University of Waterloo
Internal-External Member	Dr. Francis Poulin Professor, Applied Mathematics University of Waterloo

Author's Declaration

I hereby declare that I am the sole author of this thesis. This is a true copy of the thesis, including any required final revisions, as accepted by my examiners.

I understand that my thesis may be made electronically available to the public.

Abstract

Simulations of explosions and granular impacts are challenging tasks to tackle using conventional mesh-based methods. In this thesis, a mesh-free technique called smoothed particle hydrodynamics (SPH) in conjunction with the Open-MP and CUDA parallel programming interfaces is introduced to tackle three-dimensional (3D) problems with large deformations.

Chapter 1 gives an introduction of the SPH method and a literature review of the theoretical improvement of SPH, landmine detonations, underwater explosions, and granular impacts. A research outline of the thesis is also presented at the end of this chapter. The basic ideas of the SPH method and some techniques which are relevant to improve the accuracy and stability of SPH, including the artificial viscosity, artificial stress, boundary implementation, neighboring particles search, and kernel gradient correction, are described in Chapter 2. In order to solve the governing equations, an elaboration of the constitutive models to update the stress tensor of soil and solid and the equation of states (EOSs) is given in Chapter 3.

The simulations of the detonation and granular impact problems using the SPH method are thoroughly presented in chapters 4-7. In Chapter 4, in order to tackle 3D problems with large number of particles, the in-house SPH code is parallelized by the Open-MP programming interface. The parallel efficiency is tested by the 3D shaped charge detonation. The simulations of the 2D soil explosion and its effects on structures are investigated in Chapter 5. Based on the parallelization of the SPH code and the simulation of 2D soil explosion, the physical process of the 3D landmine detonation is studied further. The simulations of the 3D underwater explosion within cylindrical rigid and aluminium (Al) tubes including cavitation phenomenon are presented in Chapter 6. The simulations of the 3D granular impacts using GPU acceleration are presented in Chapter 7. The numerical results of SPH are compared against the experimental and other available numerical data, and it is shown that the SPH method is capable of predicting landmine detonations, underwater explosions, and granular impacts.

The conclusions, novelties, and future plan of SPH research are summarized in Chapter 8.

Acknowledgements

First and foremost, I would like to express my sincere gratitude to my supervisor Professor Fue-Sang Lien for all his contributions of time, ideas, and funding to make my Ph.D research productive and stimulating. His patience for the students, enthusiasm for his research, and immense knowledge of computational fluid dynamics (CFD) are contagious and motivational to me, especially during the tough time of the Ph.D pursuit. I really appreciate the excellent example he has provided as a successful professor.

Besides my supervisor, I would like to thank Professor Eugene Yee, Dr. Chong Peng, Dr. Guang-Yu Wang, and Dr. Dian-Lei Feng, not only for their encouragements and insightful comments on the SPH research, but also for the hard questions which incented me to widen my research from various perspectives.

My sincere thank also goes to Dr. Qi-Hang Wu, Dr. Hang Meng, Dr. Huang-Rui Mo, and all the other members in our group for their precious supports and helpful discussions.

I would like to thank my wife Hui Li, my parents, brothers, and sisters for supporting me spiritually throughout my Ph.D career and my life in general.

Last but not the least, I would also like to thank my committee members, Professor Luc Bauwens, Professor Duane Cronin, Professor Jean-Pierre Hickey, and Professor Francis Poulin for serving as my committee members even at hardship. Your brilliant comments and suggestions related to my research are really appreciated. Thank you.

Table of Contents

List of Figures

List of Tables

List of Abbreviations

Acronym	Description
SPH	Smoothed Particle Hydrodynamics
DEM	Discrete Element Method
2D	Two Dimensional
PDE	Partial Differential Equation
EOS	Equation of State
HVI	High Velocity Impact
C-J	Chapman-Jouget
TNT	Trinitrotoluene
C4	Composition C-4
PETN	Pentaerythritol tetranitrate
Al	Aluminum
ALE	Arbitrary Lagrangian-Eulerian
RHS	Right Hand Side
LHS	Left Hand Side

Nomenclature

Characters

Symbol	Description	Unit
R_{ij}	distance between two particles	m
m	mass	kg
ρ	density	$\mathrm{kg} \cdot \mathrm{m}^{-3}$
$\boldsymbol{v}$	velocity vector	$\mathrm{m} \cdot \mathrm{s}^{-1}$
e	energy	$\mathrm{kg} \cdot \mathrm{m}^{2} \cdot \mathrm{s}^{-2}$
F	force	$\mathrm{kg} \cdot \mathrm{m} \cdot \mathrm{s}^{-2}$
p	pressure	$\mathrm{kg} \cdot \mathrm{m}^{-1} \cdot \mathrm{s}^{-2}$
$\boldsymbol{\sigma}$	stress tensor	$\mathrm{kg} \cdot \mathrm{m}^{-1} \cdot \mathrm{s}^{-2}$
$\boldsymbol{S}$	deviatoric stress tensor	$\mathrm{kg} \cdot \mathrm{m}^{-1} \cdot \mathrm{s}^{-2}$
$\dot{\boldsymbol{\varepsilon}}$	strain rate tensor	s^{-1}
$\dot{\boldsymbol{w}}$	spin rate tensor	s^{-1}
c	sound speed	$\mathrm{m} \cdot \mathrm{s}^{-1}$
E	Young's modulus	$\mathrm{kg} \cdot \mathrm{m}^{-1} \cdot \mathrm{s}^{-2}$
K	elastic bulk modulus	$\mathrm{kg} \cdot \mathrm{m}^{-1} \cdot \mathrm{s}^{-2}$
G	shear bulk modulus	$\mathrm{kg} \cdot \mathrm{m}^{-1} \cdot \mathrm{s}^{-2}$
T	temperature	K
$\boldsymbol{I}$	identity tensor	1
$\boldsymbol{\delta}$	Kronecker tensor	1

Operators

Symbol	Description
Ω	support domain of a given particle

∇	gradient operator
Δ	difference
$\otimes$	tensor product
O	order of magnitude

Chapter 1

Research Background

1.1 Introduction

Landmine detonations and underwater explosions are common threats in conflict areas all over the world. For example, the blast loading and soil throw of the landmine detonations can cause significant damage on human body such as spinal cord compression and brain damage. In order to understand these physical processes of explosive detonations, numerous experiments related to the landmine detonations and underwater explosions have been conducted by the previous researchers. Bergeron et al. conducted the detonation of 100-g charge of C4 explosive to study the basic explosion physics of shallow-buried charges and to generate a high-quality data set for the validation of computer codes [10]. Rigby et al. developed soil explosion apparatus and utilised Hopkinson pressure bars (HPBs) to measure the spatial pressure distribution from explosives buried in dry sand [1, 11]. Brett et al. measured the pressure distribution and employed high-speed video to record the dynamics of bubble formation and collapse in the interaction of an underwater explosion with a nearby steel cylinder [12]. However, in comparison with conducting experiments, computational simulation has increasingly become a very important approach for predicting the physical processes of soil and underwater explosions. As we know, experimental approaches have limited applications in complex problems due to its measurement difficulties, scaling difficulties, and configurations costs. Theoretical approaches are limited to simplified problems and provide ideal exact solutions as a reference. Compared to these two methods, numerical modeling has become a common practice for complicated industrial problems with the advent of computational hardware.

Grid-based methods, such as the finite difference method (FDM), finite volume method (FVM), and the finite element method (FEM), have been widely applied to various problems of computational fluid dynamics (CFD) and computational solid mechanics (CSM). Based on properly pre-defined mesh, the partial differential equations can be transformed to a set

of algebraic equations. Despite their broad applications, conventional methods suffer from some challenges and difficulties in some aspects. First of all, the distortion of mesh can generate computational crash especially in free surface, moving interface and extremely large deformation. Furthermore, the mesh generation can be time-consuming and difficult for problems with complicated geometries. The difficulties become more evident when simulating explosions and HVIs issues, as the feature such as large deformations existing in these phenomena is difficult for traditional methods to cope with. Therefore, a new generation of computational method - the meshfree method-has attracted significant attention over the past three decades. Numerous meshfree particle methods and their modified versions, such as the smoothed particle hydrodynamics (SPH) method, the peridynamics method, and the discrete element method (DEM), have been proposed to deal with the problems with large deformation. The grids are completely abandoned and replaced by particles which carry physical properties such as position, velocity, mass, energy, and stress. Consequently, the evolution of the fluid system can be governed by the interactions between particles, and the interface between different species can be easily tracked. In comparison with the conventional methods, these meshfree methods require no mesh in computation, and thus they can tackle large deformation problems like HVIs and crack propagation. For example, Rabczuk et al. proposed a simplified cracking meshfree particle method (CPM) for arbitrary evolving cracks, and the numerical results show that the CPM method can replicate crack paths and handle crack branching and fragmentation [13–17]. This thesis focuses on the simulations of the three-dimensional (3D) soil, underwater explosions, and granular impacts using the SPH method. The reasons are listed in the following: 1) The applications of the SPH method are wide, and it can tackle problems with extremely large deformation, free surface flow as well as moving interface. 2) The SPH method is quickly approaching its mature stage over the past three decades. The stability, accuracy and adaptivity of the SPH method have reached an acceptable level for practical use. 3) The particle methods bridge the gap between the continuum and fragmentation in a natural way. As a consequence, SPH is a suitable approach for the study of brittle fracture and subsequent fragmentation in damaged solids.

The SPH method is a Lagrangian method. Unlike the Eulerian method, the Lagrangian method concentrates on moving particles instead of the fixed spatial points (See Fig. 1.1). SPH has some special advantages in comparison with the traditional methods, which are listed as follows, 1) The time history of the moving particles can be obtained and the free surfaces, material interfaces can be tracked in the simulation process as SPH is a particle method of Lagrangian nature. 2) There is no grid/mesh work in SPH, which provides a straightforward strategy for large deformations, so these problems such as underwater explosions, HVIs are more suitably handled by the SPH method. 3) The SPH method is suitable to be parallelized using Open-MP or CUDA programming interface to obtain high computing performance.

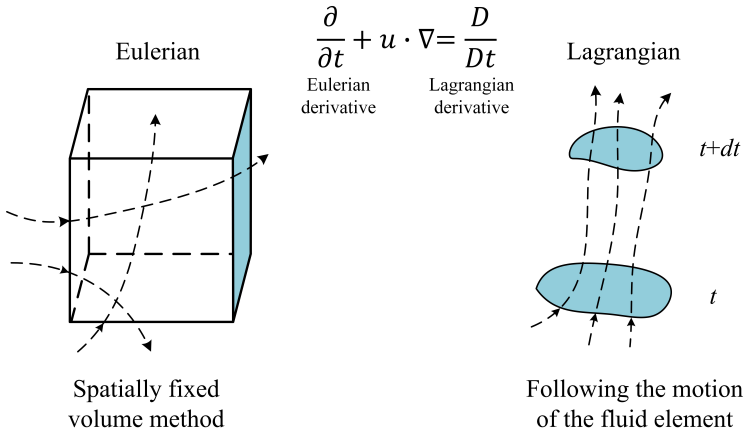

Figure 1.1 Eulerian and Lagrangian representation of fluid flow.

1.2 Literature review

SPH is a gridless numerical method which was presented by Monaghan and Lucy in 1977 independently [18, 19]. Although this approach was originally applied to simulate astrophysical problems, it has been used in a variety of problems and especially for multi-phase systems since the beginning of 1990s, as the change rates of variables in governing equations can be obtained through particle-particle interactions, which is inherently different from grid-based methods. Many researchers have investigated the theoretical issues of the SPH method. Swegle was the first person to study tensile instability of SPH in detail, which is particularly important for materials with negative pressure [20]. A variety of approaches have been proposed to tackle this problem. Morris noted that the stability property of the SPH method can be improved when the higher order spline interpolant approximation is used as the kernel function [21]. Monaghan gave a small repulsive term to eliminate the tensile instability problem while retaining the desirable SPH features [22]. Adams et al. used a variable background pressure to modify the particle transport velocity and remove the instability problem completely [23]. It is known that the accuracy of the conventional SPH is closely related to the selection of kernel function, particles distribution, and smoothing length evolution. Different approaches have been proposed to improve the accuracy of SPH. Liu et al. proposed the reproducing kernel methods (RKPM), in which an extra term is added to the traditional SPH interpolation kernel to exactly reproduce the constant, linear or higher order fields [24]. Chen et al. derived a corrective smoothed particle method, which resolved the general particle deficiency near or on the boundary and enhanced the solution accuracy not only on the boundary but also inside the problem domain [25]. Liu and Liu introduced the finite particle method (FPM) capable of accurately modeling higher order derivatives [26]. Shao et al. used the kernel gradient correction (KGC) to reduce particle

inconsistency and improved the accuracy of the SPH approximation [27]. The boundary treatment in the SPH method is also an open question and is of particular importance in numerical simulations. Enforcing impermeable boundary is essential in engineering applications. Since Monaghan's first SPH simulation for free surface flow, there have been many approaches for treating the boundary. These proposals can be grouped nearly into three types: 1) virtual particles; 2) repulsive particles; 3) boundary integrals [28]. For example, Adami et al. proposed a simple and generalized wall boundary condition which can address both stationary and moving walls of problems with complex geometries and shaped corners [29]. This technique has been incorporated into a well-known software package DualSPHysics. The above content is a brief description for the theoretical development of the SPH method. Fig. 1.2 presents crucial dates and important researchers who contributed greatly to the theoretical development and applications of the SPH method pertinent to the research topic in the thesis. The literature review for the applications of SPH on the landmine detonation, underwater explosion, and granular impacts is elaborated in the following.

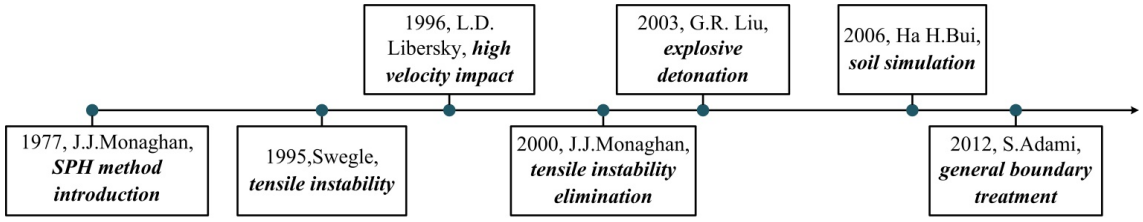

Figure 1.2 The historical development of the SPH method.

In the modeling and simulation of HVIs and explosive detonations, Libersky conducted the pioneering work on HVIs modelings using SPH [30, 31]. Johnson et al. also developed the numerical algorithms and materials models, such as the constitutive models of metals and concretes, for penetration and jet formation of the shaped charge computations [32]. Rabczuk et al. investigated the fragmentation of concrete due to explosive loading, which suggests that the SPH method can predict the damage of the concrete slabs [33–35]. In order to apply the SPH method to simulate landmine detonation problems, an appropriate soil constitutive model is essential. Maeda et al. firstly employed the SPH method to investigate the granular flow in conjunction with a non-linear elastic model [36]. Bui and his co-workers implemented elastoplastic constitutive model to the SPH framework to study plastic soil behavior, which can yield good results for the problems of soil failure and landslide [37]. Chen and Qiu conducted the simulation of column collapse of cohesionless granular with the SPH method [38]. Peng et al. employed the hypoplastic constitutive model to simulate geomechanics problems within the framework of SPH, which shows a good performance compared to analytical and experimental results [39, 40]. Fan and Li combined the peridynamics and the SPH methods and implemented three types of soil constitutive models to investigate the blast fragmentation of soil under buried explosives

[41–45]. The research revelant to dry granular flows using SPH have also been reported in [46, 47]. Recently, the SPH method has also been applied to simulate soil-structure interaction and rock explosion, which gives more realistic and accurate results for the geo-mechanical problems than the conventional method [48, 49]. Although many investigations of soil collapse simulations have been conducted, application of the SPH method in modeling and simulation of explosion in soil is still in its infancy. Our research group first developed an in-house SPH code to investigate 2D soil explosion and its effects on structures, and a general agreement between our SPH predictions and the experimental data can be observed. However, the 2D model is still of limited use for engineering applications. Thus, based on the 2D soil explosion research, another new soil constitutive model - the hypoplastic model which can capture some salient behaviors of soils is implemented, and the 3D soil explosion modeling using the Open-MP programming interface is established further. In comparison with the previous studies on soil fragmentation simulations, the modified SPH method in conjunction with the elastoplastic and hypoplastic constitutive models are employed to tackle the 3D landmine detonation for the first time.

In the field of underwater explosion issues, many research works in relation to the explosion simulations have been exploited using the grid-based methods. However, these grid-based numerical methods have a number of deficiencies in their ability to address explosion simulations. For example, the meshing and remeshing of the solution domain for explosion simulations are time-consuming. Moreover, extreme distortions of the mesh that may result in this remeshing can provoke numerical instabilities that can culminate in a program crash. In consequence, traditional numerical methods for explosion simulation are frequently augmented with various other strategies in order to resolve various numerical difficulties associated with the simulation. As an example of this approach [50], a boundary element method (BEM) such as the doubly asymptotic approximation (DAA) is used to simulate the movement of the water due to an explosion, whereas a FEM is used to model the effects of the explosion on the structure. Other strategies involve the combination of a Lagrangian and an Eulerian grid framework in which a Lagrangian mesh is used to track the material interface, while an Eulerian mesh is used to model the large deformations that characterize an underwater explosion [51, 52]. Zhang et al. [53] coupled a Runge-Kutta discontinuous Galerkin (RKDG) method with a FEM in order to investigate the cavitation problem induced in the near-field of an underwater explosion [53]. Recently, there has been a growing interest in the application of particle methods for explosion simulation, owing to the fact that these methods can track the changing material interface easily and, hence, are more applicable to addressing detonation problems involving large deformations. In our current research, the SPH method is used to address underwater explosion problems. In some seminal work, Swegel [54] investigated the feasibility of using the SPH method to simulate an underwater explosion and demonstrated that the SPH method can capture the shock wave and treat the large deformations that characterize detonation phenomenology

well. Liu, Liu and Lam [55] simulated air and underwater explosions using the SPH method. Zhao et al. [56] simulated underwater explosions and their effects on steel and reinforced concrete slabs using the SPH method. Zhang et al. [57] investigated bubble pulsing, jet formation, and shockwave propagation in an underwater explosion using a combination of the SPH method and BEM. Currently, SPH simulations of an underwater explosion are mostly limited to two-dimensional (2D) models. Although some 3D underwater explosion problems such as an axial symmetrical column charge detonation can be converted to a 2D problem and simulated using an axisymmetric SPH method, it is still difficult to address general 3D explosion problems using the SPH method, owing to the fact that these problems are extremely compute-intensive [57]. In view of this situation, our research group has developed a general 3D in-house SPH code [58, 59] based on a strategy described by Liu and Liu [60]. The Open-MP programming interface has been utilized in this code in order to reduce the computational time (viz., to improve significantly the computational efficiency of a simulation involving a large number of particles required for 3D underwater explosion simulations). To this purpose, we have applied this code to the simulation of an underwater explosion within a rigid cylinder and a deformable aluminum tube, including the phenomenon of cavitation for the first time using the SPH method. Furthermore, the 3D underwater explosion in a tube is simulated directly as a full 3D problem, rather than reducing it to a 2D problem by using a 2D cylindrical coordinate system as has been done in previous investigations [3, 4].

In addition to the explosion problems, the 3D granular impacts involving large deformation have also been investigated in the thesis. Recently, a number of experiments and simulations related to granular impacts have been conducted using a mesh-free methodology. This work concerning granular material impacts is of significant importance for various industrial applications including ink-jet printing and inpinging jet milling. Pacheco-Vázquez and Ruiz-Suárez [61] carried out impact cratering experiments using granular projectiles with different porosities. Ellowitz [62] investigated the phenomenon of two-dimensional (2D) head-on collisions of dense granular jets using discrete particle simulations . Shi et al. [7] studied the dynamic behavior of a dense granular jet impacting on a circular target using the Discrete Element Method (DEM) . To date, most of modeling effort concerning granular impact modeling have been conducted using the DEM method as described in Cundall and Strack [63]. While accurate, the DEM method involves solving Newton's equation of motion for each grain individually. In consequence, this method is computationally prohibitive for problems involving a large physical domain [9]. Although numerous investigations of the simulation of granular flows have been conducted, the application of the SPH methodology to the modeling and simulation of 3D granular impact is still in its infancy. In this thesis, the phase-change constitutive model will be incorporated into the SPH framework and used to investigate various phenomena associated with granular flow for the first time. This material constitutive model was recently proposed by Dunatunga and

Kamrin [9] who used it to investigate 2D granular flow problems within the material point method (MPM) framework. In comparison with the more commonly used rate-independent elastoplastic and Mohr–Coulomb models, the phase-change constitutive model is more suitable for addressing problems involving dense zones and rapid flows. Furthermore, the effects of particle size have also been incorporated into the phase-change constitutive model [9].

The search for the neighbors of a particle and the calculation of the rates of change of various physical variables are extremely time-consuming operations in the SPH methodology. As a consequence, the parallelization of the SPH methodology is necessary, especially for simulations of 3D granular dynamic behavior that necessarily involve large numbers of particles. The parallel efficiency of Open-MP used for the simulation of 3D explosion problems is still limited. Therefore, it is imperative to find an alternative parallel programming interface for SPH code so that the 3D large deformation problems can be simulated with higher computational efficiency. To this purpose, it is noted that CUDA, which is a parallel computing platform and programming interface for GPUs developed by NVIDIA, is especially well-suited for the efficient implementation of the SPH methodology. The implementation of the SPH methodology on GPUs was first described by Harada et al. [64]. Subsequently, Crespo et al. [65] reported GPU-accelerated SPH simulations for the investigation of complex free surface flows. These researchers showed that their SPH simulations on a single GPU were two orders of magnitude faster than that conducted on a single-core CPU. In this thesis, the CUDA programming interface has been used for the implementation of a new SPH code for simulation of granular flows on a GPU. The in-house parallelized SPH code has been implemented in C++ and designed specifically for the computationally efficient and accurate simulation of 3D granular impact problems involving large numbers of particles. To the best of our knowledge, this is the first time that the phase-change constitutive model has been incorporated in the SPH methodology and used to investigate the phenomenology associated with 3D granular impact problems. Furthermore, phenomena associated with 3D head-on collisions and the impact of granular jets with a wave structure on a granular film are modeled and simulated within the SPH framework for the first time.

In summary, the applications of the SPH method to large deformation problems have achieved numerous accomplishments, but nevertheless there are still a variety of problems listed below for us to tackle.

1) The granular flow problems have been well studied using SPH, but further research is required in the area of the soil explosion and granular impacts.

2) Although the underwater explosion phenomena have been studied by many researchers, the explosion within a water-filled cylindrical tube including cavitation and its effects on nearby solid structures still require further investigations.

3) The simulations of problems with complex geometries involving large number of particles require much computational time. To increase the computational efficiency and reliability

based on a serial code remains a challenge in the SPH method.
Therefore, to simulate the explosion and structure (soil, water and solid) interactions efficiently and effectively and clarify the mechanism in these multiphase and multiphysics problems are the main objective of the thesis, and these large deformation problems are of particular significance to the protection of human beings and property and development of national defense.

1.3 SPH Applications

The early applications of the SPH method were mainly focused on astrophysical phenomena and later extended to fluid dynamics problems. Historically, marine and costal engineering presents the primary utilizations of the SPH method because of the free surface of water and possible interaction with the costal structure [66, 67]. In aerospace engineering, ditching or water landing is one of the primary field which can be solved by the SPH method, as very large flow and structural deformations exist in these fluid-structural interactions. Car and tire industries are other important sectors where the SPH method is extensively employed due to the violent flow and the complex shape of free surface [68]. In industrial processing such as material forming, the SPH method provides capabilities to track the plastic strain, material fracture and composition due to its Lagrangian attribute [69]. Many environmental and geophysical problems include broad ranges of land motions, thus the SPH method is employed to simulate soil failure, debris flows, rockfalls, tsunami, earthquake, etc [70]. Furthermore, the SPH method has also been used in the simulation of motion of blood through vessels of the human circulation [71].

1.4 Challenges of the SPH method

Four grand challenges still exist in the SPH method: convergence, numerical stability, boundary conditions and adaptivity [72].
1) Convergence: convergence means that the numerical solution tends to theoretical solution when refining the discretization. Obtaining second-order convergence is one of the key challenges for the SPH method to be used in industrial applications.
2) Numerical stability: numerical instability is caused by undesirable properties of numerical algorithm. The main instabilities occurring in the SPH method are zero-energy modes, particle clumping and tensile instability.
3) Boundary conditions: initial and boundary conditions are important issues for solving a set of partial differential equations. How to initialize particles and assign accurately their properties, such as velocity and pressure, are the two main topics in initializing flow simulation. Free-slip, non-slip, periodic boundaries are boundary conditions with special

importance. Good development has been made over the last decades. Therefore, boundary conditions for the SPH method may not be considered as a difficult problem to date.
4) Adaptivity: The adaptive multi-resolution mesh refinement can be used effectively in grid-based methods, while such a well-established method is not available within the SPH method. Spatial resolution refinement in terms of effectiveness, efficiency and consistency is still a bottleneck that needs to be addressed properly before the method can be industrially established.

1.5 Research Outline

The research outline is clearly presented in Fig. 1.3, and the aim is primarily to conduct the simulations for the landmine detonation, the underwater explosion, and their effects on structures with satisfactory accuracy and high efficiency. The research work can be categorized into four parts. The first part is the validations of the explosive detonation model, soil constitutive model, and the HVI model using some benchmark problems. In order to tackle the 3D large deformation problems, the Open-MP parallel programming interface will be introduced and implemented for the optimization and acceleration of SPH simulations. Based on the validations of the models and the implementation of Open-MP, the 2D and 3D landmine detonations and their effects on structures will be investigated. In addition, the explosion in a water-filled tube including cavitation and its damage to structures will be conducted by combining the detonation model with the solid impact model. Finally, the 3D granular impacts using CUDA parallel computing platform are conducted.

The thesis is divided into seven chapters. In Chapter 1, the background of the SPH method and literature review have been thoroughly described. In addition, the features, development history, special advantages, applications, and challenges of the SPH method are briefly introduced. In Chapter 2, the main idea of the SPH method is presented and the governing Navier-Stokes equation is discretized to the summation form of the neighboring particles. Afterwards, some numerical techniques to tackle the issues such as tensile instability and accuracy are also given. Chapter 3 elaborates the constitutive models and EOSs used in all the simulations in this thesis. In order to solve the 3D detonation problems, the implementation details of the Open-MP parallel programming interface is presented in Chapter 4. The following chapters are the primary numerical results of the Ph.D thesis. Chapter 5 investigates the 2D soil explosion and its effects on structures and the 3D landmine detonation, respectively. In Chapter 6, the underwater explosion within rigid and deformable cylindrical tubes including cavitation is studied. The 3D granular impacts simulations are studied in Chapter 7. Some conclusion remarks, novelties, and future plan are given in Chapter 8.

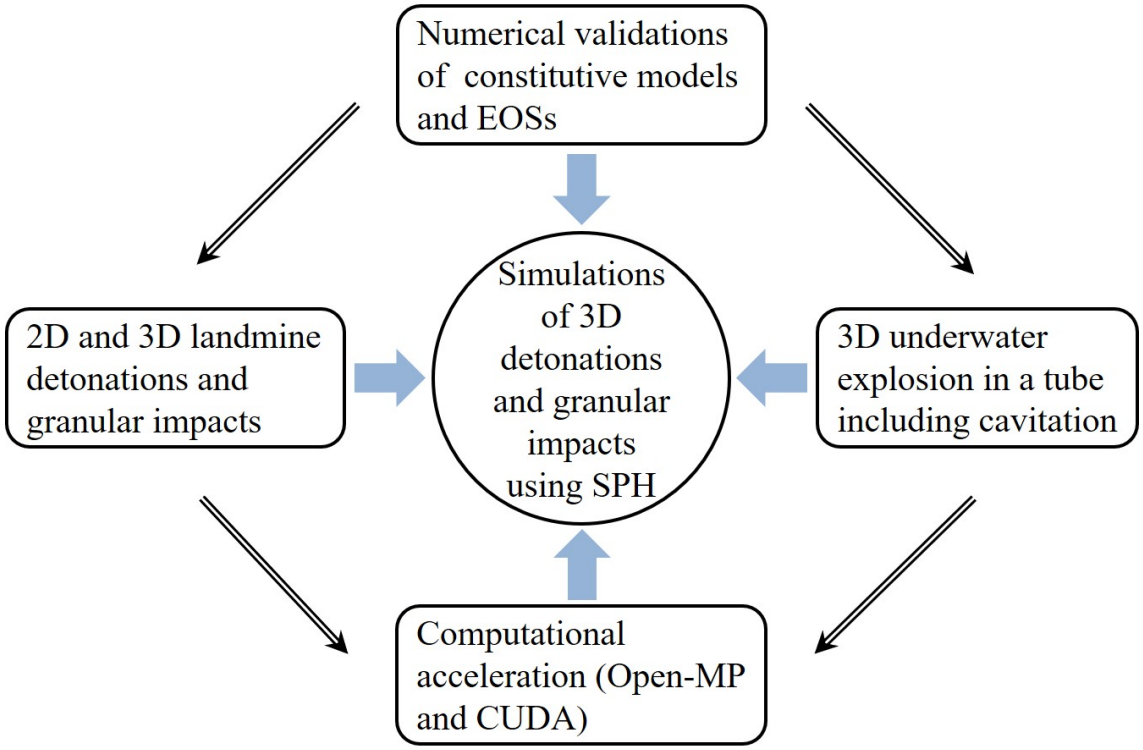

Figure 1.3 The outline of the SPH research.

Chapter 2

The basics of the SPH method

The conventional SPH method is a Lagrangian, meshfree solver developed for hydrodynamics problems in which the governing equations consist of partial differential equations (PDE). The principal feature of the SPH method is the use of statistical techniques with the objective of replacing the analytical formulations (PDEs) by a distribution of fluid elements for the physical properties. The derivation of the discretized PDE using SPH and some techniques to improve the stability and accuracy of SPH will be elaborated in the following.

2.1 Function approximation in SPH

The derivation of the SPH formulation can be basically divided into two parts. The first step is the kernel approximation, which transfers the functions to integral forms [60], and the function $f(\boldsymbol{x})$ and the function derivative $\nabla f(\boldsymbol{x})$ are approximated by

$$\langle f(\boldsymbol{x})\rangle = \int_{\Omega} f(\boldsymbol{x}')W(\boldsymbol{x}-\boldsymbol{x}',h)d\boldsymbol{x}' \,, \tag{2.1}$$

$$\langle \nabla f(\boldsymbol{x})\rangle = -\int_{\Omega} f(\boldsymbol{x}')\nabla W(\boldsymbol{x}-\boldsymbol{x}',h)d\boldsymbol{x}' \,, \tag{2.2}$$

where f is a function of vector $\boldsymbol{x}$, W is the kernel function, and h is the smoothing length. Ω is the integration domain. It can be found that the interpolant reproduces $f(\boldsymbol{x})$ exactly if the kernel is a delta function $\delta(\boldsymbol{x})$. In practice, the kernel function should statisfy three conditions. Firstly, the kernels are fucntions which tend to delta function as the smoothing lenth h tends to 0.

$$\lim_{h\to 0} W(\boldsymbol{x}-\boldsymbol{x}',h) = \delta(\boldsymbol{x}-\boldsymbol{x}') \,. \tag{2.3}$$

Secondly, they are normalized to 1 so that the constants are interpolated exactly.

$$\int_{\Omega} W(\boldsymbol{x}-\boldsymbol{x}',h)d\boldsymbol{x}' = 1 \,. \tag{2.4}$$

Thirdly, the kernels are effective only in the support domain of point $\boldsymbol{x}$.

$$W(\boldsymbol{x}-\boldsymbol{x}',h)=0, |\boldsymbol{x}-\boldsymbol{x}'|>kh\,, \tag{2.5}$$

where k is a constant of the smoothing function, and kh is the radius of the support domain of point $\boldsymbol{x}$. The second step of the SPH derivation is the particle approximation. The physical values of particle i can be approximated by the summation of particles in the support domain of particle i bestowed with volume, mass, density, and other hydrodynamics properties (see Fig. 2.1).

$$\langle f(\boldsymbol{x}_i)\rangle=\sum_{j=1}^{N} f(\boldsymbol{x}_j)W_{ij}V_j=\sum_{j=1}^{N} f(\boldsymbol{x}_j)W_{ij}\frac{m_j}{\rho_j}\,. \tag{2.6}$$

The particles approximation of function derivative $\nabla f(\boldsymbol{x})$ can be obtained in the same manner,

$$\langle \nabla f(\boldsymbol{x}_i)\rangle=-\sum_{j=1}^{N} f(\boldsymbol{x}_j)\nabla W_{ij}\frac{m_j}{\rho_j}\,, \tag{2.7}$$

in which, ρ_i, m_i, and V_i are density, mass, and volume of particle i, respectively. For convenience, $W_{ij}=W(\boldsymbol{x_i}-\boldsymbol{x_j},h)$.

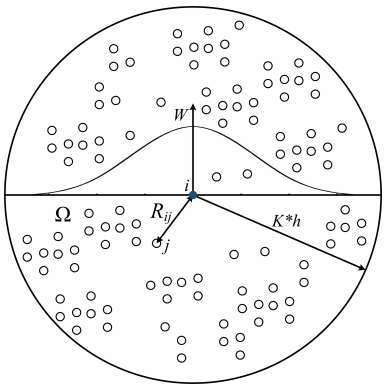

Figure 2.1 Particles approximation of the SPH method in a 2D problem; $K*h$ is the range of the support domain; R_{ij} is the distance between two particles.

2.2 Smoothing function

The choice of the interpolation kernel $W(\boldsymbol{x},h)$ is arbitrary for SPH. Plugging the taylor expansion of the $f(\boldsymbol{x})$ into Eq. (2.1) yields

$$\langle f(\boldsymbol{x})\rangle=\int_{\Omega}\left[f(\boldsymbol{x})+f'(\boldsymbol{x})(\boldsymbol{x}'-\boldsymbol{x})+\frac{1}{2!}f''(\boldsymbol{x})(\boldsymbol{x}'-\boldsymbol{x})^2+\cdots\right]W(\boldsymbol{x}-\boldsymbol{x}',h)d\boldsymbol{x}'\,. \tag{2.8}$$

In order to obtain results with nth order accuracy, the following "consistency equations" should be satisfied.

$$\int_{\Omega} W(\boldsymbol{x}-\boldsymbol{x}', h)d\boldsymbol{x}' = 1\,, \tag{2.9}$$

$$\int_{\Omega} W(\boldsymbol{x}-\boldsymbol{x}', h)(\boldsymbol{x}-\boldsymbol{x}')^{\otimes m}d\boldsymbol{x}' = 0, m \in [1, n]\,. \tag{2.10}$$

in which, $(\boldsymbol{x}-\boldsymbol{x}')^{\otimes m}$ represents the mth product of the vector $\boldsymbol{x}-\boldsymbol{x}'$. In our current research, the cubic spline kernel function W_3 below is adopted.

$$W_3(q,h) = \alpha_d \begin{cases} \frac{2}{3} - q^2 + \frac{1}{2}q^3 & 0 \le q < 1\,; \\ \frac{1}{6}(2-q)^3 & 1 \le q < 2\,; \\ 0 & q \ge 2\,, \end{cases} \tag{2.11}$$

in which q is the normalized distance between two particles and defined as $q = r/h$, and r is the Euclidean distance. α_d is a normalization factor, and the value is $15/(7\pi h^2)$ in two dimensions and $3/(2\pi h^3)$ in three dimensions. The cubic spline function conforms to the following conditions required in SPH: i) As the smoothing length $h \to 0$, W_3 approaches a delta function, ii) The cubic spline function has a compact support, and iii) $\int_{\Omega} W_3(\boldsymbol{x}-\boldsymbol{x}', h)d\boldsymbol{x}' = 1$ and $\int_{\Omega} W(\boldsymbol{x}-\boldsymbol{x}', h)(\boldsymbol{x}-\boldsymbol{x}')d\boldsymbol{x}' = 0$. We can recognize that the Eq. (2.9) is satisfied by the W_3, but Eq. (2.10) with $m > 1$ is a stronger constraint that is not satisfied by the W_3. Therefore, the numerical results obtained using cubic spline function should be second-order accurate theoretically. The smoothing length h of particle i in the detonation problems is updated using the following equation,

$$\frac{dh_i}{dt} = -\frac{1}{d}\frac{h_i}{\rho_i}\frac{d\rho_i}{dt}\,, \tag{2.12}$$

in which d is the dimension of a given problem and ρ_i is the density of particle i.

2.3 Discretized equations for Navier-Stokes (N-S) equation

Navier-Stokes equation contains continuity equation, momentum equation, and energy equation. For general fluid dynamics problems, the N-S equation is,

$$\begin{cases} \frac{d\rho}{dt} = -\rho\frac{\partial v^{\beta}}{\partial x^{\beta}}\,, \\ \frac{dv^{\alpha}}{dt} = \frac{1}{\rho}\frac{\partial \sigma^{\alpha\beta}}{\partial x^{\beta}}\,, \\ \frac{de}{dt} = \frac{\sigma^{\alpha\beta}}{\rho}\frac{\partial v^{\alpha}}{\partial x^{\beta}}\,. \end{cases} \tag{2.13}$$

As we know, a second-order stress tensor consists of a spherical part and a deviatoric part:

$$\sigma^{\alpha\beta} = -p\delta^{\alpha\beta} + S^{\alpha\beta}\,, \tag{2.14}$$

in which $-p\delta^{\alpha\beta}$ is the hydrostatic stress and $S^{\alpha\beta}$ is the deviatoric stress. With the basics of the SPH method mentioned above, the governing equations can be discretized in the following [60].

$$\begin{cases} \frac{\mathrm{d}\rho_i}{\mathrm{d}t} = \sum_{j=1}^{N} m_j v_{ij}^{\alpha} \cdot \frac{\partial W_{ij}}{\partial x_i^{\alpha}}\,, & (a) \\ \frac{\mathrm{d}v_i^{\alpha}}{\mathrm{d}t} = \sum_{j=1}^{N} m_j \frac{\sigma_i^{\alpha\beta} + \sigma_j^{\alpha\beta}}{\rho_i \rho_j} \frac{\partial W_{ij}}{\partial x_i^{\beta}}\,, & (b) \\ \frac{\mathrm{d}e_i}{\mathrm{d}t} = \frac{1}{2}\sum_{j=1}^{N} m_j \frac{p_i + p_j}{\rho_i \rho_j} v_{ij}^{\beta} \cdot \frac{\partial W_{ij}}{\partial x_i^{\beta}} + \frac{1}{2\rho_i} S_i^{\alpha\beta} \varepsilon_i^{\alpha\beta}, & (c) \\ p_i = p(\rho_i, e_i)\,, & (d) \end{cases} \tag{2.15}$$

where ρ_i, v_i, e_i, p_i, m_i are density, velocity, internal energy, pressure, and mass of particle i; $\frac{\mathrm{d}()}{\mathrm{d}t}$ is the time derivative of physical quantities; $v_{ij}^{\alpha} = v_i^{\alpha} - v_j^{\alpha}$. Equation (2.15 (d)) will be elaborated further in the next chapter. The derivation details of the discretized governing equations are given in appendix A [60].

2.4 Neighboring particle search

The computational efficiency of SPH depends directly on how to identify the neighboring particles. Three approaches including all pair search, linked list search, and tree search algorithms are popular for searching the nearest particles of a given particle (see Fig. 2.2). The all pair search approach calculates the distance from a given particle i to each particle j in a problem domain. If the distance is smaller than the dimension of the support domain of particle i, then the particle j is recorded as the nearest particle. In the implementation of the linked list algorithm, a temporary mesh is overlaid in the problem domain for a certain particle. Then the neighboring particles can only be found in the same grid cells or the immediate neighboring cells. The tree search algorithm is a very robust and efficient method for simulations of problems with large deformation. Therefore, the tree search algorithm is currently employed in our research to find the neighboring particles.

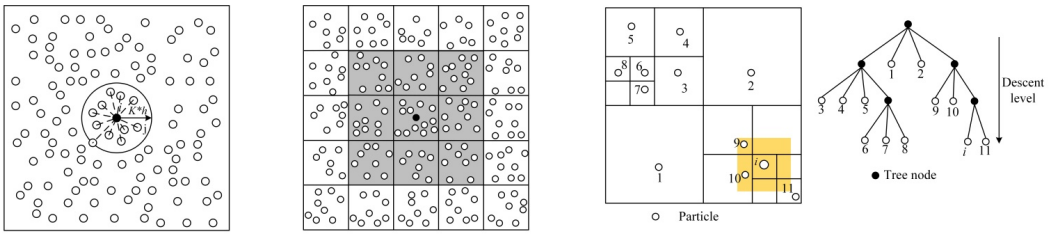

Figure 2.2 Nearest neighboring particle search approaches.

2.5 Artificial viscosity

The Monaghan type artificial viscosity [73] is incorporated into SPH in order to smooth potential unphysical oscillations, to prevent unphysical particle-particle penetration, and to stabilize the numerical solutions. This artificial viscosity assumes the following form:

$$\Pi_{ij} = \begin{cases} \frac{-\alpha c_{ij}\phi_{ij}+\beta\phi_{ij}^2}{\rho_{ij}}, & \boldsymbol{v_{ij}}\cdot\boldsymbol{x_{ij}} < 0\,; \\ 0\,, & \boldsymbol{v_{ij}}\cdot\boldsymbol{x_{ij}} \geq 0\,. \end{cases} \tag{2.16}$$

Here, $\phi_{ij} = \frac{h_{ij}\boldsymbol{v_{ij}}\cdot\boldsymbol{x_{ij}}}{|\boldsymbol{x_{ij}}|^2+(\varphi)^2}$, $c_{ij} = \frac{1}{2}(c_i + c_j)$, $\rho_{ij} = \frac{1}{2}(\rho_i + \rho_j)$, $h_{ij} = \frac{1}{2}(h_i + h_j)$, $\boldsymbol{v_{ij}} = \boldsymbol{v_i} - \boldsymbol{v_j}$, and $\boldsymbol{x_{ij}} = \boldsymbol{x_i} - \boldsymbol{x_j}$, where c_i is the speed of sound associated with particle i; α and β are constant coefficients that are set to have values of 1.0 and 10.0, respectively; and, $\varphi = 0.1h_{ij}$ is applied in order to prevent the unphysical overlapping of two particles. Thus the momentum equation should be modified as,

$$\frac{\mathrm{d}v_i^\alpha}{\mathrm{d}t} = \sum_{j=1}^{N} m_j\left(\frac{\sigma_i^{\alpha\beta} + \sigma_j^{\alpha\beta}}{\rho_i\rho_j} + \Pi_{ij}\delta^{\alpha\beta}\right)\frac{\partial W_{ij}}{\partial x_i^\beta}\,. \tag{2.17}$$

This formulation of viscosity is capable of capturing 1-D shock phenomena. The success of the Monaghan artificial viscosity can be attributed to the pari-wise formulation [74]. However, the viscosity will be triggered and add dissipation as long as $\boldsymbol{v_{ij}}\cdot\boldsymbol{x_{ij}} < 0$, and there will be times when $\boldsymbol{v_{ij}}\cdot\boldsymbol{x_{ij}} < 0$, the viscosity will be activated even though no compression occurs. Therefore, the artificial viscosity limiter has been developed recently in [74] to limit the SPH artificial viscosity. They accomplish this by replacing the velocity jump $\boldsymbol{v_{ij}}$ with a linearly extrapolated velocity jump. In our current research, only the Monaghan type artificial viscosity is employed, and the viscosity limiter will be implemented and compared with the Monaghan type artificial viscosity in the near future.

2.6 Boundary conditions

The imposition of boundary conditions is a challenge in the SPH method. Various methodologies have been proposed for the imposition of boundary conditions in SPH simulations [29, 30, 66]. Generally, there are two basic concepts of the wall models for SPH simulations. In one concept, the repulsion forces are introduced to prevent particles crossing the interface or the boundary. For example, Monaghan used a set of virtual particles on the boundary to produce a repulsive force to the real particles and prevent real particles from penetrating through the boundary. The force per unit mass p_{ij} has a Lennard-Jones form, but equals to zero if $r_{ij} > r_0$ so that the force is purely repulsive [66].

$$p_{ij} = \begin{cases} D\left[\left(\frac{r_0}{r_{ij}}\right)^{n_1} - \left(\frac{r_0}{r_{ij}}\right)^{n_2}\right]\frac{x_{ij}}{r_{ij}^2}, & \left(\frac{r_0}{r_{ij}}\right) > 1\ ; \\ 0\ , & \left(\frac{r_0}{r_{ij}}\right) \leq 1\ . \end{cases} \tag{2.18}$$

where n_1 and n_2 are set to be 12 and 4, respectively.

Another concept is to fill the boundary walls with virtual particles to ensure that the support domain of a given particle near the boundary is completely covered with particles. Libersky first introduced virtual particles to reflect a symmetrical boundary condition. For the free slip boundary condition, the physical variables of the virtual particles are set according to the following relations [30].

$$\begin{cases} x_v = 2x_w - x_r, y_v = 2y_w - y_r\ ; \\ v_{v,t} = v_{r,t}, v_{v,n} = -v_{r,n}\ ; \\ p_v = p_r, \rho_v = \rho_r\ . \end{cases} \tag{2.19}$$

For the non-slip boundary condition, both the tangential and normal velocities of the virtual particles are reversed.

$$\begin{cases} x_v = 2x_w - x_r, y_v = 2y_w - y_r\ ; \\ v_{v,t} = -v_{r,t}, v_{v,n} = -v_{r,n}\ ; \\ p_v = p_r, \rho_v = \rho_r\ . \end{cases} \tag{2.20}$$

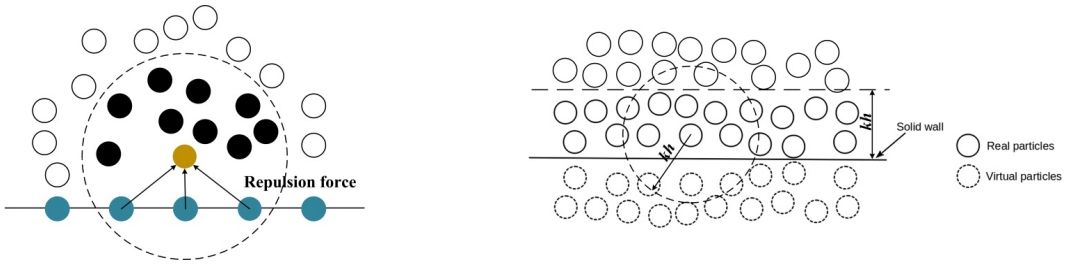

Figure 2.3 Monaghan (left side) and Libersky (right side) types of virtual particles distribution.

In this thesis, dummy particles are employed to impose the no-slip solid boundary condition at the walls of the rigid cylinder within which the explosion occurs (see Fig. 2.4). The velocity of the solid wall boundary $\boldsymbol{v}_w$ is assigned to the velocity of the dummy particles $\boldsymbol{v}_d$ (viz., $\boldsymbol{v}_d = \boldsymbol{v}_w$). For the calculation of the rate of change of a physical quantity associated with a real particle κ, the components of the stress tensor of the dummy particles are extrapolated using the values of the neighboring granular particles, so

$$\sigma_d^{ij} = \frac{\sum_{\kappa=1}^{N} \sigma_\kappa^{ij} W(r_{d\kappa}) - (g^i - a_d^i) \sum_{\kappa=1}^{N} \rho_\kappa r_{d\kappa}^i W(r_{d\kappa}) \delta^{ij}}{\sum_{\kappa=1}^{N} W(r_{d\kappa})}, \tag{2.21}$$

where subscripts d and κ are used to denote the dummy and granular particles, respectively. Moreover, $\boldsymbol{a}_d$ is the prescribed acceleration of the dummy particles; $\boldsymbol{g}$ is the gravitational acceleration; $\boldsymbol{r}_{d\kappa}$ is the displacement vector from the granular particle κ to the dummy particle d; $r_{d\kappa}$ is the Euclidean distance between the granular particle κ and the dummy particle d, so $r_{d\kappa} = ||\boldsymbol{r}_{d\kappa}||$; δ^{ij} is the Kronecker delta function (equivalent to the identity matrix in three dimensions); and, N denotes the number of granular particles within the support domain (taken to be a spherical region with a radius that is some multiple k of the kernel smoothing length h) of the dummy particle d.

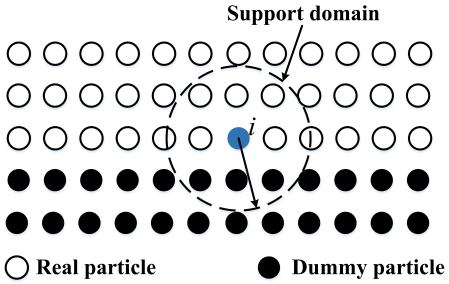

Figure 2.4 Depiction of the imposition of the no-slip boundary condition along a solid surface in SPH using dummy particles.

2.7 Impact force calculation

When calculating the impact force of a granular material on the boundary, we first use the extrapolated stresses of the dummy particles given above to determine the interaction force on each dummy particle through application of the momentum equation as follows [75]:

$$F_d^\alpha = m_d \sum_i m_i \left(\frac{\sigma_i^{\alpha\beta} + \sigma_d^{\alpha\beta}}{\rho_d \rho_i} + \Pi_{di} \delta^{\alpha\beta} \right) \frac{\partial W_{di}}{\partial x_d^\beta}. \tag{2.22}$$

Following this calculation, the impact force F_W exerted on the solid wall boundary can be calculated as the summation of the forces $\boldsymbol{F}_d$ on the dummy particles, so

$$F_W = \sum_d \sum_i m_d m_i n^\alpha \left(\frac{\sigma_i^{\alpha\beta} + \sigma_d^{\alpha\beta}}{\rho_d \rho_i} + \Pi_{di} \delta^{\alpha\beta} \right) \frac{\partial W_{di}}{\partial x_d^\beta} , \tag{2.23}$$

where the subscripts i and d denote the granular and dummy particles, respectively; and, $\boldsymbol{n}$ is the normal vector to the solid wall boundary.

2.8 Interface treatment

When using the SPH method to simulate the entire process of landmine detonation and its effects on structures, the major challenge is the treatment for the interfaces of multi-materials (see Fig. 2.5). The summation allows contributions from particles of different materials for a given particle near the interface. Two types of equations can be used for the density change rate calculation in soil explosion. One is

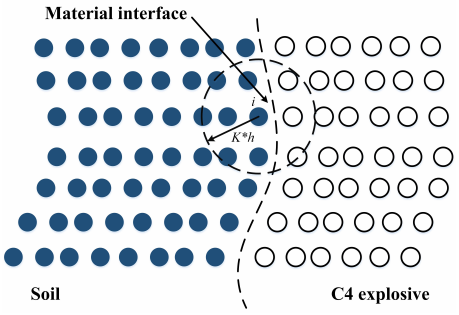

Figure 2.5 Soil and explosive particles near the interface.

$$\frac{\mathrm{d}\rho_i}{\mathrm{d}t} = \sum_{j=1}^{N} m_j (v_i^\alpha - v_j^\alpha) \frac{\partial W_{ij}}{\partial x_i^\alpha} , \tag{2.24}$$

another one is

$$\frac{\mathrm{d}\rho_i}{\mathrm{d}t} = \rho_i \sum_{j=1}^{N} \frac{m_j}{\rho_j} (v_i^\alpha - v_j^\alpha) \frac{\partial W_{ij}}{\partial x_i^\alpha} . \tag{2.25}$$

The Eq. (2.24) is more stable and accurate than Eq. (2.25) when tackling problems with density ratio less than 2. However, some unphysical values will occur during the computation with the Eq. (2.24) in landmine detonation, as the density ratio near the interface among the explosion gas, soil and structures is extremely large, and the expression (2.25) is more accurate than Eq. (2.24) for the systems involving two or more fluids with large

density ratios in contact. This is because near the interface, the summation form of $\nabla \cdot v$ for one type of SPH fluid particle involves contributions from the other fluid. If we imagine the one fluid field with exactly the same velocity, particle positions as the other fluid, but different density, we still want to obtain the same estimation of $\nabla \cdot v$ for these two fluids. However, the estimate will be different when using Eq. (2.24) as the mass elements are different. But the estimate of $\nabla \cdot v$ will be the same when using Eq. (2.25) because the ratio of mass to density is used [76]. Monaghan found that both of these two equations are suitable for the fluids with density ratio less than 2, whereas it is better to use Eq. (2.25) when the density ratio across the interface is larger than 2 [76]. In order to tackle the multiphase problems with high density ratio, the Eq. (2.25) can be used to calculate the density change rate near the multiphase interface, while the Eq. (2.24) can be applied for the particles in the single phase. Thus the continuity equation is required to be modified by combining these two equations (2.24) and (2.25) near the interface [77]:

$$\frac{\mathrm{d}\rho_i}{\mathrm{d}t} = \sum_{j=1}^{N} \frac{\rho_i + \psi_i \rho_j}{(1+\psi_i)\rho_j} m_j (v_i^\alpha - v_j^\alpha) \frac{\partial W_{ij}}{\partial x_i^\alpha} , \tag{2.26}$$

where $\psi_i = \frac{1}{lnk_i}$. $k_i = \frac{\rho_{i,\max}}{\rho_{i,\min}}$, in which $\rho_{i,\max}$ and $\rho_{i,\min}$ are the particles with maximum and minimum densities in the support domain of particle i, respectively.

The Eq. (2.26) can be reduced to Eq. (2.24) when $k_i \to 1$ or $\psi_i \to \infty$. Otherwise, the Eq. (2.26) will be simplified to Eq. (2.25) when $k_i \to \infty$ or $\psi_i \to 0$. In this way, the density change rate in different phases can be calculated adaptively.

2.9 Artificial stress

Despite the growing popularity of the SPH method, it suffers from the tensile instability. When the solid is stretched, the SPH particles attract each other. However, unlike the behavior of atoms in solid, the attraction force can culminate in an instability which shows up as praticles forming small clumps. This instability was first investigated by Swegle et al., who related it to the negative pressure and the second derivative of the kernel function in the SPH method [20]. There have been a number of approaches to remove the tensile instability [23, 78, 79]. In the thesis, the Monaghan-type artificial stress is applied to the current research. The components of artificial stress of particle i for two-dimensional problems are

$$\begin{cases} R_i^{xx} = \cos^2\theta_i \overline{R}_i^{xx} + \sin^2\theta_i \overline{R}_i^{yy} , \\ R_i^{yy} = \sin^2\theta_i \overline{R}_i^{xx} + \cos^2\theta_i \overline{R}_i^{yy} , \\ R_i^{xy} = \sin\theta_i \cos\theta_i (\overline{R}_i^{xx} - \overline{R}_i^{yy}) . \end{cases} \tag{2.27}$$

The principal component $\overline{R}_i^{xx}$ is calculated by the following equation, which also applies for $\overline{R}_i^{yy}$.

$$\begin{cases} \overline{R}_i^{xx} = -\epsilon \frac{\overline{\sigma}_i^{xx}}{\rho^2} & (\overline{\sigma}_i^{xx} > 0)\,; \\ 0 & (\text{otherwise})\,, \end{cases} \tag{2.28}$$

ϵ is a constant parameter ranging from 0 to 1. The new components of stress tensor in rotated frame are determined by:

$$\begin{cases} \overline{\sigma}_i^{xx} = \cos^2\theta_i \sigma_i^{xx} + 2\sin\theta_i \cos\theta_i \sigma_i^{xy} + \sin^2\theta_i \sigma_i^{yy}\,; \\ \overline{\sigma}_i^{yy} = \sin^2\theta_i \sigma_i^{xx} + 2\sin\theta_i \cos\theta_i \sigma_i^{xy} + \cos^2\theta_i \sigma_i^{yy}\,. \end{cases} \tag{2.29}$$

The rotation angle θ_i is defined by:

$$\tan 2\theta_i = \frac{2\sigma_i^{xy}}{\sigma_i^{xx} - \sigma_i^{yy}}\,. \tag{2.30}$$

Thus the artificial stress can be added to particle approximation of the momentum equation:

$$\frac{\mathrm{d}v_i^\alpha}{\mathrm{d}t} = \sum_{j=1}^{N} m_j \left(\frac{\sigma_i^{\alpha\beta} + \sigma_j^{\alpha\beta}}{\rho_i \rho_j} + \Pi_{ij}\delta^{\alpha\beta} + f_{ij}^n (R_i^{\alpha\beta} + R_j^{\alpha\beta})\right) \frac{\partial W_{ij}}{\partial x_i^\beta}\,, \tag{2.31}$$

where the exponent $n > 0$, f_{ij} is the repulsive term in terms of the kernel:

$$f_{ij} = \frac{W_{ij}}{W(\Delta d)}\,, \tag{2.32}$$

where Δd denotes the initial particle spacing.

2.10 The correction of kernel gradient

The second-order accuracy of the interior region is ensured by the continuous kernel interpolation of Eq. (2.1), which means the constant and linear functions can be reproduced exactly. However, this C^1 consistency is not always satisfied due to the irrigular distributions of particles and the deficiency near the boundary, which may lead to relatively low accuracy of the conventional SPH method. A variety of corrective procedures have been proposed to improve the particle inconsistency and accuracy of the kernel-based approximations [24, 27, 40]. In the thesis, the kernel gradient correction [80] is applied to enforce C^1 consistency, and is given as follows,

$$\nabla_i^C W_{ij} = L(r_i) \nabla_i W_{ij}\,, \tag{2.33}$$

in which, $\nabla_i^C W_{ij}$ is the corrected kernel gradient; $L(r_i)$ is the renormalization matrix. For the 3D problem simulations,

$$L(r_i) = \begin{pmatrix} \sum_{j=1}^{N} x_{ji} \frac{\partial W_{ij}}{\partial x_i} \frac{m_j}{\rho_j} & \sum_{j=1}^{N} x_{ji} \frac{\partial W_{ij}}{\partial y_i} \frac{m_j}{\rho_j} & \sum_{j=1}^{N} x_{ji} \frac{\partial W_{ij}}{\partial z_i} \frac{m_j}{\rho_j} \\ \sum_{j=1}^{N} y_{ji} \frac{\partial W_{ij}}{\partial x_i} \frac{m_j}{\rho_j} & \sum_{j=1}^{N} y_{ji} \frac{\partial W_{ij}}{\partial y_i} \frac{m_j}{\rho_j} & \sum_{j=1}^{N} y_{ji} \frac{\partial W_{ij}}{\partial z_i} \frac{m_j}{\rho_j} \\ \sum_{j=1}^{N} z_{ji} \frac{\partial W_{ij}}{\partial x_i} \frac{m_j}{\rho_j} & \sum_{j=1}^{N} z_{ji} \frac{\partial W_{ij}}{\partial y_i} \frac{m_j}{\rho_j} & \sum_{j=1}^{N} z_{ji} \frac{\partial W_{ij}}{\partial z_i} \frac{m_j}{\rho_j} \end{pmatrix}^{-1} , \tag{2.34}$$

in which, $x_{ji} = x_j - x_i$, $y_{ji} = y_j - y_i$, and $z_{ji} = z_j - z_i$. The derivation detail of the correction of kernel gradient is given in Appendix B.

2.11 Explicit time integration

Equations (2.15 (a)), (2.15 (b)), and (2.15 (c)) are integrated using the standard Leapfrog method to update the density ρ, velocity v, and energy e:

$$\rho_{n+1/2} = \rho_{n-1/2} + \Delta t \left(\frac{d\rho}{dt} \right)_n , \tag{2.35}$$

$$v^{\alpha}_{n+1/2} = v^{\alpha}_{n-1/2} + \Delta t \left(\frac{dv^{\alpha}}{dt} \right)_n , \tag{2.36}$$

$$e_{n+1/2} = e_{n-1/2} + \Delta t \left(\frac{de}{dt} \right)_n , \tag{2.37}$$

$$x^{\alpha}_{n+1} = x^{\alpha}_n + \Delta t v^{\alpha}_{n+1/2} , \tag{2.38}$$

where x is the coordinate of particles; Δt is the time step; n denotes the current calculation step.

In addition, the CFL (Courant-Friedichs-Levy) condition, governing the stability of the Leapfrog method, should be satisfied by the following time step:

$$\Delta t \leq 0.2(h/c) , \tag{2.39}$$

in which c is the sound speed. In this thesis, the sound speed of the soil and solid is calculated by $c = \sqrt{E/\rho}$, where E is the Young's modulus and ρ is the density, respectively. The sound speed of the compressible fluids is calculated by $c = \sqrt{\frac{\partial p}{\partial \rho}}$, where p is the pressure.

2.12 The solution procedure of SPH

The solution procedure of the SPH method can be split into three main steps. The first step is the generation of boundary particles and neighboring particles search for each particle in the problem domain. The second step is to solve the change rates of physical properties in the continuity, momentum, and energy equations. The calculations of deviatoric stress tensor $\boldsymbol{S}$ and the hydrostatic pressure p in the governing equations are given in the next chapter in detail. The third step is updating the physical quantities at the given time step and marching these steps in an iterative manner before reaching the maximum time steps. The main solution procedure for the SPH method is shown in Fig. 2.6. The present in-house code is based on the sample code provided by Liu and Liu [60].

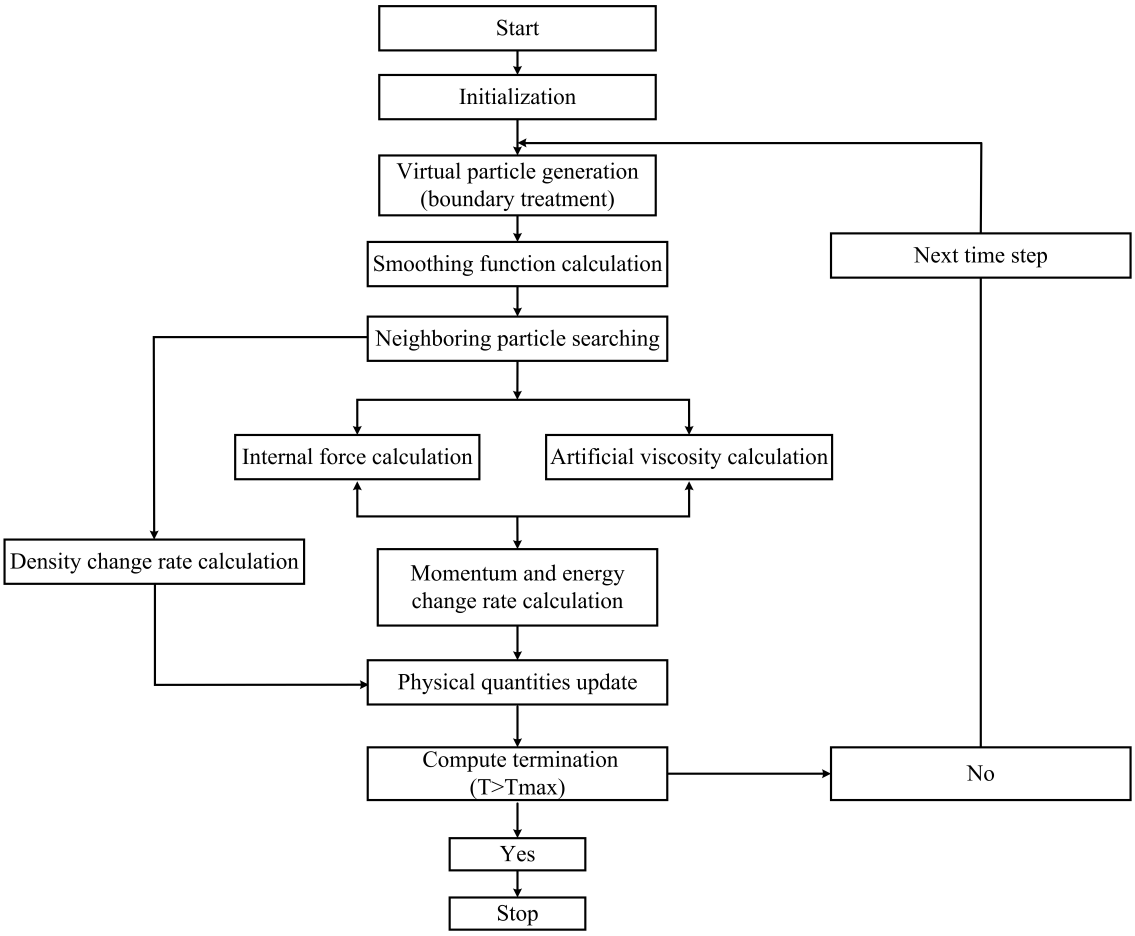

Figure 2.6 The SPH algorithm of the detonation problems.

2.13 Summary

In this chapter, the main feature and basic concepts for the SPH method have been presented. Then the Navier-Stokes equation is discretized to the summation form of neighboring particles. In addition, the artificial viscosity, boundary condition treatment, time integration method, artificial stress, correction of kernel gradient, neighboring particles search, and interface treatment for multi-materials have been introduced to improve the accuracy and stability of SPH. At the end, the solution procedure of the in-house SPH code is shown by a flow chart.

Chapter 3

The constitutive models and EOSs

The basic ideas of the SPH method have been presented in Chapter 2. In order to solve the governing equations, the consitutive models including the elastoplastic, hypoplastic, and phase-change models to describe the dynamic behaviors of the soil, the elastic perfectly plastic constitutive model to update the stress tensor in HVIs, and the equation of states (EOSs) of the explosive detonation, compressible water, and solid impact are elaborated in this chapter.

3.1 Soil constitutive models

A constitutive equation is required in order to calculate the stress tensor $\boldsymbol{\sigma}$ and to close the governing equations. Towards this objective, the stress tensor is decomposed into two parts as follows:

$$\sigma^{\alpha\beta} = -p\delta^{\alpha\beta} + S^{\alpha\beta}\,, \tag{3.1}$$

where $-p$ and $\boldsymbol{S}$ are the pressure and the deviatoric stress tensor, respectively. Normally, the pressure $-p$ is calculated using an EOS, while the deviatoric stress $\boldsymbol{S}$ is obtained through a constitutive equation. However, in the simulations of the dynamical behavior of soil conducted herein, the stress tensor $\boldsymbol{\sigma}$ is calculated directly using a constitutive equation and, subsequently, the pressure is obtained from the mean stress without having to use an EOS. More specifically,

$$p = -\frac{\sigma^{\alpha\alpha}}{3} = -\frac{1}{3}\left(\sigma^{11} + \sigma^{22} + \sigma^{33}\right), \tag{3.2}$$

where σ^{11}, σ^{22}, and σ^{33} are the components of the normal stress tensor in x, y and z directions, respectively.

3.1.1 Elastoplastic constitutive model

There are several soil constitutive models, such as the Mohr-Coulomb, Drucker-Prager and Cam-Clay models to predict the dynamic behaviors of the soil. The elastoplastic constitutive model in conjunction with the Drucker-Prager yield criterion is employed here to simulate 2D and 3D landmine detonations [37]. The plastic deformation occurs only if the following criterion is satisfied,

$$f(I_1, J_2) = \sqrt{J_2} + \varphi_\phi I_1 - k_c \geq 0\,, \tag{3.3}$$

where $I_1 = \sigma^{\alpha\alpha}, J_2 = \frac{1}{2}S^{\alpha\beta}S^{\alpha\beta}$ are the first and the second invariants of the stress tensor, respectively. φ_ϕ and k_c are Drucker-Prager model constants which are calculated from c (cohesion) and ϕ (internal friction).

$$\varphi_\phi = \frac{\tan\phi}{\sqrt{9 + 12\tan^2\phi}}\,, \tag{3.4}$$

$$k_c = \frac{3c}{\sqrt{9 + 12\tan^2\phi}}\,. \tag{3.5}$$

When solving a large deformation problem, a stress rate that is invariant with respect to rigid-body rotation should be considered and incorporated into the constitutive equation. In our current research, the Jaumann stress rate $\mathring{\boldsymbol{\sigma}}$ used for the objectivity is employed as follows.

$$\mathring{\boldsymbol{\sigma}} = \dot{\boldsymbol{\sigma}} + \boldsymbol{\sigma}\dot{\boldsymbol{\omega}} - \dot{\boldsymbol{\omega}}\boldsymbol{\sigma}\,, \tag{3.6}$$

in which $\dot{\boldsymbol{\sigma}}$ is the stress rate tensor. $\dot{\boldsymbol{\omega}}$ is the spin tensor defined as $\dot{\boldsymbol{\omega}} = \frac{1}{2}\left[(\nabla v) - (\nabla v)^T\right]$. The final stress-strain relationship of the soil model including plastic deformation can be derived as,

$$\frac{\mathrm{d}\sigma_i^{\alpha\beta}}{\mathrm{d}t} = \sigma_i^{\alpha\gamma}\dot{w}_i^{\beta\gamma} + \sigma_i^{\gamma\beta}\dot{w}_i^{\alpha\gamma} + 2G(\dot{\varepsilon}_i^{\alpha\beta} - \frac{1}{3}\delta_i^{\alpha\beta}\dot{\varepsilon}_i^{\gamma\gamma}) + K\dot{\varepsilon}_i^{\gamma\gamma}\delta_i^{\alpha\beta} - \dot{\lambda}_i[9K\sin\psi\delta^{\alpha\beta} + \frac{G}{\sqrt{J_2}}S_i^{\alpha\beta}]\,, \tag{3.7}$$

in which, $\dot{\varepsilon}_i^{\alpha\beta}$ is the strain rate tensor; K is the elastic bulk modulus and G is the shear modulus,

$$K = \frac{E}{3(1-2\nu)}\,, \tag{3.8}$$

$$G = \frac{E}{2(1+\nu)}\,, \tag{3.9}$$

in which E is the Young's modulus and ν is the Poisson's ratio. $\dot{\lambda}_i$ is the rate form of plastic multiplier, which is given in the following:

$$\dot{\lambda}_i = \frac{3\varphi_\phi K \dot{\varepsilon}_i^{\gamma\gamma} + (G/\sqrt{J_2}) S_i^{\alpha\beta} \dot{\varepsilon}_i^{\alpha\beta}}{27\varphi_\phi K \sin\psi + G} \,. \tag{3.10}$$

The derivation details of the $\dot{\lambda}_i$ is given in Appendix D. The strain rate and rotation rate tensors are defined as

$$\dot{\varepsilon}^{\alpha\beta} = \frac{1}{2}\left(\frac{\partial v^\alpha}{\partial x^\beta} + \frac{\partial v^\beta}{\partial x^\alpha}\right) , \tag{3.11}$$

and

$$\dot{w}^{\alpha\beta} = \frac{1}{2}\left(\frac{\partial v^\alpha}{\partial x^\beta} - \frac{\partial v^\beta}{\partial x^\alpha}\right) . \tag{3.12}$$

The particles approximations for the strain rate tensor and the spin tensor are presented as follows:

$$\dot{\varepsilon}_i^{\alpha\beta} = \frac{1}{2}\sum_{j=1}^{N} \frac{m_j}{\rho_j}(v_{ji}^\alpha \frac{\partial W_{ij}}{\partial x_i^\beta} + v_{ji}^\beta \frac{\partial W_{ij}}{\partial x_i^\alpha}) \,, \tag{3.13}$$

$$\dot{w}_i^{\alpha\beta} = \frac{1}{2}\sum_{j=1}^{N} \frac{m_j}{\rho_j}(v_{ji}^\alpha \frac{\partial W_{ij}}{\partial x_i^\beta} - v_{ji}^\beta \frac{\partial W_{ij}}{\partial x_i^\alpha}) \,. \tag{3.14}$$

As the elastoplastic constitutive model is implemented in this study, the soil mechanical behavior must be consistent with this model, i.e., the stress state should not be out of the yield surface when the plastic deformation occurs. However, the stress state of the soil may leave the elastic domain due to the numerical errors in computational plasticity. Therefore, the return mapping algorithm is used to return the stress state to the yield surface. According to Chen and Mizuno [81], if the stress state exceeds the apex of the yielding surface (Fig. 3.1 (a)), the hydrostatic stress components should be modified based on the following equation:

$$\overline{\sigma}^{\alpha\beta} = \begin{cases} \sigma^{\alpha\beta} - \frac{1}{3}(I_1 - \frac{k_c}{\varphi_\phi})\delta^{\alpha\beta} & \text{if } -\varphi_\phi I_1 + k_c < 0 \,; \\ \sigma^{\alpha\beta} & \text{if } -\varphi_\phi I_1 + k_c \geq 0 \,. \end{cases} \tag{3.15}$$

When the stress state of the soil exceeds the yielding surface (Drucker-Prager criterion) (see Fig. 3.1 (b)), the deviatoric shear stress components are reduced proportionally by the scaling factor R , whereas the hydrostatic component I_1 remains unchanged, according to following equations:

$$\overline{\overline{\sigma}}^{\alpha\beta} = \begin{cases} R\overline{\sigma}^{\alpha\beta} + \frac{1}{3} I_1 \delta^{\alpha\beta} & \text{if } -\varphi_\phi I_1 + k_c < \sqrt{J_2} \,; \\ \overline{\sigma}^{\alpha\beta} & \text{if } -\varphi_\phi I_1 + k_c \geq \sqrt{J_2} \,. \end{cases} \tag{3.16}$$

in which $R = \frac{-\varphi_\phi I_1 + k_c}{\sqrt{J_2}}$ is a scaling factor. For more information about the derivation of the soil elastoplastic model, please refer to Bui et al. [37].

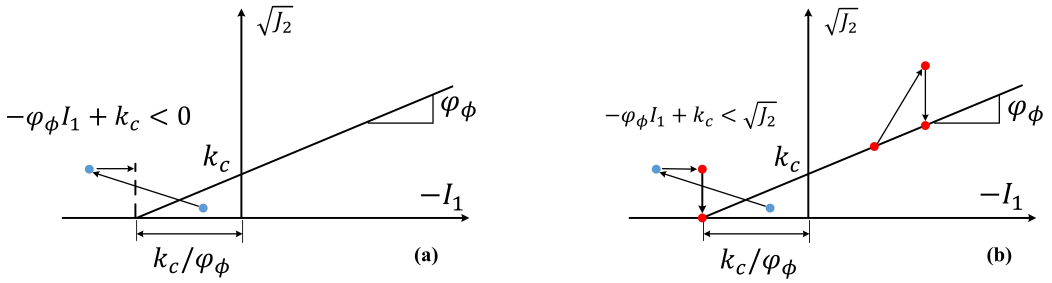

Figure 3.1 Return mapping algorithms: (a) Tension cracking treatment; (b) Stress scaling back procedure.

3.1.2 Hypoplastic constitutive model

In addition to the elastoplastic constitutive model, the hypoplastic model is presented as an alternative method to describe the dynamics behavior of soil. Different from the elastoplastic constitutive model, the hypoplastic model is established without the concepts of yield surface and flow rule. A general hypoplastic constitutive model was proposed by Wu and Kolymbas [82], which can be decomposed into two parts representing reversible and irreversible behaviors of soil, respectively. A rate independent hypoplastic constitutive model is considered here [82].

$$\mathring{\boldsymbol{\sigma}} = \boldsymbol{H}(\boldsymbol{\sigma}, \dot{\boldsymbol{\varepsilon}}) = \boldsymbol{L}(\boldsymbol{\sigma}) : \dot{\boldsymbol{\varepsilon}} - \boldsymbol{N}(\boldsymbol{\sigma})\|\dot{\boldsymbol{\varepsilon}}\| \,, \tag{3.17}$$

in which, $\boldsymbol{L}(\boldsymbol{\sigma})$ is assumed to be linear in $\dot{\boldsymbol{\varepsilon}}$ and $\boldsymbol{N}(\boldsymbol{\sigma})$ is nonlinear in $\dot{\boldsymbol{\varepsilon}}$. $\|\dot{\boldsymbol{\varepsilon}}\| = \sqrt{\mathrm{tr}\varepsilon^2}$ is an Euclidean norm. The terms $\boldsymbol{L}(\boldsymbol{\sigma})$ and $\boldsymbol{N}(\boldsymbol{\sigma})$ are usually constructed by using the representation theorem for isotropical tensorial functions.

The following specific hypoplastic constitutive model [83] is incorporated into the SPH code, which is based on a simple hypoplastic constitutive model presented by Wu and Bauer [84].

$$\mathring{\boldsymbol{\sigma}} = c_1(\mathrm{tr}\boldsymbol{\sigma})\varepsilon + \mathrm{c}_2(\mathrm{tr}\varepsilon)\boldsymbol{\sigma} + \mathrm{c}_3\frac{\mathrm{tr}(\boldsymbol{\sigma}\varepsilon)}{\mathrm{tr}\boldsymbol{\sigma}}\boldsymbol{\sigma} + \mathrm{c}_4(\boldsymbol{\sigma} + \boldsymbol{\sigma}^*)\|\varepsilon\| \,, \tag{3.18}$$

where c_1, c_2, c_3, and c_4 are dimensionless parameters; tr() stands for the trace of a tensor; $\boldsymbol{\sigma}^*$ represents the deviatoric stress tensor and is defined as,

$$\boldsymbol{\sigma}^* = \boldsymbol{\sigma} - \frac{1}{3}\mathrm{tr}(\boldsymbol{\sigma})\boldsymbol{I} \,, \tag{3.19}$$

where $\boldsymbol{I}$ is the identity tensor.

Thus, for a given particle i, the final stress-strain relationship of the hypoplastic model can be modified as,

$$\frac{d\boldsymbol{\sigma}_i}{dt} = \dot{\boldsymbol{\omega}}_i\boldsymbol{\sigma}_i - \boldsymbol{\sigma}_i\dot{\boldsymbol{\omega}}_i + c_1(\mathrm{tr}\boldsymbol{\sigma}_\mathrm{i})\varepsilon_\mathrm{i} + \mathrm{c}_2(\mathrm{tr}\varepsilon_\mathrm{i})\boldsymbol{\sigma}_\mathrm{i} + \mathrm{c}_3\frac{\mathrm{tr}(\boldsymbol{\sigma}_\mathrm{i}\varepsilon_\mathrm{i})}{\mathrm{tr}\boldsymbol{\sigma}_\mathrm{i}}\boldsymbol{\sigma}_\mathrm{i} + \mathrm{c}_4(\boldsymbol{\sigma}_\mathrm{i} + \boldsymbol{\sigma}_\mathrm{i}^*)\|\varepsilon\| \,. \tag{3.20}$$

It can be observed that the stress rate tensor in Eq. (3.20) can be calculated directly from the stress tensor and strain rate tensor. The return mapping algorithm considered in the elastoplastic constitutive equation is not required in the hypoplastic model, which greatly simplifies the numerical implementation in SPH.

3.1.3 Phase-change constitutive model

The phase-change constitutive model proposed by Dunatunga and Kamrin [9] is implemented within the SPH framework for the first time. This constitutive model allows the granular media to change through several common phases (viz., the grains can behave like a solid, liquid or gas). The granular matter is considered to be elasto-viscoplastic when the media is sufficiently dense and is treated as a disconnected material when the density of the material is smaller than a critical value. In order to calculate an objective rate of change for the stress tensor $\mathring{\boldsymbol{\sigma}}$, the Jaumann frame of reference (Eq. (3.6)) is used. The components of the trial stress tensor $\sigma_{\mathrm{tr}}^{\alpha\beta}$ can be calculated as

$$\sigma_{\mathrm{tr}}^{\alpha\beta} = \Delta t \left(\sigma^{\alpha\gamma}\dot{\omega}^{\beta\gamma} + \sigma^{\gamma\beta}\dot{\omega}^{\alpha\gamma} + 2G\left(\dot{\varepsilon}^{\alpha\beta} - \frac{1}{3}\delta^{\alpha\beta}\dot{\varepsilon}^{\gamma\gamma}\right) + K\dot{\varepsilon}^{\gamma\gamma}\delta^{\alpha\beta}\right) + \sigma^{\alpha\beta}\,, \tag{3.21}$$

where $\dot{\boldsymbol{\varepsilon}}$ is the strain rate tensor.

Using the trial stress tensor determined above, the procedure for updating the stress consists of the following steps.

1. If the particle density ρ^{n+1} is less than the critical value ρ_c, then set the stress tensor of the particle to $\boldsymbol{\sigma}^{n+1} = 0$ for the next time step.

2. For all other cases, if the trial pressure p_{tr} is negative, then $\boldsymbol{\sigma}^{n+1} = 0$ and $p_{\mathrm{tr}} = -\frac{1}{3}\mathrm{tr}(\boldsymbol{\sigma}_{\mathrm{tr}})$.

3. Otherwise, the stress tensor is computed as follows. If $\overline{\tau}_{\mathrm{tr}} \leq S_0$ where $\overline{\tau}_{\mathrm{tr}} = \left(\frac{1}{2}(\boldsymbol{S}_{\mathrm{tr}} : \boldsymbol{S}_{\mathrm{tr}})\right)^{1/2}$ and $S_0 = \mu_s p_{tr}$, the granular material is in the elastic regime, so set $\boldsymbol{\sigma}^{n+1} = \boldsymbol{\sigma}_{\mathrm{tr}}$. If $\overline{\tau}_{\mathrm{tr}} > S_0$, the granular material is in the plastic flow regime, and $\overline{\tau}^{n+1}$ is determined from

$$\left(\overline{\tau}^{n+1}\right)^2 - B\overline{\tau}^{n+1} + H = 0\,. \tag{3.22}$$

This quadratic equation for $\overline{\tau}^{n+1}$ can be solved explicitly to give

$$\overline{\tau}^{n+1} = \frac{2H}{B + \left(B^2 - 4H\right)^{1/2}}\,, \tag{3.23}$$

where B and H are obtained from $B = S_2 + \overline{\tau}_{\mathrm{tr}} + \alpha$ and $H = S_2\overline{\tau}_{\mathrm{tr}} + S_0\alpha$. Furthermore, S_2 and α are determined from $S_2 = \mu_2 p_{\mathrm{tr}}$ and $\alpha = \xi G \Delta t p_{\mathrm{tr}}$, where ξ is a parameter of the

granular media, μ_s is the friction coefficient at zero shear rate, and μ_2 is the maximum value of the friction coefficient. The stress tensor at the next time step is given by

$$\boldsymbol{\sigma}^{n+1} = \frac{\overline{\tau}^{n+1}}{\overline{\tau}_{\text{tr}}} \boldsymbol{S}_{\text{tr}} - p_{\text{tr}} \boldsymbol{I} \ . \tag{3.24}$$

3.2 Elastic perfectly plastic constitutive model for solids

The elastic perfectly plastic constitutive relation is used for the solid impact between two particles and is formulated as follows. The Jaumann rate of stress $\dot{S}_J^{\alpha\beta}$ is widely used for this purpose [31] and is related to the stress tensor as follows:

$$\dot{S}^{\alpha\beta} = \dot{S}_J^{\alpha\beta} + S^{\alpha\gamma}\dot{w}^{\beta\gamma} + S^{\gamma\beta}\dot{w}^{\alpha\gamma} \ . \tag{3.25}$$

For a material in the elastic range,

$$\dot{S}_J^{\alpha\beta} = 2G\left(\dot{\varepsilon}^{\alpha\beta} - \frac{1}{3}\delta^{\alpha\beta}\dot{\varepsilon}^{\gamma\gamma}\right) , \tag{3.26}$$

where G is the shear modulus. With the Jaumann rate of stress, the evolution of the trial elastic stress can be obtained from equations (3.25) and (3.26) as

$$S_e^{\alpha\beta} = \Delta t\left(2G\left(\dot{\varepsilon}^{\alpha\beta} - \frac{1}{3}\delta^{\alpha\beta}\dot{\varepsilon}^{\gamma\gamma}\right) + S^{\alpha\gamma}\dot{w}^{\beta\gamma} + S^{\gamma\beta}\dot{w}^{\alpha\gamma}\right) + S_{(n)}^{\alpha\beta} , \tag{3.27}$$

where $S_{(n)}^{\alpha\beta}$ is the deviatoric stress component at the n-th time step. The second invariant J_2 of the deviatoric part of the elastic trial stress $S_e^{\alpha\beta}$ is

$$J_2 = \frac{1}{2}S_e^{\alpha\beta}S_e^{\alpha\beta} \ . \tag{3.28}$$

The plastic regime is determined by Von-Mises criterion when the second invariant J_2 is greater than one-third of the square of the yield stress σ_Y. In this case, the components of the deviatoric stress tensor are brought back to the yield surface in accordance to

$$S^{\alpha\beta} = \begin{cases} S_e^{\alpha\beta} , & \text{if } J_2 \le \sigma_Y^2/3 \ ; \\ \sqrt{\frac{\sigma_Y^2}{3J_2}}S_e^{\alpha\beta} , & \text{if } J_2 > \sigma_Y^2/3 \ . \end{cases} \tag{3.29}$$

The Johnson-Cook model that accounts for thermal softening, high strain rates, and strain hardening is used to calculate the plastic yield stress σ_Y [85]:

$$\sigma_Y = \left[A + B(\varepsilon_p)^n\right]\left[1 + C\ln\left(\frac{\dot{\varepsilon_p}}{\dot{\varepsilon}_0}\right)\right]\left[1 - (T^*)^k\right] , \tag{3.30}$$

where ε_p is the equivalent plastic strain, $\dot{\varepsilon_p}$ is the equivalent plastic strain rate, and $\dot{\varepsilon_0} = 1$ s^{-1}. Furthermore, T^* is the dimensionless temperature which is defined as

$$T^* = \frac{T - T_{\text{room}}}{T_{\text{melt}} - T_{\text{room}}}, \tag{3.31}$$

where T_{room} is the room temperature, T_{melt} is the melting temperature, T is the temperature, and A, B, C, k and n are coefficients that define the the material properties.

The incremental plastic work is determined from

$$\Delta W_p^{(n)} = \frac{1}{2}\left(\sigma_p^{(n+1)} + \sigma_p^{(n)}\right)\Delta\varepsilon_p^{(n)}\left(\frac{m}{\rho^{(n+1/2)}}\right), \tag{3.32}$$

where σ_p at the $(n+1)$-th time step is calculated from the deviatoric stress tensor $\mathbf{S}_e^{(n+1)}$ as follows:

$$\sigma_p^{(n+1)} = \left(\frac{3}{2}\mathbf{S}_e^{(n+1)} : \mathbf{S}_e^{(n+1)}\right)^{1/2}. \tag{3.33}$$

Finally, the incremental equivalent plastic strain is determined from

$$\Delta\varepsilon_p^{(n)} = \frac{\sigma_p^{(n)} - \sigma_Y}{3G}. \tag{3.34}$$

The derivation details of the incremental equivalent plastic strain is in Appendix C.

3.3 The EOSs of solid and compressible flow

3.3.1 Mie-Grüneisen model

We use the Mie-Grüneisen equation [30] for the EOS of the solids used in the simulations of landmine detonation and underwater explosion conducted in the thesis. This EOS assumes the following form:

$$p = \left(1 - \frac{1}{2}\Gamma\eta\right)P_H(\rho) + \Gamma\rho E, \tag{3.35}$$

where

$$P_H(\rho) = \begin{cases} a_0\eta + b_0\eta^2 + c_0\eta^3, & \eta > 0; \\ a_0\eta, & \eta \le 0. \end{cases} \tag{3.36}$$

Here, $\eta = \rho/\rho_0 - 1$ is used to represent the compression; Γ is the Grüneisen parameter; E is the specific internal energy; and, the constants a_0, b_0, and c_0 are obtained from

$$\begin{cases} a_0 = \rho_0 C^2, \\ b_0 = a_0\left[1 + 2\left(S - 1\right)\right], \\ c_0 = a_0\left[2\left(S - 1\right) + 3\left(S - 1\right)^2\right], \end{cases} \tag{3.37}$$

where C and S are constant parameters.

3.3.2 Tillotson model

The Tillotson model is introudced to describe the hypervelocity impact behavior of metal [86] in the simulation of the jet formation of 3D shaped charge. The Tillotson EOS is divided into four regions according to the compression $\mu = \eta - 1$ and the specific energy E, where $\eta = \frac{\rho}{\rho_0}$.
1) If $\mu \geq 0$, the pressure is calculated by

$$p_1 = (a + \frac{b}{w_0})\eta\rho_0 E + A\mu + B\mu^2 \,, \tag{3.38}$$

2) If $\mu < 0$, $E \leq E_s$, the pressure is calculated by substituting $B = 0$ to Eq. (3.38).

$$p_2 = (a + \frac{b}{w_0})\eta\rho_0 E + A\mu \,, \tag{3.39}$$

3) If $\mu < 0$, $E_s < E \leq E'_s$, the pressure is calculated by the following equation.

$$p_3 = p_2 + (p_4 - p_2)\frac{E - E_s}{E'_s - E_s} \,, \tag{3.40}$$

4) If $E > E'_s$, the pressure is calculated by

$$p_4 = a\eta\rho_0 E + (\frac{b\eta\rho_0 E}{w_0} + A\mu e^{\beta x})e^{-\alpha x} \,. \tag{3.41}$$

where $w_0 = 1 + \frac{E}{E_0\eta^2}$, E_s, E'_s, E_0, A, B, a, b, α, β are the property cofficients of materials. The pressure is assumed to be 0 Pa when then material is in the tensile state.

3.3.3 JWL model

The Jones-Wilkins-Lee (JWL) equation is used here to calculate the pressure resulting from an ideal explosive detonation [87]. The JWL equation is given by

$$p = A\left(1 - \frac{w\eta_1}{R_1}\right)e^{-\frac{R_1}{\eta_1}} + B\left(1 - \frac{w\eta_1}{R_2}\right)e^{-\frac{R_2}{\eta_1}} + w\eta_1\rho_0 E \,, \tag{3.42}$$

where A, B, R_1, R_2, w are constant parameters; η_1 is the ratio of the detonation products density to the initial density of the explosive; ρ_0 is the initial density; and, E is the specific internal energy.

3.3.4 The model for the gas bubble

A gas bubble in an underwater explosion is assumed to be homogeneous, isentropic and compressible, and the EOS for a gas bubble [4] is determined from

$$p_g = p_0\left(\frac{\rho_g}{\rho_{g0}}\right)^{\gamma} \,, \tag{3.43}$$

where p_0 is the initial pressure for the bubble gas; ρ_{g0} and ρ_g are the initial density and the density of the gas, respectively; and, the constant γ is taken to have a value of 2 for our underwater explosion simulations. The speed of sound in the gas bubble is determined from

$$a_g = \left(\frac{dp}{d\rho}\right)^{\frac{1}{2}} = \left(\frac{p_0\gamma}{\rho_{g0}}\left(\frac{\rho_g}{\rho_{g0}}\right)^{\gamma-1}\right)^{\frac{1}{2}} . \tag{3.44}$$

3.3.5 The models for the compressible water

Water is modelled as a compressible fluid and is represented using two different EOSs. One of these EOSs is an alternative form of the Mie-Grüneisen equation [88] given by

$$p = \begin{cases} \frac{\rho_0 C_0^2 \mu[1+(1-\frac{\gamma}{2})\mu-\frac{\alpha\mu^2}{2}]}{[1-(S_1-1)\mu-\frac{S_2\mu^2}{\mu+1}-\frac{S_3\mu^3}{(\mu+1)^2}]^2} + (\gamma+\alpha\mu)E\,, & \mu > 0\,; \\ \rho_0 C_0^2\mu + (\gamma+\alpha\mu)E\,, & \mu \le 0\,, \end{cases} \tag{3.45}$$

where $\mu = \rho/\rho_0 - 1$, ρ_0 is the initial density, E is the specific internal energy, and S_1, S_2, S_3, γ, α and C_0 are the coefficients of the material. Another EOS for water is Tait's equation where the relation between the density and the pressure is expressed as

$$p_w = B\left(\frac{\rho_w}{\rho_{w0}}\right)^N - B + A\,, \tag{3.46}$$

where B and A are constants with values of 3.31×10^8 and 1.0×10^5 Pa, respectively; ρ_{w0} and ρ_w are the initial density and the density of water, respectively; and, N is a constant with a value of 7.15. The parameter A is set equal to the initial water pressure. The speed of sound in water is given by

$$a_w = \left(\frac{dp}{d\rho}\right)^{\frac{1}{2}} = \left(\frac{BN}{\rho_{w0}}\left(\frac{\rho_w}{\rho_{w0}}\right)^{N-1}\right)^{\frac{1}{2}} . \tag{3.47}$$

Both the Mie-Grüneisen EOS and Tait's equation can be used in the simulation of a compressible flow. Tait's equation is the simplest form of EOS for a compressible water flow, and it works well when the pressure is below 20,000 atm [4]. The Mie–Grüneisen equation of state is suitable for a completely compressible flow, and the variation in the internal energy is properly accounted for in this equation [89].

3.3.6 The modified Schmidt cavitation model

In the case of an underwater explosion near a structure and a free surface, the cavitation is created just below the free surface or in the vicinity of the structure. The primary difficulties

in the simulation of a cavitating flow are in creation and collapse of the cavity. To date, various one-fluid methods have been developed for cavitation simulation in a compressible flow [3, 4]. The modified Schmidt cavitation model is one of the most important models in this category and has been used exclusively in underwater explosion simulations [90]. Moreover, this cavitation model is physically stable. As the cavitation flow is assumed to be homogeneous, the density and the pressure of the mixture is governed by the following relationship:

$$\frac{dp}{d\rho} = a_m^2 \,. \tag{3.48}$$

The speed of sound a_m in the mixture, consisting of vapour and liquid components, is determined from

$$a_m = \left\{ [\rho_l + \alpha \cdot (\rho_v - \rho_l)] \cdot \left[\frac{\alpha}{\rho_v \cdot a_v^2} + \frac{(1-\alpha)}{\rho_l \cdot a_l^2} \right] \right\}^{-\frac{1}{2}} \,. \tag{3.49}$$

The pressure of the mixture can be obtained by integrating Eq. (3.48) after the substitution of a_m from Eq. (3.49). Alternatively, if Tait's EOS is used for pure water, the modified Schmidt cavitation model reduces to the following form:

$$p_w = \begin{cases} B\left(\frac{\rho}{\rho_0}\right)^N - B + A \,, & p \geq p_{\text{sat}} \,; \\ p_{\text{sat}} + p_{gl} \cdot \ln\left[\frac{\rho_v \cdot a_v^2 \cdot (\rho_l + \alpha \cdot (\rho_v - \rho_l))}{\rho_l \cdot (\rho_v \cdot a_v^2 - \alpha \cdot (\rho_v \cdot a_v^2 - \rho_l \cdot a_l^2))} \right] \,, & p_\varepsilon < p < p_{\text{sat}} \,; \\ p_\varepsilon \,, & p \leq p_\varepsilon \,, \end{cases} \tag{3.50}$$

where

$$p_{gl} = \frac{\rho_v \cdot a_v^2 \cdot \rho_l \cdot a_l^2 \cdot (\rho_v - \rho_l)}{\rho_v^2 \cdot a_v^2 - \rho_l^2 \cdot a_l^2} \,; \tag{3.51}$$

a_v and a_l are the constant speed of sound in the vapour and liquid components (equal to 208 m s^{-1} and 1538 m s^{-1}), respectively; and, ρ_v and ρ_l are constant densities of the vapour and liquid components, respectively. The liquid density is assumed to have a value of $\rho_l = 10^3$ kg m^{-3} and the ratio of vapour to the liquid density is assumed to have a value of $\rho_v/\rho_l = 10^{-5}$. Finally, in Eq. (3.50), p_ε is a small positive value (about 10^{-5}) and α is the void fraction, which is defined as $\alpha \equiv (\rho - \rho_l)/(\rho_v - \rho_l)$.

3.4 Summary

In this chapter, the elastoplastic, hypoplastic, and phase-change constitutive models for the investigation of the dynamic behaviors of the soil, the elastic perfectly plastic constitutive model for the solid impact, and the EOSs of explosives detonations, solids, and compressible

flow are presented, respectively. The soil constitutive models and the JWL EOS are implemented in the in-house SPH code to simulate the 2D and 3D landmine detonations. The solid constitutive model, the compressible flow EOS, and the cavitation model are applied for the modeling and simulation of the 3D underwater explosion in cylindrical rigid and Al tubes. Furthermore, the elastoplastic and phase-change constitutive models are employed to study the 3D granular impacts. The constitutive models and EOSs used in the following test cases are summarized in Table 3.1 and Table 3.2.

Table 3.1 The list of the constitutive models and the corresponding subsections.

Constitutive model	Elastoplastic	Hypoplastic	Phase-change	Elastic perfectly plastic
Subsection	5.1.2, 5.2, 5.3, 7.2.1, 7.10, 7.2.3, 7.2.4	5.1.2, 5.3	7.2.1, 7.10, 7.2.3, 7.2.4	4.2.1, 5.2, 6.3

Table 3.2 The list of the EOSs and the corresponding subsections.

EOS	M-G (solid)	Tillotson	JWL	Gas bubble	M-G (water)	Tait	Schmidt
Subsection	6.1.4, 6.3, 5.2	4.2.1	5.1.1, 5.3, 5.2, 6.1.3, 6.3	6.2	6.3	6.2, 6.3	6.1.2, 6.2

Chapter 4

Open-MP parallel computing

As the change rates of physical variables in the SPH method are obtained through the summation of the nearest particles, searching for the neighboring particles for each given particle is essential, and the SPH method is always time-consuming when solving problems with large number of particles, especially 3D problems. In order to simulate the physical processes of the 3D soil explosion and underwater explosion problems, the Open-MP parallel programming interface is introduced, and the implementation details of Open-MP in the in-house SPH code is described in this chapter. In addition, the parallel efficiency of Open-MP is tested by the 3D shaped charge detonation.

4.1 Open-MP parallel programming interface for in-house SPH code

4.1.1 An introduction to Open-MP

Open-MP is an application programming interface (API) to express shared memory parallelism. It provides compact, yet flexible shared memory programming model for C, C++, and Fortran. The notation/directives in Open-MP can be added to a sequential program to describe how the work is to be shared among the threads, and the derectives can be categorized into three aspects: parallel control structures, communication and data environment, and synchronization [91]. The control structures provide a directive to create multiple threads that execute concurrently. The basic execution model is also called fork/join model (see Fig. 4.1), which means that the execution branches off in parallel at designated points to set up parallel program and merge at subsequent point to resume sequential program. Communication between multiple threads is governed by the attributes of individual variables. For example, the private for a variable means the memory location is inaccessible to other threads; the reduction declares that a binary operator is applied to a variable repeatedly and

the result is stored back in the variable. The synchronization means the parallel program can coordinate the execution of multiple threads.

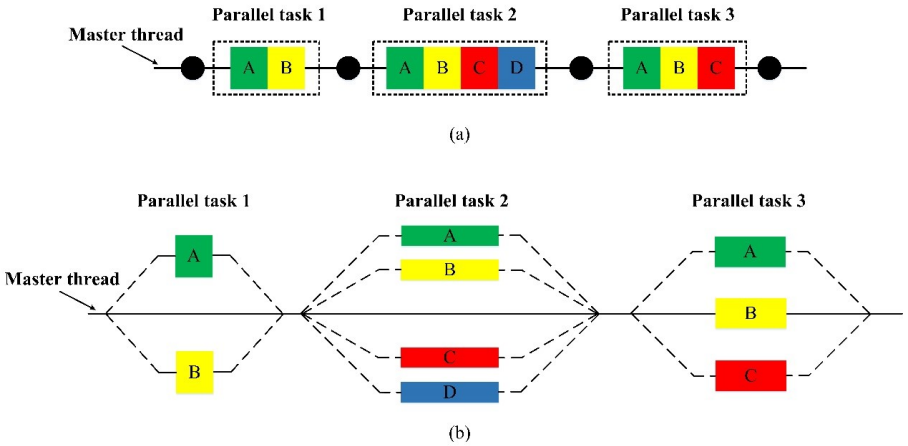

Figure 4.1 Fork/join model of Open-MP parallelism ((a) sequential program;(b) parallel program).

For the creation of Open-MP program, firstly, we require to identify the portion of sequential code that can be executed concurrently by different processors [92]. The second step for creating Open-MP program is to add appropriate directives to express parallelism that has been identified. The huge benfit of Open-MP is that the directive can be inserted into regions of program incrementally, which means that once the resulting program has been compiled and tested, another portion of code can be parallelized. It is essential that the resulting parallelized code should be correct. At the end, we can find some techniques to improve the performance of a parallel program.

4.1.2 Implementation of the Open-MP programming interface

Starting the Open-MP implementation is relatively easier than other parallelization methods. For the simple loops, the directives can be added directly. For the parallelization of more complicated loops, the attributes of the variables should be defined carefully. For example, the calculation of the velocity change rate in the artificial viscosity subroutine consists in a loop running on all of the pairwise interaction particles. In order to avoid the race condition on access to the array dvxdt(dim,maxn), another new temporary array should be constructed as dvxdt1(dim,maxn,th), in which the variable th is used to determine the thread number executing the current iteration. In addition, the initialization of these arrays is important since it ensures that the in-house SPH code runs correctly in a serial or a parallel mode.

```
!$OMP parallel num_threads(numofthreads)
!$OMP do
```

```
      do i=1,ntotal
        do d=1,dim
          dvxdt(d,i) = 0.e0
          do k=1,numofthreads
            dvxdt1(d,i,k)=0.e0
            dedt1(i,k)=0.e0
          enddo
        enddo
        dedt(i) = 0.e0
      enddo
!$OMP END do
!$OMP end parallel
```

After the initialization of these arrays, this complex loop can be parallelized. The directives for the parallel compilation are indicated as follows. It can be found that the temporary array can be calculated concurrently with no access to other arrays.

```
!$OMP parallel private(i,j,mhsml,dx,vr,rr,dvx,muv,mc,mrho,piv,h)
!$OMP+private(ithr)
!$OMP+num_threads(numofthreads)
!$OMP do
      do k=1,niac
!$      ithr=omp_get_thread_num()+1
        i = pair_i(k)
        j = pair_j(k)
        mhsml= (hsml(i)+hsml(j))/2.
        vr = 0.e0
        rr = 0.e0
        do d=1,dim
          dvx(d) = vx(d,i) - vx(d,j)
          dx     =  x(d,i) -  x(d,j)
          vr     = vr + dvx(d)*dx
          rr     = rr + dx*dx
        enddo
        if (vr.lt.0.e0) then
          muv = mhsml*vr/(rr + mhsml*mhsml*etq*etq)
          mc   = 0.5e0*(c(i) + c(j))
          mrho = 0.5e0*(rho(i) + rho(j))
          piv  = (beta*muv - alpha*mc)*muv/mrho
          do d=1,dim
```

```
            h = -piv*dwdx(d,k)
            dvxdt1(d,i,ithr) = dvxdt1(d,i,ithr) + mass(j)*h
            dvxdt1(d,j,ithr) = dvxdt1(d,j,ithr) - mass(i)*h
            dedt1(i,ithr) = dedt1(i,ithr) - mass(j)*dvx(d)*h
            dedt1(j,ithr) = dedt1(j,ithr) - mass(i)*dvx(d)*h
          enddo
        endif
      enddo
!$OMP END do
!$OMP end parallel
```

After finishing the calculation of dvxdt1(dim,maxn,th), the summation of these temporary arrays is required for the calculation of dvxdt(d,i). In the end, we can obtain a correct numerical result for dvxdt(d,i).

```
!$OMP parallel num_threads(numofthreads)
!$OMP do
      do i=1,ntotal
        do k=1,numofthreads
          do d=1,dim
            dvxdt(d,i)=dvxdt(d,i)+dvxdt1(d,i,k)
          enddo
            dedt(i)=dedt(i)+dedt1(i,k)
        enddo
         dedt(i) = 0.5e0*dedt(i)
      enddo
!$OMP END do
!$OMP end parallel
```

4.2 Numerical examples

The 3D shaped charge detonation involving large number of particles are tested here to validate the efficiency and stability of the Open-MP programming interface. Given that the main goal of this chapter is to present the details of the implementation of Open-MP and validate the performance of Open-MP, the explosion, Tillotson, and elastoplastic models are not verified here. The validation cases for each component of SPH code are given in the following chapters, and you can also refer to [58] for the validation cases.

4.2.1 3D shaped charge detonation

The general configuration of the shaped charge is shown in Fig. 4.2. In this example, the thick of the case is 5 mm, the thick of the aluminum liner is 3 mm, and the cone angle is 60°. Both of the total length and diameter of the shaped charge are 60 mm. The initial geometry of the simulation is very close to the initial experimental configuration from [93]. The JWL, Johnson-Cook, and Tillotson EOSs are employed for the simulation of the shaped charge detonation, and the parameters for these three models are listed in Table 4.1, 4.2, and 4.3, respectively. The CPU Intel E5-2683 is employed in this computation.

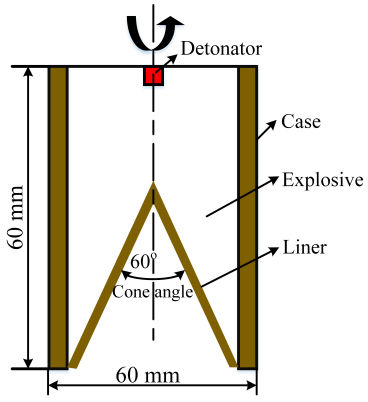

Figure 4.2 General configuration of the shaped charge.

Firstly, it is required to identify the most time-comsuming part in the sequential SPH code. The computational efforts of the different parts of the SPH program are analysed first and shown in Table 4.4 . We can find that the most time-consuming parts are the nearest particles searching and the calculation of the variables change rates. Therfore, these two parts are the most essential parts to parallelize. The rest part of the sequential SPH code, especially the do loops can be parallelized incrementally. In order to obtain a good performance of the parallelization, it is essential to parallelize a sufficiently large portion of the SPH code. This idea is expressed by the Amdahl's law, in which the overall speed is determined by

$$S = \frac{1}{(1-F) + \frac{F}{S_p}}, \tag{4.1}$$

in which, F is the parallelized fraction and the S_p is the speedup of the parallelized sections. From this equation, we can find that the performance of the parallelization will be limited by F. For example, if F is equal to 70%, the speedup S will be restricted by 3.33 (let S_p go to infinity).

Table 4.1 Coefficients of the JWL model for explosives.

Materials	ρ_0 (kg/m^3)	A (Pa)	B (Pa)	R_1	R_2	w	E_0 (J/kg)	v (m/s)
Composition B	1600	5.242×10^{11}	7.68×10^9	4.2	1.1	0.34	5.31×10^6	7980

Table 4.2 Johnson-Cook parameters for Al.

A (MPa)	B (MPa)	C	n	k	T_{room} (K)	T_{melt} (K)
175	380	0.0015	0.34	1.0	273	775

Table 4.3 Coefficients of the Tillotson model for Al.

A (GPa)	B (GPa)	a	b	α	β	$e_0(kJ \cdot g^{-1})$	$e_s(kJ \cdot g^{-1})$	$e'(kJ \cdot g^{-1})$
75.20	65.00	0.50	1.63	5.00	5.00	5.00	3.00	15.00

Table 4.4 The computational time (seconds) cost for each part of the sequential SPH code.

Particles number	Initialize	Particle search	Change rates	Others	Total
7859	0.3623	79.9060	138.8682	37.3681	256.1423
17112	0.2821	180.7744	337.3471	88.7661	606.8876
30698	0.5069	373.9897	681.3730	178.0906	1233.4533

The influence of different threads on the computational time, the speedup versus different threads, and the parallel efficiency versus different threads are tested here to evaluate the performance of the parallel SPH code. These results are presented in Fig. 4.3, Fig. 7.7, and Fig. 4.5 respectively, in which the parallel efficiency is obtained by dividing the speedup by the total number of threads. It can be found that the calculation time decreases dramatically for the number of threads from 2 to 15, and slow down before reaching a calculation plateau. Similarly, the speedup ratio increases rapidly to around 10 times until almost reaching a steady state. The parallel efficiency of the case with larger number of particles is higher than

the efficiency of case with smaller number of particles. The phenomenon can be explained by several reasons. Firstly, according to the Amdahl's law, the speedup is limited by the percentage of the program that is parallel. Secondly, the parallel loop will not finish until all the threads complete their iterations. The parallel performance will suffer if some of the processors execute more work than other processors. Thirdly, the memory band width is shared by N processors, and these threads will compete for the use of memory band width, which will lead to the performance degradation. There are several approaches to improve the performance of our current parallel SPH code. For example, we can use a better computer to run the parallel SPH code so that the multiple threads can use shared memory with less competition. We can improve the load balancing so that each thread spends an equal amount of time in parallel loop. Moreover, we can employ larger number of particles for the detonation problems to increase the parallel efficiency of the program. For the completion of the investigation of this problem, the detonation process is also given below (see Fig. 4.6). There are 240,000 particles involved in this simulation. Firstly, the detonation wave reaches the apex of the cone cavity (see Fig. 4.6 a). Then the detonation wave moves perpendicular to the cone cavity. The metal is compressed by the high pressure generated by explosive products and converges to the centerline (see Fig. 4.6 c). In the end, a metal jet of high energy and velocity is formed. The numerical jet velocity using the SPH method is around 7,000 m/s, which is very close to the experimental data [93].

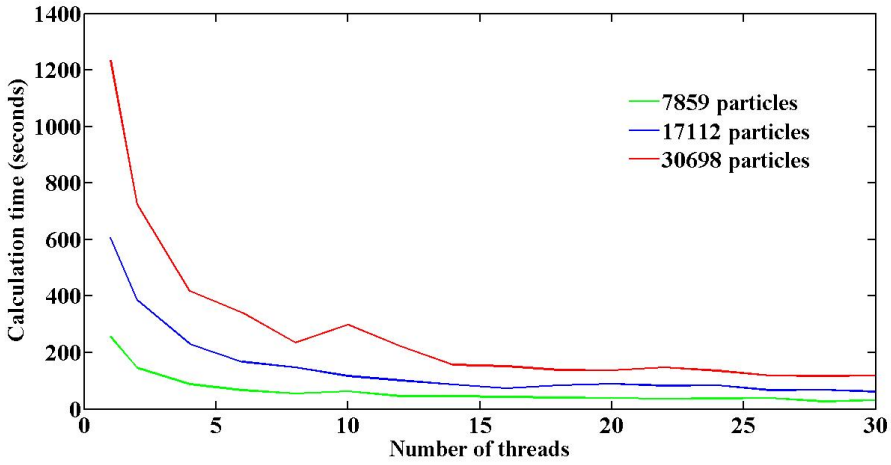

Figure 4.3 Simulation time versus the number of threads involved.

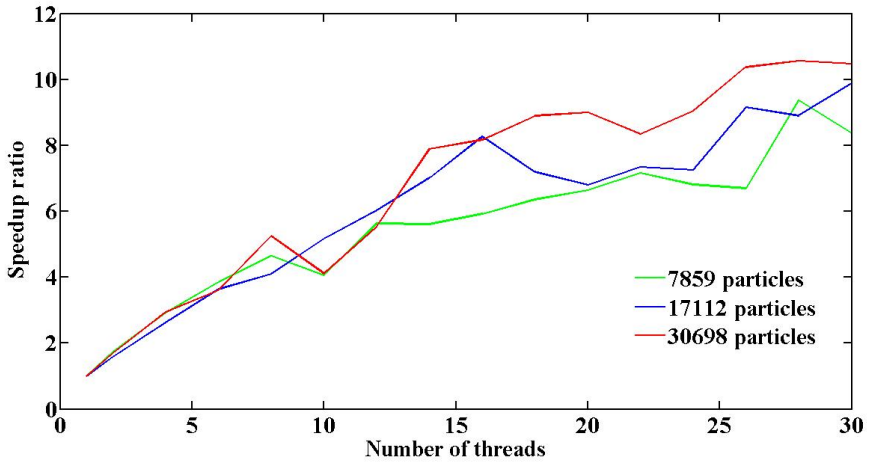

Figure 4.4 The speedup ratio of the parallel in-house SPH code using Open-MP.

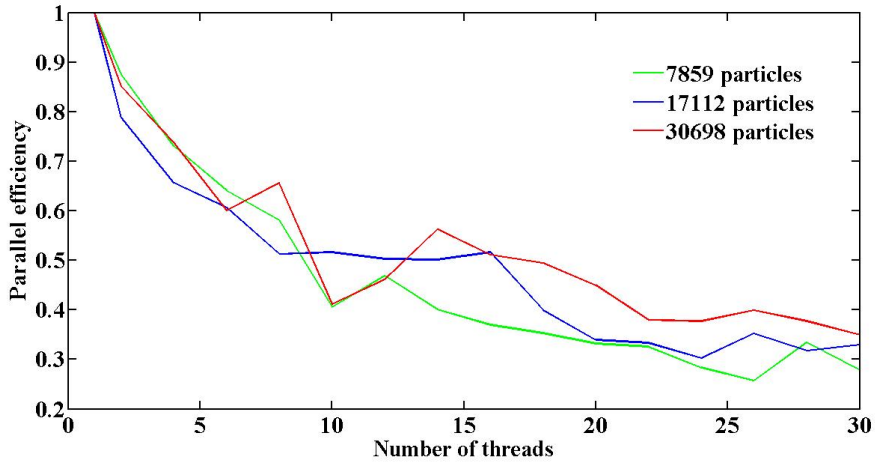

Figure 4.5 The parallel efficiency of the in-house SPH code using Open-MP.

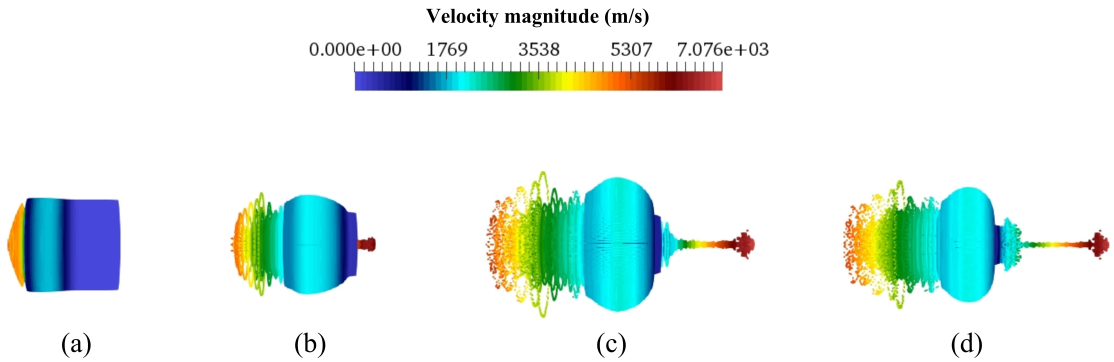

Figure 4.6 The detonation process of the shaped charge.

4.3 Summary

The Open-MP programming interface has been implemented in the in-house SPH code, and the speedup ratio and the parallel efficiency of the code have been analysed using the simulation of the 3D shaped charge detonation in this chapter. The simulation results show that the computational time decreases rapidly to with the increase of threads, and the speedup ratio tends to 10 when using 24 threads. Therefore, the Open-MP can be employed to parallelize the most time-consuming part in SPH so that the calculation efficiency can be enhanced sigficantly. Based on the parallelization of the in-house SPH code, the 3D landmine detonation and underwater explosion can be investigated in the following chapters.

Chapter 5

2D and 3D Landmine detonations

In this chapter, the 1D TNT slab detonation and 2D sand collapse have been tested to verify the JWL and soil constitutive models first. Based on the validation of these models, the 2D landmine detonation and its effect on structures are investigated. Afterwards, the 3D landmine detonation is studied with the implementation of the Open-MP parallel programming interface.

5.1 Numerical validations

5.1.1 TNT explosion

To show the accuracy and effectiveness of the SPH method for detonation problems, the benchmark problem of 1D TNT explosion is provided here. The total TNT slab is 0.1 m and is ignited at one end. The symmetrical slab is used in the present study so that the solid wall boundary can be represented by the symmetrical boundary (see Fig. 5.1). As the detonation velocity of the TNT explosive charge is 6930 m/s, it takes about 14 μs to finish the detonation process along the TNT slab. The values of the JWL model coefficients for TNT are listed in Table 5.1. E_0 is the initial specific internal energy. 2000 particles are used in this simulation. The initial particle space Δx is 0.01 cm and the time step Δt is 1.0×10^{-9} s. The initial pressures and velocities of all the particles are assumed to be 0 Pa and 0 m/s, respectively.

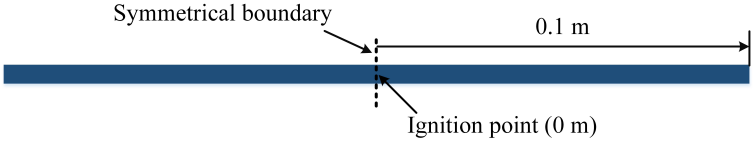

Figure 5.1 Numerical model of one-dimensional TNT slab detonation.

Table 5.1 Coefficients of the JWL model for TNT.

ρ_0 (kg/m^3)	A (Pa)	B (Pa)	R_1	R_2	w	E_0 (J/kg)
1630	317.2e9	3.21e9	4.15	0.95	0.30	4.29e6

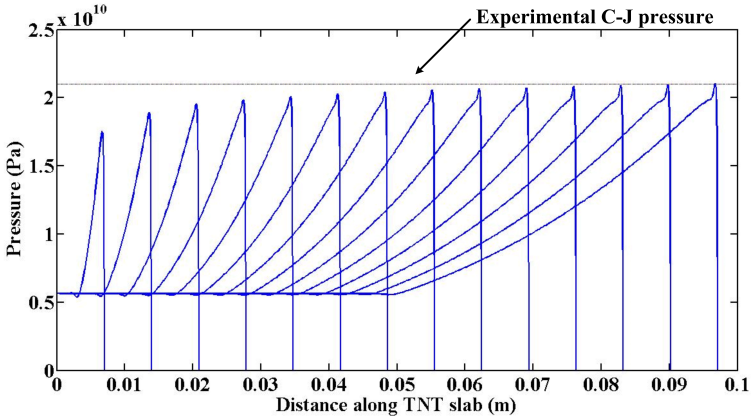

Figure 5.2 Pressure distribution along the one-dimensional TNT slab during the detonation process.

It can be seen from the Fig. 5.2 that with the detonation process in the TNT slab, the numerical results of C-J pressure converge to 21 Gpa, which is in good agreement with the experimental data. In addition, the influence of different number of particles on simulation results is studied (see Fig. 5.3). It can be found that the peak pressure increases slightly with an increase in the number of particles and converges to 21 GPa eventually.

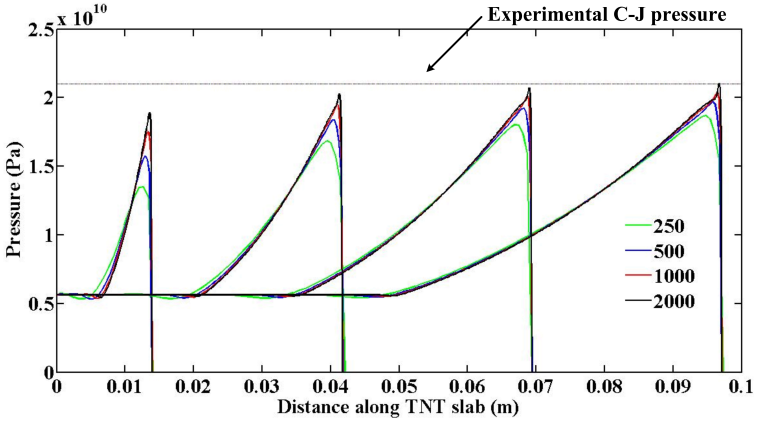

Figure 5.3 Pressure distribution along the one-dimensional TNT slab with different particles.

5.1.2 Sand collapse

The numerical implementations of the elastoplastic and hypoplastic models are validated by the sand collapse problem, respectively. A rectangle of sand confined between two vertical parallel plates remains static. Then the gates are opened (i.e. the plates are lifted up) and the sand is released. Thus the 3D problem can be simplified to a 2D plane strain problem solved by this 3D SPH code. The length d of this rectangle sand is 0.4 m, the height h of it is 0.1 m, and the ratio $a = h/d$ determines the collapse mode. The coefficients of elastoplastic and hypoplastic models are listed in Table 5.2. There are five input parameters in the constitutive models, an uncertainty analysis to quantify the influence of all uncertain input parameters on the simulation results can be conducted in the same way in research [94–96]. In this thesis, the material parameters correspond to the sand in the experiments conducted by Lube et al. [97], and are employed directly. The particle spacing is $\Delta d = 2$ mm, and 10,000 particles are involved in this simulation. In addition, the non-slip boundary condition is implemented in this simulation by using three layers of dummy particles.

Table 5.2 The elastoplastic and hypoplastic constitutive models coefficients for the sand collapse problem [8].

	Elastoplastic constants					Hypoplastic parameters			
$\rho_0(kg/m^3)$	E (MPa)	ϕ (^{o})	ψ (^{o})	c (kPa)	ν	c_1	c_2	c_3	c_4
2100	20.0	30.0	1.0	0.0	0.25	-55.6	-171.2	-540.9	-170.9

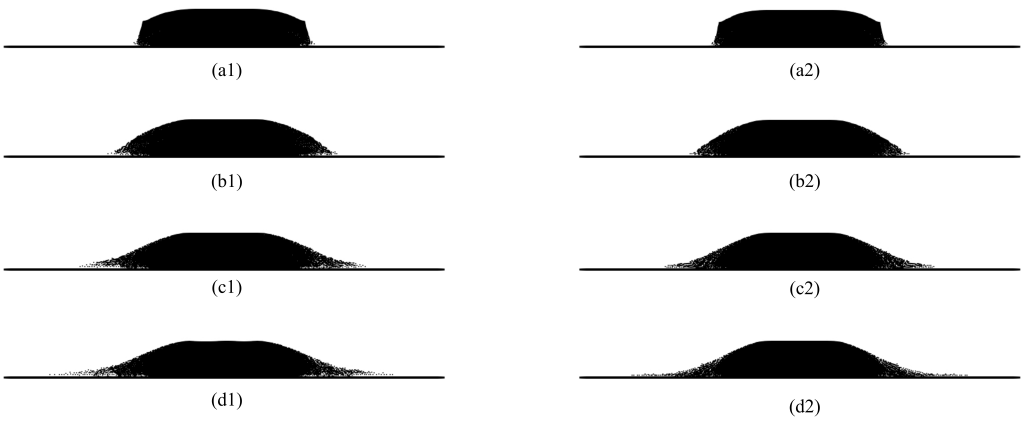

Figure 5.4 Collapse process of sand with the elastoplastic (a1-d1) and the hypoplastic (a2-d2) constitutive models.

The sand collapse processes using the elastoplastic and hypoplastic models are well described in Fig. 5.4 in terms of distribution of particles. At first, a discontinuity can be initially observed as a straight line on the upper surface of the sand column. After a while, a curve plane occurs between the static and moving particles. Finally, a parabolic-like surface profile is formed, which agrees well with the collapse process in the experiment and simulation from [8, 97].

The stresses distributions of these two models are presented in Fig. 5.5. It can be found that the horizontal and vertical stresses increase linearly with the depth, which is consistent with the stresses distributions of the sand confined in two parallel plates and subjected to gravity. The shear stress develops in two areas close to the wall. The reason is the sand at the bottom tend to move sideward but are restricted by the non-slip boundary condition. Therefore, these two constitutive models have been verified by the sand collapse problem.

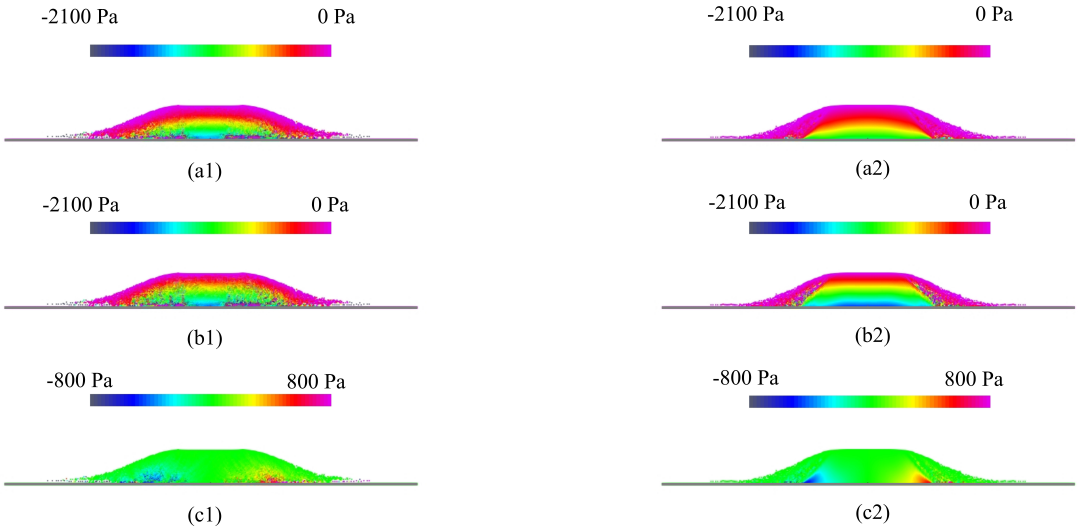

Figure 5.5 Stresses distributions of sand collpase problem at steady state with the elastoplastic constitutive model ((a1) horizontal stress σ_{xx}; (b1) vertical stress σ_{yy}; (c1) shear stress σ_{xy}) and the hypoplastic constitutive model ((a2) horizontal stress σ_{xx}; (b2) vertical stress σ_{yy}; (c2) shear stress σ_{xy}).

5.2 2D soil explosion and its effects on structures

The initial geometry for the soil explosion test case and its effects on structures are shown in Fig. 5.6, which is similar to the experimental configuration in [1]. The TNT explosive is buried to the depth of 28 mm in dry soil and the steel plate standing at 140 mm above the soil surface is 100 mm thick, 1000 mm long. The JWL, Drucker-Prager, Johnson-Cook, Mie-Grüneisen models are incorporated into this simulation and the parameters of these models

are listed in Table 5.1, Table 5.2, Table 5.3 and Table 5.4. Three layers of dummy particles are used for the solid boundary to prevent the soil particles from penetrating througn the boundary. The gravitational force is considered in this simulation and the sound speed (c = 600 m/s) in soil is applied in the computation.

5.2.1 Soil explosion simulation

Firstly, the TNT landmine detonation is investigated in this section. 9215 particles are used is this numerical model. The initial particle spacing Δx is 0.5 cm, Δy is 0.5 cm, and the time step Δt is 1×10^{-7} s. The pressure distribution of landmine detonation process is shown in Fig. 5.7. After the buried TNT charge is ignited, the extremely high pressure detonation wave propagates in the explosive and the explosive converts rapidly into dense gas (Fig. 5.7 (a)). Once the detonation wave reaches the edge of TNT, the detonation energy is mostly transmitted to the soil adjacent to the explosive, which generates the elastic and plastic deformation of surrounding soil. Thus the soil cap is ejected from the soil surface and, as a result, the soil bubble which confines the expanded gas is generated due to the expansion of explosive products (Fig. 5.7 (b), (c), (d)). The shockwave generated by TNT detonation propagates in the soil (Fig. 5.7 (b), (c), (d)). We can find from Fig. 5.8 (a) that the velocity of the particle on top of the dome is the largest as the soil at this location gains most of the momentum from the buried explosive. This is the reason why the dome becomes larger and larger. The soil bubble will expand, thin and rupture at certin point as shown in Fig. 5.7 (e), (f). The outline of soil ejecta depicted in Fig. 5.7 (f) is like the shape of a bulb as more resistance force in the soil is imposed on the expanded products than that in the air. The stresses distributions in xx, yy and xy directions at 0.16 ms are presented in Fig. 5.8 (b), (c) and (d). It can be observed that the horizontal and vertical stresses reach their maximum magnitudes at the interface between soil and explosive products. The shear stresses at this interface are antisymmetrical with respect to the vertical direction. In addition, the heights of the soil ejecta predicted by the simulation at 0.10 ms and 0.14 ms are compared with the experimental results from [1] (see Fig. 5.9) and a general agreement is observed, which is encouraging. The fitting curve of the pressure and the detonation time at point A (0 mm, 140 mm) is shown in Fig. 5.10. It can be found that the magnitude of the pressure at the point A increases significantly to 110 MPa at around 0.16 ms and then decays rapidly over a short period of time. The computational data appears reasonable and acceptable, and is similar to the published experimental results for axisymmetric case in [1], although the two dimensional plane-strain case is simulated here. The soil explosion simulation in three-dimensional space, which requires a large number of particles, will give more accurate results. We will extend the current 2D problem to 3D in the following section.

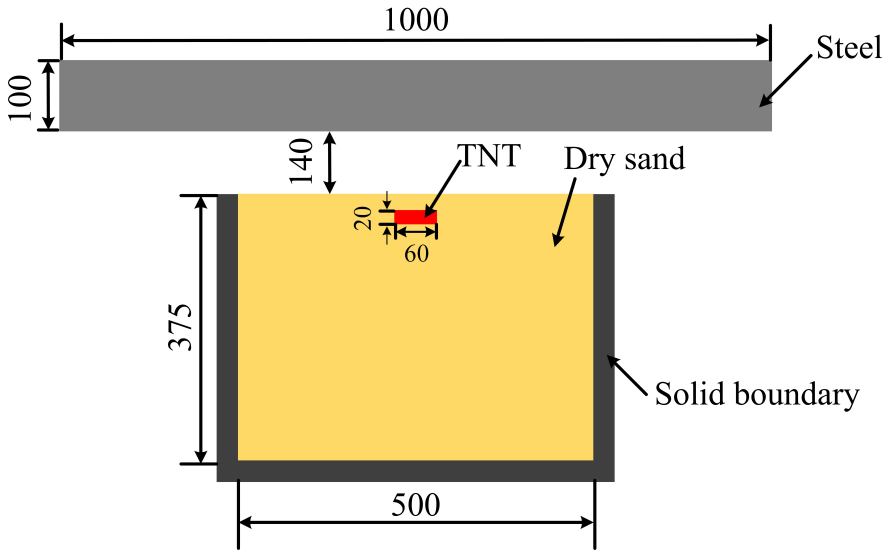

Figure 5.6 Configuration of landmine detonation and its effects on structures (unit: mm).

Table 5.3 Johnson-Cook model parameters of steel.

A (MPa)	B (MPa)	C	n	k	T_{room} (K)	T_{melt} (K)	C_v (J/kg K)
350	275	0.022	0.36	1.00	273	1810	452

Table 5.4 Mie-Grüneisen EOS model parameters of steel.

ρ_0 (kg/m^3)	C_0 (km/s)	S_1	S_2	S_3	γ	α	E_0 (J)
7830	3.63	4.569	1.49	0.0	0.0	2.17	0

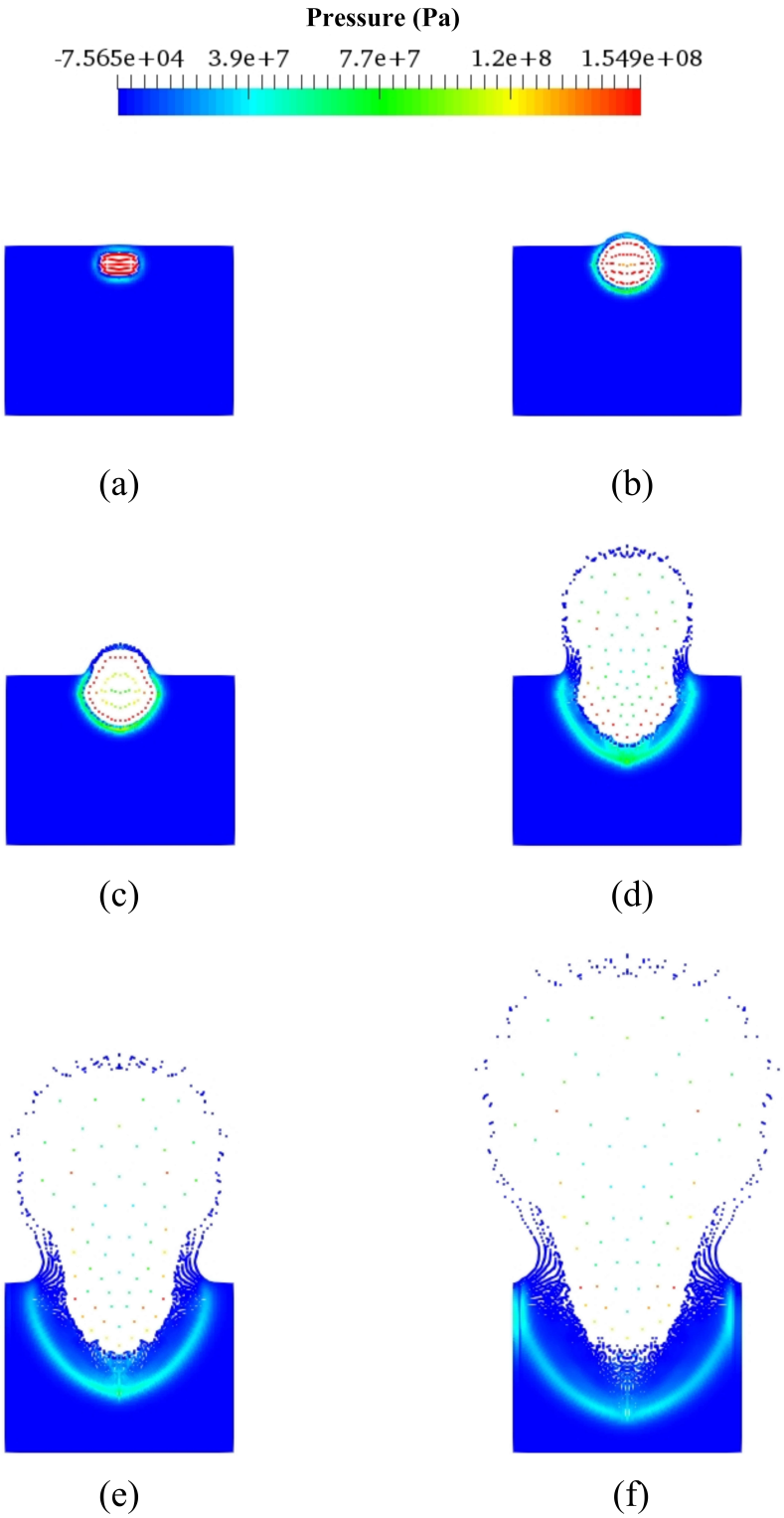

Figure 5.7 Pressure distributions of soil explosion at (a) 0.01 ms; (b) 0.05 ms; (c) 0.1 ms; (d) 0.35 ms; (e) 0.6 ms; (f) 0.85 ms.

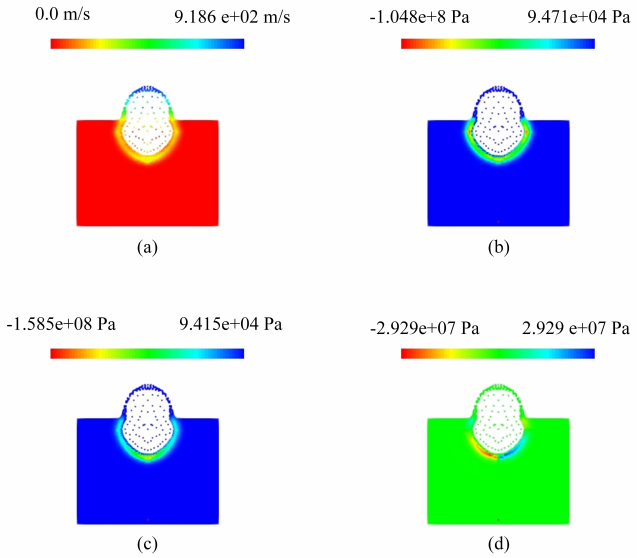

Figure 5.8 Distributions of (a) velocity and stresses in (b) xx, (c) yy, (d) xy directions at 0.16 ms.

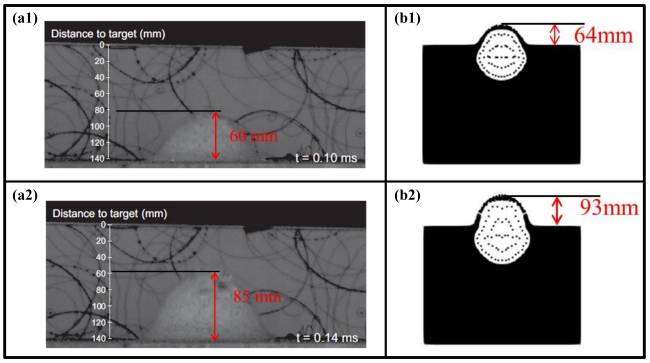

Figure 5.9 Comparisons of the height between the experiment [1] (a1, a2) and the simulation (b1, b2) at 0.1 ms and 0.14 ms.

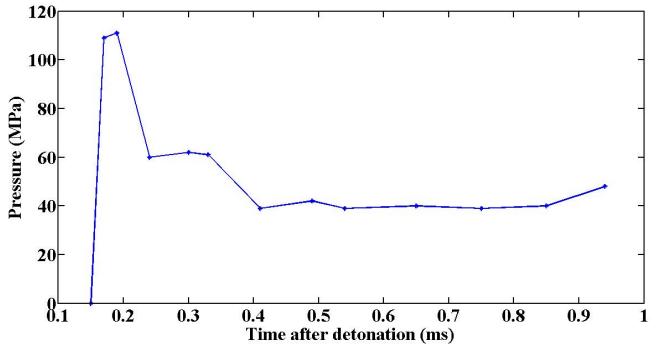

Figure 5.10 Pressure-time history at 140 mm above the sand surface.

5.2.2 Simulation of structural response to blast loading of buried explosive

Full investigation of the soil explosion structures interactions provides a robust approach to assess and safely design platforms and vehicles which maybe subjected to Improvised Explosive Devices (IDEs) attacks. Following the results of explosion in soil presented in subsection 5.2.1, the structural response to soil explosion can now be studied. 13,436 particles are used is this numerical model. The initial particle spacing and the time step are the same as in the soil explosion modeling.

The explosive-soil and soil-steel plate interactions are clearly distinguishable in Fig. 5.11. In the first stage, the apex of the soil ejecta arrives at the bottom of the steel at 1.5 ms, which is close to the arrival time of pressure wave reported in [1]. Afterwards, the soil ejecta momentum is partially transmitted to the steel, and the stress wave propagation in the steel plate is shown in Fig 5.11 (a), (b), (c). The soil-plate interaction area becomes larger and larger and the steel also crushes with recoverable elastic deformation and permanent plastic deformation during this process (Fig 5.11 (d), (e), (f)) as the detonation products continue to expand and impact the plate. The outline of the soil as a result of explosive products and structure interactions presented in this paper is similar to the simulation result using the ALE method [98]. The damage size of the structure depends on properties of the soil and structure, the available energy imparted to the target, and the geometry of the soil explosion. In addition, the time history of energy has been checked, and Fig. 5.12 shows that the global energy remains almost constant. After the TNT explosion, internal energy reduces while kinetic energy grows correspondingly over a short period of time. This is because the internal energy of explosive is partially transmitted to the kinetic energy of explosive gas and soil. When the soil ejecta impacts the steel plate at around 0.17 ms, the loss of kinetic energy of soil ejecta is then transferred to the internal energy of the steel. Thus the internal energy increases while the kinetic energy drops gradually. The soil explosion/structure interaction model can also be applied to predict the damage mode of the steel plate with different thickness and angles in three dimensions, which will be conducted in the future research.

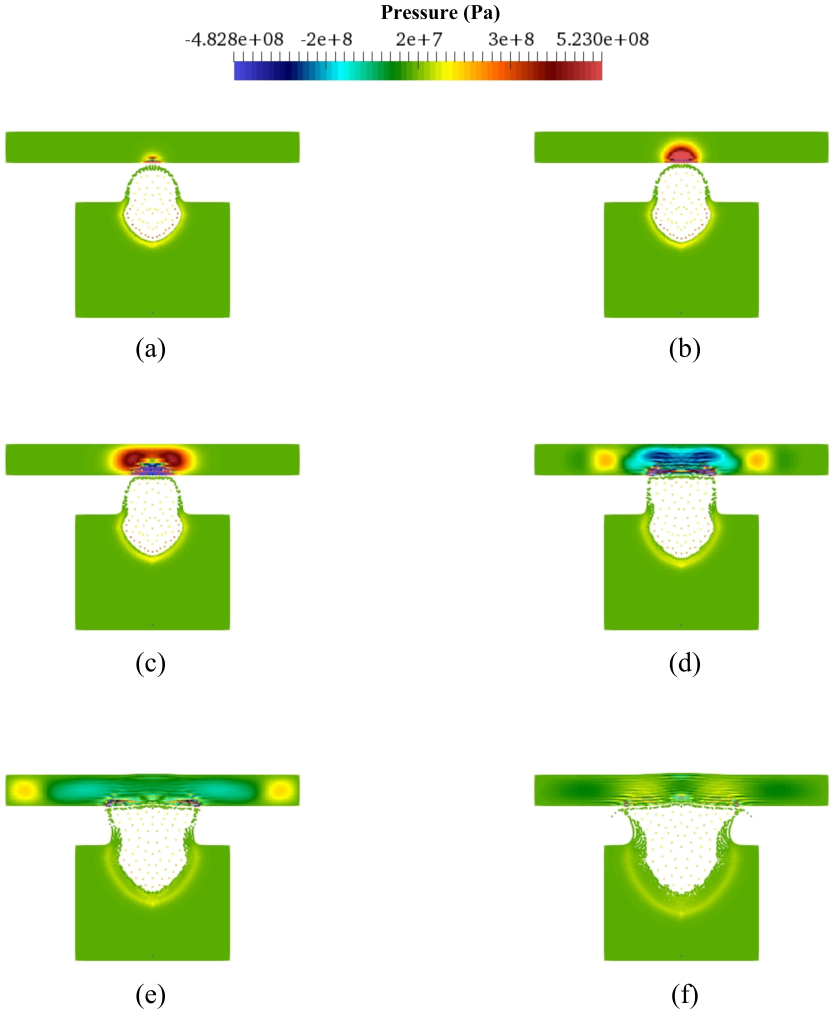

Figure 5.11 Pressure distributions of structural response to explosion in soil at (a) 0.16 ms; (b) 0.17 ms; (c) 0.19 ms; (d) 0.25 ms; (e) 0.35 ms; (f) 0.5 ms.

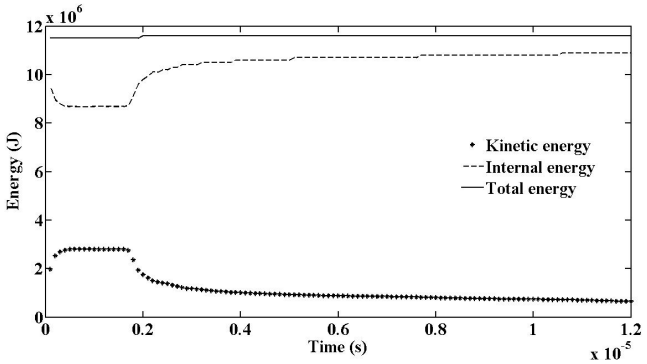

Figure 5.12 Energy-time history of soil explosion and its interaction with structure.

5.3 3D landmine detonation

In this section, the elastoplastic and hypoplastic constitutive models are combined with the explosion model to simulate the 3D landmine detonation. The motivation of this simulation is to predict the soil ejecta generated from buried C4 explosive. The initial configuration of soil explosion simulation is shown in Fig. 5.13, which is exactly the same as the experimental geometry from [1]. A cylindrical container, with 375 mm height and 500 mm internal diameter, is filled with dry sand. A cylindrical C4 explosive charge is buried to the sand with a depth of 28 mm, and its surface is parallel to the sand surface. The coefficients of the elastoplastic and hypoplastic models used in this simulation are the same as in the sand collapse problem (see Table 5.2). Three layers of dummy particles are introduced to represent fixed solid boundary condition. The particle spacing is $\Delta d = 4.17$ mm, and 1,150,000 particles are involved in this simulation. The simulation time step is chosen to be $\Delta t = 1.0 \times 10^{-7}$ s. Furthermore, the Open-MP programming interface is incorporated to the in-house SPH code for the parallelization and acceleration of the computation. The CPU used here is Intel E5-2683. The total computational time for the landmine detonation is 72 CPU hours.

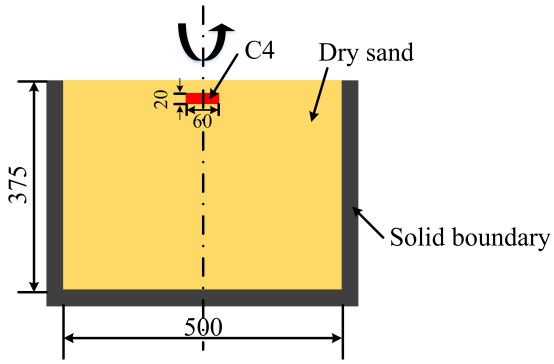

Figure 5.13 Initial geometry of the landmine detonation (mm).

Firstly, the elastoplastic model is used and its velocity distributions of the soil fragmentation process are shown in Fig. 5.14. After the ignition of the C4 explosive, a detonation wave travels outward from the detonation point. Once the shockwave reaches the edge of the explosive, most of the energy is transmitted to the surrounding soil. (see Fig. 5.14 (a), (b)). The particles at the top of the soil are pushed up by the detonation and gains the most momentum from the buried explosive, and a spherical dome is formed. It can be observed that the velocities of the particles at the top of the dome are always larger than the rest particles of the soil ejecta. The top soil moves much faster and this spherical dome becomes larger and larger. The profile of the soil fragmentation is like a bubble shown in Fig. 5.14 (d), which is close to the experimental data [1]. As the explosion gas continue to expand, the soil bubble will become thinner and rupture at some point.

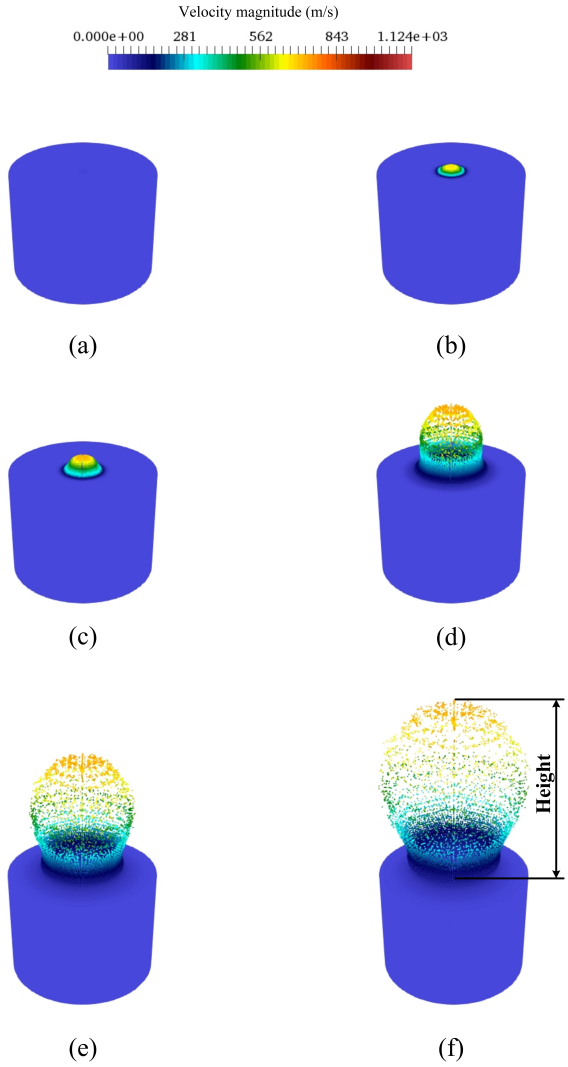

Figure 5.14 Velocity distributions of landmine detonation at (a) 0.01 ms; (b) 0.05 ms; (c) 0.10 ms; (d) 0.35 ms; (e) 0.60 ms; (f) 0.84 ms.

The particles density distributions are presented in Fig. 5.15. It shows that the densities of the soil particles below the explosive are the largest, as more resistance and compression are encountered by these particles compared to the rest of the particles surrounding the explosive charge. The detonation shock wave propagates through the interaction zone and expands the soil particles to every direction. Furthermore, the heights of load-deflection curves (see Fig. 5.14 (f)) for different discretizations (particle spacing of $3\Delta x$, $2\Delta x$, $1.5\Delta x$, and $\Delta x = 4.17$ mm) are investigated and shown in Fig. 5.16. It can be found that the heights grow with an increase in the number of particles, which converges to the values along the red line. This shows the reliablity and stability of the numerical results. Therefore, the main process of the soil fragmentation using the elastoplastic model has been captured and

well described by the SPH method.

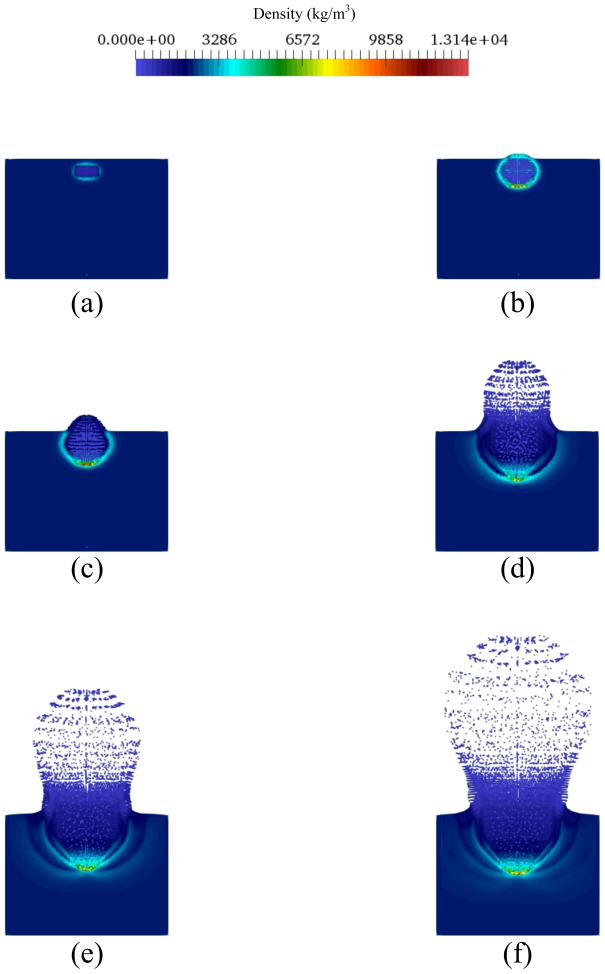

Figure 5.15 Density distributions of the landmine detonation at (a) 0.01 ms; (b) 0.05 ms; (c) 0.10 ms; (d) 0.35 ms; (e) 0.60 ms; (f) 0.84 ms.

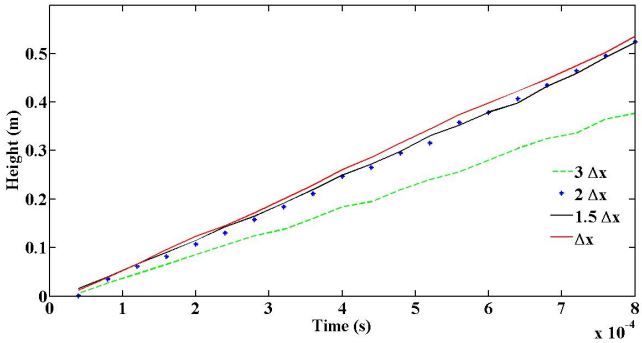

Figure 5.16 Height-time history of 3D landmine detonation using different discretizations.

In addition to the elastoplastic constitutive model, the hypoplastic model has also been implemented to study the detonation process. The total number of particles involved in this simulation is the same as the previous one. The velocities distributions of the landmine detonation using the hypoplastic model are presented in Fig. 5.17. It can be found that the soil fragmentation using this model is very similar to the soil ejecta using the elastoplastic model, and this mutual authentication strengthens the credibility of these simulation results. However, the widths obtained from the elastoplastic model are larger than those obtained from the hypoplastic model (see Fig. 5.18 (b4)). In order to check the validity of the 3D soil explosion model, the outline of the soil fragmentation obtained from these two constitutive models are compared with the experimental data at respective times t = 0.03 ms, 0.10 ms, 0.14 ms, and 0.18 ms (see Fig. 5.18). We can find that the profiles of soil ejecta at different times are very close to the experimental data. Even the extremely small soil deformation at 0.03 ms can still be captured by the SPH method (see Fig. 5.18 (a1, b1, c1)). Moreover, the heights and widths of the soil fragmentation are mearsured to verify the 3D landmine detonation modeling further (see Fig. 5.18 (b4)). Table 5.5 presents the heights and widths calculated from these two constitutive models, and these physical variables are very similar to the experimental measurements. The relative errors are calculated by relative error = $|\text{sim}-\text{exp}|/\text{exp}$, in which sim represents simulation results and exp denotes the experimental results. The relative error1 and error2 are calculated from the elastoplastic and hypoplastic models, respectively. It can be observed that most of the relative errors are less than 12 %, which shows that the SPH method method in conjunction with these two soil constitutive models can tackle landmine detonation problems successfully. In addition, the time history of energy balance of 3D landmine detonation using the hypoplastic constitutive model is shown in Fig. 5.19. It can be observed that the total energy of the landmine detonation is conserved. After the detonation of C4 explosive, the internal energy of the explosive is transferred to the kinetic energy of the sand. Thus the internal energy decreases while the kinetic energy increases rapidly. Then the sand near the expanded explosive gas interacts with the sand further, and some of the kinetic energy of the sand is converted into the internal energy of the surrounding sand. At the end, the kinetic and internal energies reach a steady state. In comparison with the results obtained from the 2D soil explosion simulations [58], the 3D soil explosion modeling yields more accurate widths and heights of the soil ejecta.

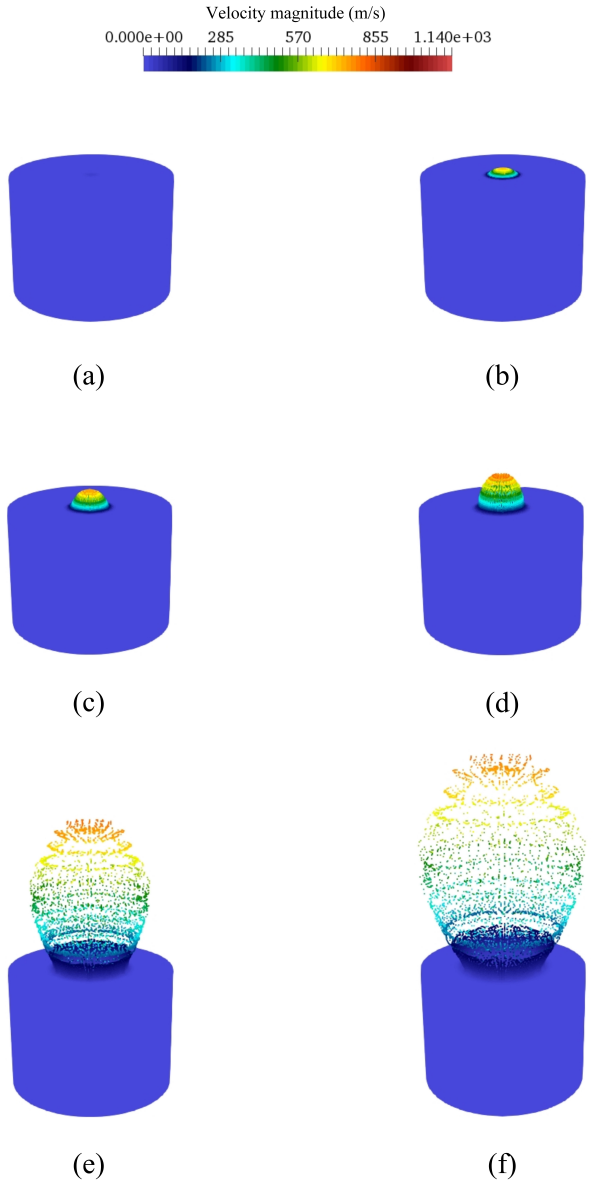

Figure 5.17 Velocity distributions using the hypoplastic model at (a) 0.01 ms; (b) 0.05 ms; (c) 0.10 ms; (d) 0.35 ms; (e) 0.60 ms; (f) 0.84 ms.

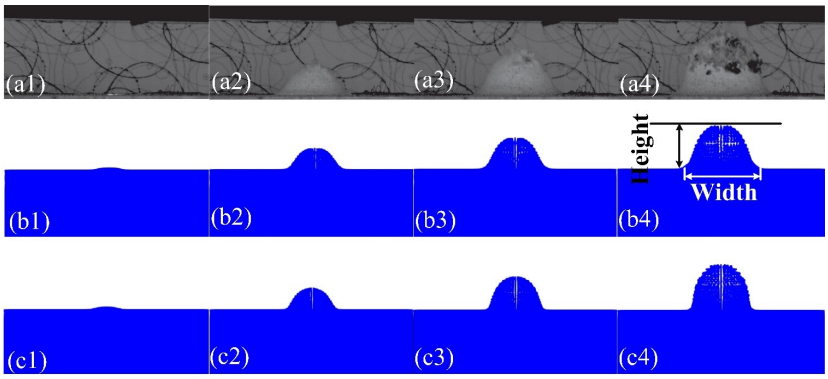

Figure 5.18 Comparison of the soil ejecta between the experimental [1] and simulation results, in which (a1-a4), (b1-b4) and (c1-c4) are results of the experiment, elastoplastic model, and hypoplastic model, respectively.

Table 5.5 Comparison of the heights and widths obtained from the experiments and simulations (mm).

	t = 0.03 ms		t = 0.10 ms		t = 0.14 ms		t = 0.18 ms	
	Height	Width	Height	Width	Height	Width	Height	Width
Experiment	5.0	33.3	55.0	120.0	82.0	136.5	115.0	180.0
Elastoplastic	5.2	37.5	52.8	130.0	76.0	160.2	98.0	200.0
Hypoplastic	5.1	37.0	52.3	109.4	75.4	132.0	97.2	160.7
Relative error1 (%)	4.0	12.6	4.0	8.3	7.3	17.2	14.7	11.1
Relative error2 (%)	2.0	11.1	4.9	8.8	8.0	3.3	15.4	11.8

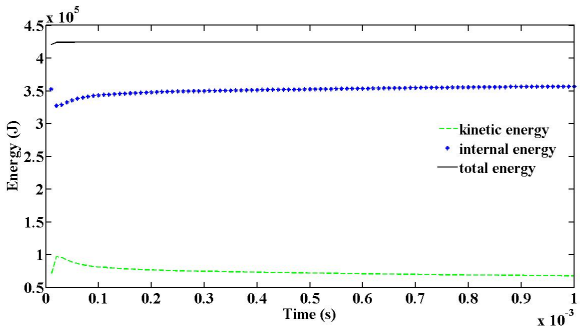

Figure 5.19 Time history of energy balance of 3D landmine detonation using the hypoplastic constitutive model.

5.4 Summary

In this chapter, the JWL detonation model and soil constitutive models are validated first. After the validation of these models, the 2D soil explosion and its effects on structures has been investigated. The modified continuity equation described in Chapter 2 is employed to tackle the multiphase interface with large density ratio. Based on the study of 2D soil exploison, the 3D landmine detonation with the elastoplastic and hypoplastic constitutive models has been conducted further. The widths and heights of the soil fragmentation are in general agreement with the experimental data, which shows that the SPH method is capable of tackling the landmine detonation problems well.

Chapter 6

Underwater explosion within a tube including cavitation

The underwater explosion within a tube including cavitation is investigated in this chapter. In order to verify the physical models used in underwater explosion, the Sjögreen problem, 1D cavitating flow in an open tube, 1D PETN detonation, and the 3D impact of Al ball on the Al plate are tested using the in-house 3D SPH code first. Then the explosions in a water filled cylindrical rigid and Al tubes are investigated, respectively, and the simulation results are compared against the published analytical results and the experimental data.

6.1 Numerical validations

6.1.1 Sjögreen test

The gas-gas shock tube problem is tested here to show that the shock wave simulation can be well predicted by the 3D SPH code. The Eq. (3.43) is used as EOS here. The left and right initial conditions are listed in the following,

$$\Big(\rho(kg/m^3), v(m/s), p(Pa)\Big) = \begin{cases} (1.0, -2.0, 0.4) & 0.0 < x < 0.5 \\ (1.0, 2.0, 0.4) & 0.5 < x < 1.0 \end{cases} \tag{6.1}$$

The pressure and velocity distributions along the tube at 0.150 s are shown in Fig. 6.1 and Fig. 6.2, respectively. We can find that the simulation results using the SPH method are in good agreement with the analytical results [99].

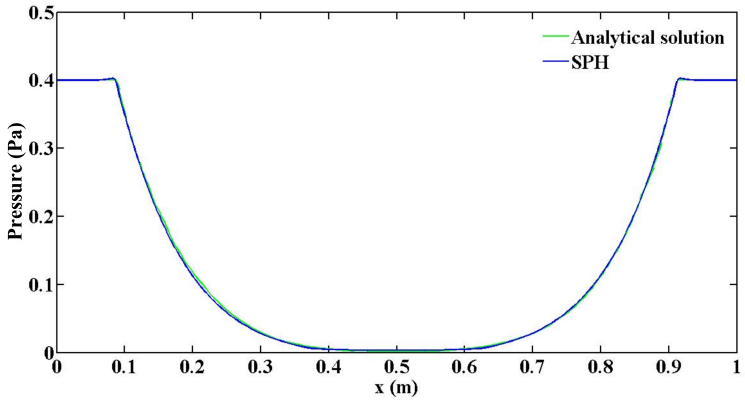

Figure 6.1 The pressure distribution along shock tube at 0.15 s.

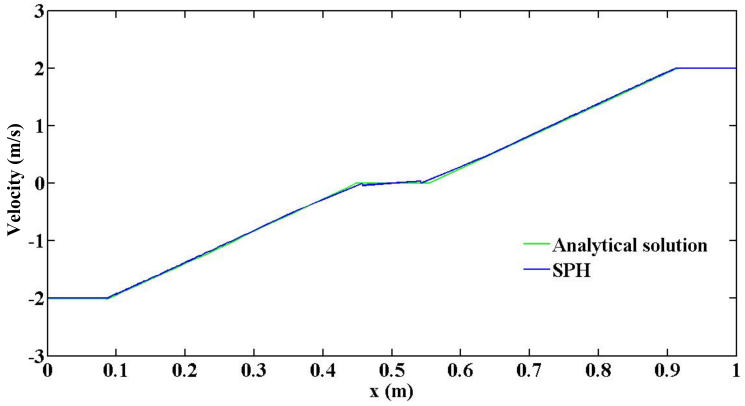

Figure 6.2 The velocity distribution along shock tube at 0.15 s.

6.1.2 1D cavitating flow in an open tube

The second case proposed by Liu et al. [4] is tested in the 3D SPH code to verify the cavitation model. The Eq. (3.46) is employed as EOS in this case. The initial condition of this water-water Riemann problem is presented as follows,

$$\left(\rho(kg/m^3), v(m/s), p(Pa)\right) = \begin{cases} (1000, -100, 100,000) & 0.0 < x < 0.5 \\ (1000, 100, 100,000) & 0.5 < x < 1.0 \end{cases} \tag{6.2}$$

The numerical results of the pressure and velocity along two water streams with different particle resolutions ($\Delta x = 0.5, 4/3\Delta x, 2\Delta x$ mm) at 0.2 ms are depicted in Fig. 6.3 and Fig. 6.4, respectively, and it can be observed that the pressure and velocity distributions using the SPH method are in general agreement with numerical results using conventional mesh-based method with the one fluid cavitation model [4].

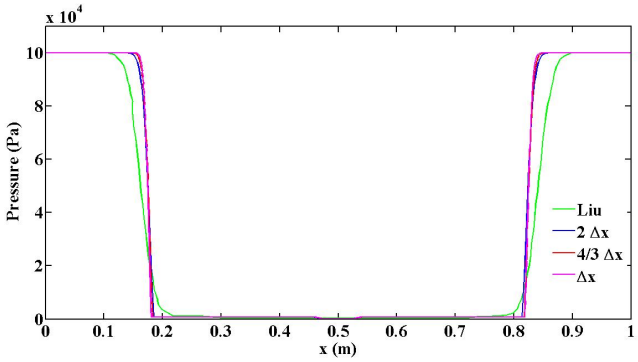

Figure 6.3 The pressure distribution along two water streams at 0.2 ms with different particle resolutions.

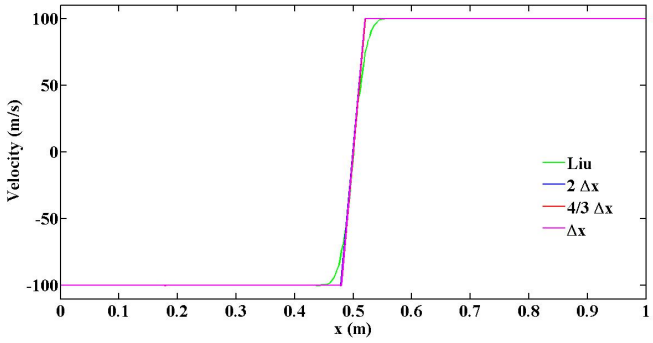

Figure 6.4 The velocity distribution along two water streams at 0.2 ms with different particle resolutions.

6.1.3 1D PETN detonation

The simulation of the 1D PETN explosive detonation is conducted here to verify the JWL model. The EOS employed here is Eq. (3.42). The detonation process is the same as the TNT detonation described in Subsection 5.1.1. As the detonation velocity of the PETN explosive charge is 8350 m/s, it takes about 11 μs to finish the detonation process along the PETN slab. The JWL parameters for 1D PETN detonation are shown in Table 6.1 [100]. The total length of the PETN slab is 0.1 m. The initial particle spacing is 0.0002 m, and the time step is 1.0×10^{-9} s. The pressure distributions along the PETN slab with different number of particles (250, 500, 1000, 2000) at respective times is shown in Fig. 6.5. It can be observed that the numerical peak pressure converges to the experimental peak pressure 33.5 GPa.

Table 6.1 Coefficients of the JWL model for PETN.

ρ_0 (kg/m^3)	A (Pa)	B (Pa)	R_1	R_2	w	E_0 (J/kg)
1765	6.17×10^{11}	1.6926×10^{10}	4.4	1.2	0.25	5.722×10^{6}

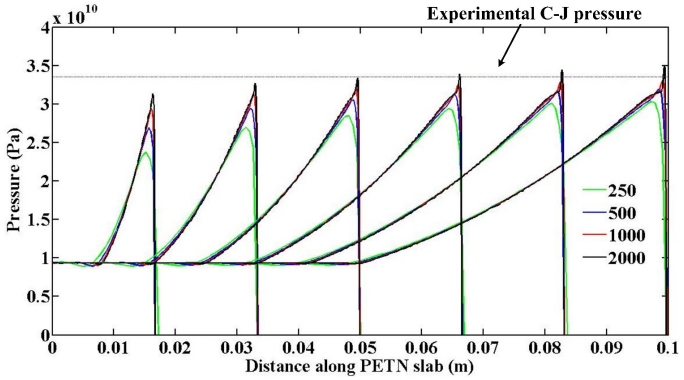

Figure 6.5 Pressure distribution along the 1D PETN slab during the detonation process.

6.1.4 3D high velocity impact

The impact of 3D aluminum (Al) sphere on a thin Al plate is simulated here to verify the elastic-perfectly plastic constitutive model. The Mie-Grüneisen equation and Johnson-Cook parameters for Al-Al impact are shown in Table 6.2 and Table 6.3 [30], respectively. The radius of the Al sphere is 0.01 m, and the velocity of the sphere is 6180 m/s. The length, width, and height of the Al plate are 0.1 m, 0.004 m, 0.1 m, respectively. 690,243 particles are involved in this simulation. The numerical result of the high velocity impact at 16 μs is shown in Fig. 6.7. From a qualitative point of view, it can be found that the whole shape of debris cloud of the simulation is similar to the experimental data (Fig. 6.6) [2]. In addition, the impact model has also been validated quantitatively by the Armco iron cylinder impact in our previous research paper [59].

Table 6.2 Coefficients of the Mie-Grüneisen model for Al-Al high velocity impact.

ρ_0 (kg/m^3)	C (m/s)	S	G (MPa)	Y_0 (MPa)	Γ
2710	5300	1.5	2.76×10^{4}	550	1.70

Table 6.3 Johnson-Cook parameters for Al-Al high velocity impact.

A (MPa)	B (MPa)	C	n	k	T_{room} (K)	T_{melt} (K)	C_v (J/kg K)
175	380	0.0015	0.34	1.0	273	775	875

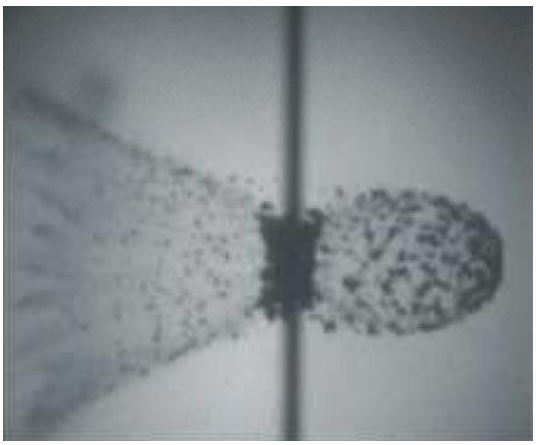

Figure 6.6 Experimental debris cloud produced by the impact of Al sphere on a thin Al plate [2].

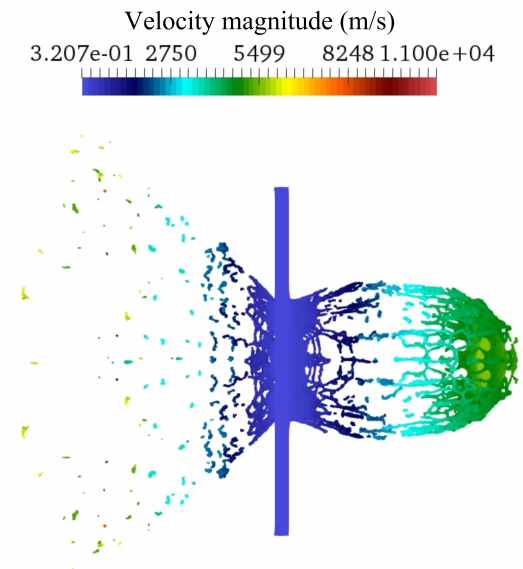

Figure 6.7 Numerical debris cloud produced by the impact of Al sphere on a thin Al plate.

6.2 Underwater explosion within a rigid cylindrical structure

Now the 3D underwater explosion in a rigid cylinder can be investigated based on these verified models above. The initial geometry of this problem is shown in Fig. 6.8, which is the same as the initial configuration in [3]. The diameter and the height of the cylinder are 0.0889 m and 0.2886 m, respectively. In order to compare with the simulation results from [3] directly, the explosion model is simplified to a high pressure gas bubble. The spherical explosive gas is located in the center of the cylinder, and its diameter is 0.03 m. The Eq. (3.43) is used as EOS for explosive gas, and the initial pressure and density of the explosive gas sphere are set equal to $p_g = 2 \times 10^9$ Pa and $\rho_g = 1770\ kg/m^3$, respectively. The parameter γ in Eq. (3.43) is set to be 2.0 in this problem. The Tait's equation (Eq. (3.46)) is employed in this simulation, and the initial pressure and density of the surrounding water are assumed to be $p_w = 1 \times 10^5$ Pa and $\rho_w = 1000\ kg/m^3$, respectively. The modified Schmidt cavitation model is employed for the pressure lower than the saturated vapour pressure which is equal to 3165 Pa here. The initial particle spacing is $\Delta x = 0.001$ m, 1,800,000 particles are involved in this simulation, and three layers of dummy particles are implemented for the solid boundary treatment. The time step for this simulation is $\Delta t = 1.0 \times 10^{-8}$ s. The CPU used here is Intel E5-2683, and the total computational time is 120 CPU hours for the calculation of 12,000 time steps.

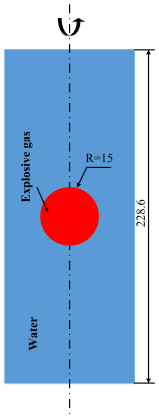

Figure 6.8 Initial geometry of underwater explosion within a rigid cylinder (mm).

Fig. 6.9 a1-a8 shows the pressure distributions at respective times of 15 μs, 30 μs, 45 μs, 60 μs, 75 μs, 90 μs, 105 μs, and 120 μs. Once the explosion is initiated, a compressive shock wave is created and propagates symmetrically to the solid boundary (Fig. 6.9 a1). Then the reflected shock wave from the solid wall interacts with the expanded high pressure gas, and a rarefaction wave is generated (Fig. 6.9 a2). A cavitation area (white area) maybe formed near the bubble surface as the rarefaction wave can be so strong. The rarefaction

wave hits the cylinder wall and is reflected from the boundary, and a cavitation is generated near the solid boundary (Fig. 6.9 a3-a5). At the end, the cavitation area collapses due to the compression of the compressive shock wave (Fig. 6.9 a6-a8). In addition, the pressure contour using the SPH method are compared against the simulation results using the Arbitrary Lagrangian-Eulerian (ALE) method [3] (see Fig. 6.9 b1-b8). It can be found that the shock wave propagation and the location of the cavitation predicted by the SPH method are fairly close to those obtained with the ALE method. Fig. 6.10 shows the pressure history, with initial particle spacing Δx = 0.001 m and 1.5 Δx, at the centre location of the side wall using the SPH method compared against the numerical results using the conventional mesh-based method from Liu [4]. For the initial particle spacing Δx, it can be observed that the pressure of the SPH method at the mid-line wall increases rapidly to 0.660 GPa at 19 μs. Then the pressure reduces near the wall and the cavitation is created at 42 μs. This cavitation region finally collapses completely within 98 μs. It can be found that the first increase and decrease of the pressure and the cavitation creation are close to the Liu's results. The second pressure raise and second cavitation occur at 102 μs and 117 μs, respectively, which are a little earlier than the Liu's results, and the second peak pressure 0.35 GPa is less than the peak pressure of the Liu's simulation 0.43 GPa. The difference between the simulation results of SPH and ALE is reasonable, firstly, the 3D underwater explosion within a rigid cylinder has been conducted directly, which is different from the 2D cylindrical coordinate system used in [3, 4]. Secondly, it can be observed that a better numerical pressure distribution (Fig. 6.10) can be obtained with larger number of particles. However, involving more particles in the simulation is beyond the capability of the current available computational resources. Thirdly, the artificial viscosity is adopted in SPH to supress the shock wave oscillation, while in Liu's paper [4], they used the integral-differential form to treat the relationship across the cavitation boundary. Furthermore, the SPH is a Lagrangian particle method, the calculation of the physical variables is based on the summation of the nearest particle in a support domain, which is totally different from the mesh-based numerical method. Lastly, the boundary implementation method (dummy particles) in SPH is totally different from the boundary treatment in the conventional mesh-bashed methods. In general, the comparison of numerical results between the SPH method and the ALE method shows that the shock wave propagation and cavitation occurring in the underwater explosion can be captured by SPH, and thus the SPH method can solve the underwater explosion within a rigid cylinder very well.

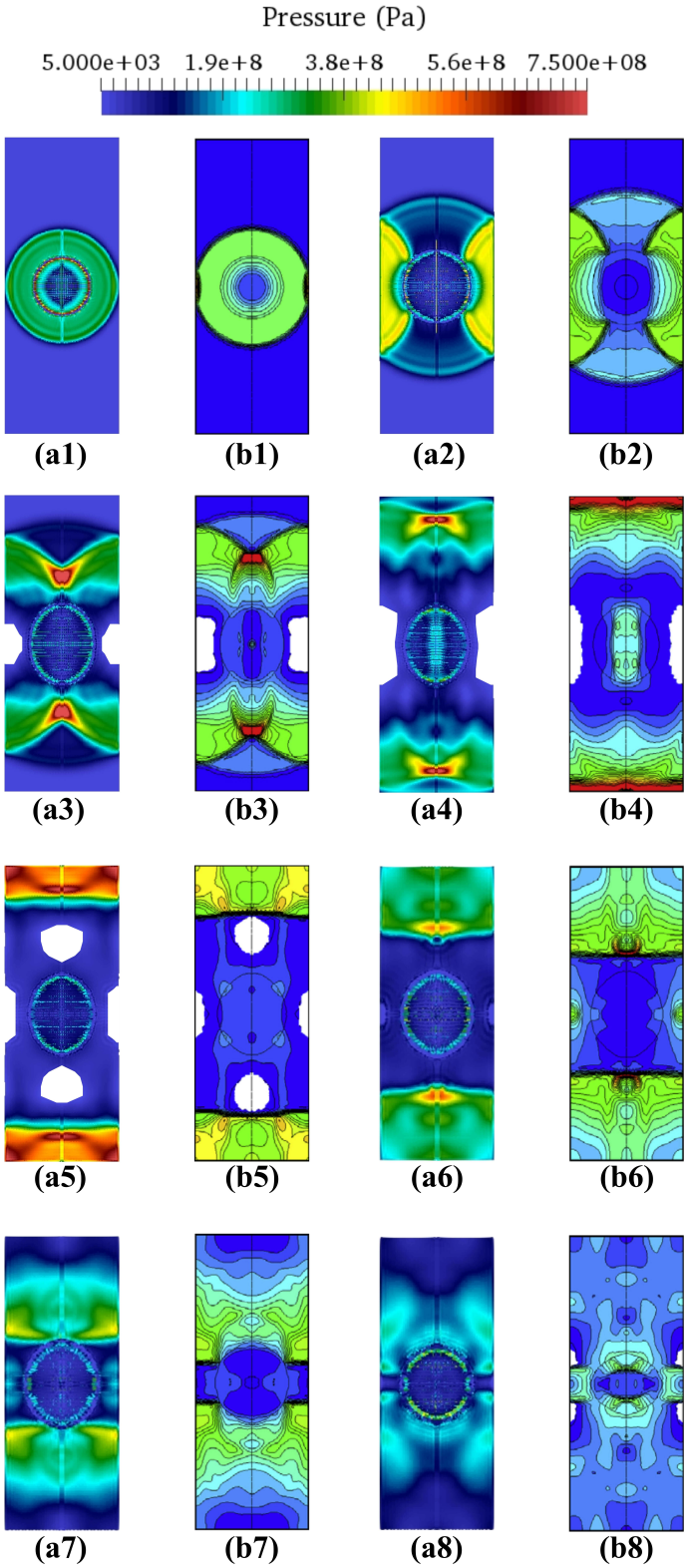

Figure 6.9 The pressure distribution of the underwater explosion within a rigid cylinder from 15-120 μs using the SPH (a1-a8) and the ALE method (b1-b8) [3].

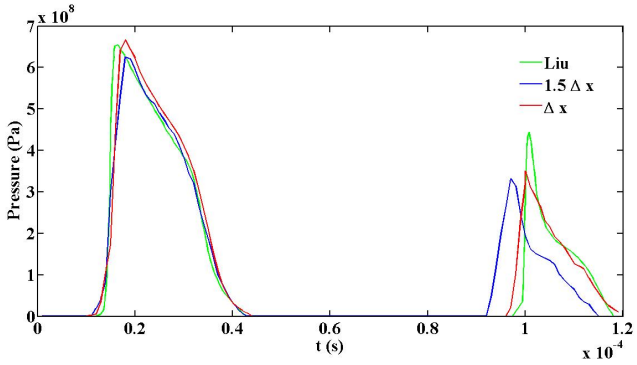

Figure 6.10 The pressure histories at mid-line wall of rigid cylinder from Liu's simulation [4] and the present SPH solution.

6.3 3D underwater explosion within an aluminum tube

Furthermore, the simulation of the 3D underwater explosion within an aluminum tube is developed. The initial configuration of the simulation is exactly the same as the initial experimental geometry from [100] (see Fig. 6.11).

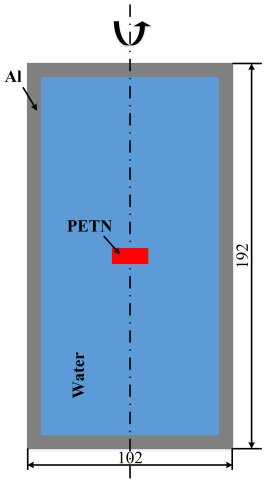

Figure 6.11 Initial geometry of underwater explosion within an aluminum tube (mm).

The deformable structure is 19.2 cm long and 10.2 cm outer diameter Al tube with 0.7 cm wall thickness. The small explosive charge of 3.0 g PETN is suspended inside the Al tube filled with distilled water. The JWL parameters for PETN detonation is listed in Table 6.1, and the Mie-Grüneisen and Johnson-Cook model parameters for Al is presented in Table 6.2 and Table 6.3, respectively. Both the Mie-Grüneisen and Tait's equation are employed for the compressible fluid simulation. The Mie-Grüneisen parameters for water is shown in Table 6.4 [60]. The initial particle spacing is set to be 0.001 m, the time

step is 1×10^{-8} s, and 870,000 particles are involved in this simulation. The Open-MP programming interface is implemented for the acceleration of the calculation procedure. The CPU applied here is Intel E5-2683, and the total computational time is 78 CPU hours for the calculation of 12,000 time steps.

The pressure and the velocity distributions of this underwater explosion using Tait's equation at respective times of 15 μs, 30 μs, 45 μs, 60 μs, 75 μs, 90 μs, 105 μs, and 120 μs are shown in Fig. 6.12 and Fig. 6.13, respectively. According to our numerical tests, a more clear pressure contour from 75 μs to 120 μs can be obtained by the Tait's equation compared to the Mie-Grüneisen EOS. Firstly, the initiated shock wave propagates symmetrically within the surrounding water and hits the Al tube at 18 μs. The pressure at the mid-line wall increases rapidly and the deformation of Al is generated as the Al tube is compressed by the shock wave (see Fig. 6.12 (d-f)). It can be observed that the deformation of the mid-line wall is larger than other part of the tube because the velocity of the mid-line wall is the largest (see Fig. 6.13). With the propagation of the shock wave, the cavitation area occurs at 30 μs near the centerline wall as the rarefaction wave hits the Al tube. Then the cavitation area collapses at 48 μs and the pressure of the cavitation area increases due to the compressive shock wave (see Fig. 6.14), which shows that the occurrence and collapse of cavitation can be predicted in the SPH simulation. In addition, the numerical pressure at mid-line wall are compared against the experimental data [5] (see Fig. 6.14). It can be found that the numerical peak pressures using Mie-Grüneisen and Tait equations are 0.585 GPa and 0.560 GPa, respectively, which are close to the experimental peak pressure 0.620 GPa. A better prediction of the peak pressure can be generated by the Mie-Grüneisen EOS. The creation and collapse of cavitation area is also similar to the experimental phenomenon. The numerical displacements at mid-line wall are also compared with the experimental results, and it can be found that all the relative errors are less than 20% (see Table 6.5). The discrepancy between the numerical pressure and displacements and the experimental results can be attributed to the following reasons, firstly, only the Tait's and Mie-Grüneisen's equations are employed to simulate the liquid compression. The other compressible fluid models will be implemented and compared with the Tait's equation in the near future to obtain simulation results with more accuracy. Secondly, as the calculation of the physical quantities in SPH is based on the selection of kernel function, which is different from the conventional based method, more kernel functions will be tested to investigate its effect on the numerical results. Thirdly, since only the Mie-Grüneisen model is applied for the aluminum impact, more solid impact models, such as the Cowper-Symonds model [101], will be incorporated and tested to simulate the the deformation of structures in an underwater explosion. In summary, the comparison of the SPH method and the experimental data shows that the SPH is applicable for predicting the deformation of underwater explosion to structures.

Table 6.4 Coefficients of Mie-Grüneisen model for water.

$\rho_0(kg/m^3)$	C_0 (km/s)	S_1	S_2	S_3	γ	α	E_0 (J)
1000	1480	2.56	1.986	1.2286	0.5	0	0

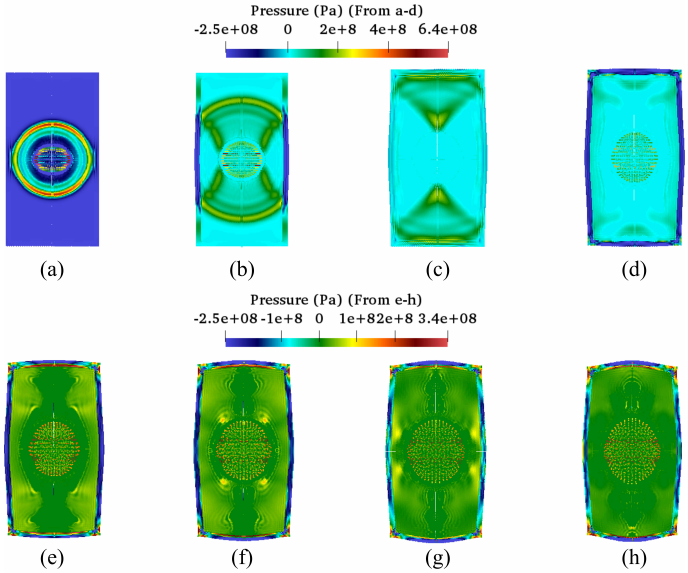

Figure 6.12 The pressure distributions of the underwater explosion within an Al tube at (a) 15 μs; (b) 30 μs; (c) 45 μs; (d) 60 μs; (e) 75 μs; (f) 90 μs; (g) 105 μs; (h) 120 μs.

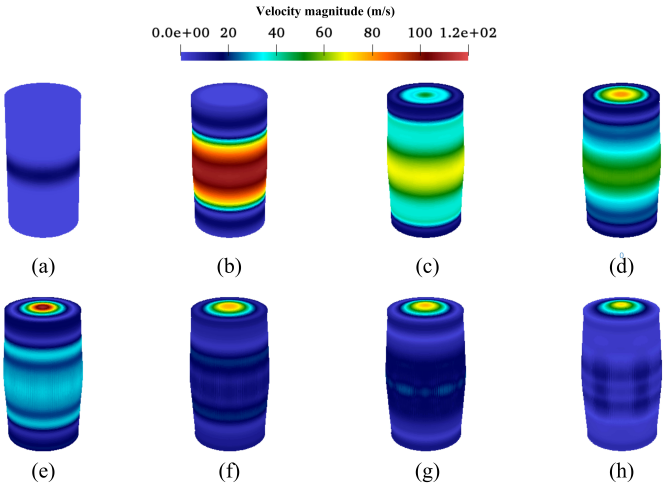

Figure 6.13 The velocity distributions of the underwater explosion within an Al tube (a) 15 μs; (b) 30 μs; (c) 45 μs; (d) 60 μs; (e) 75 μs; (f) 90 μs; (g) 105 μs; (h) 120 μs.

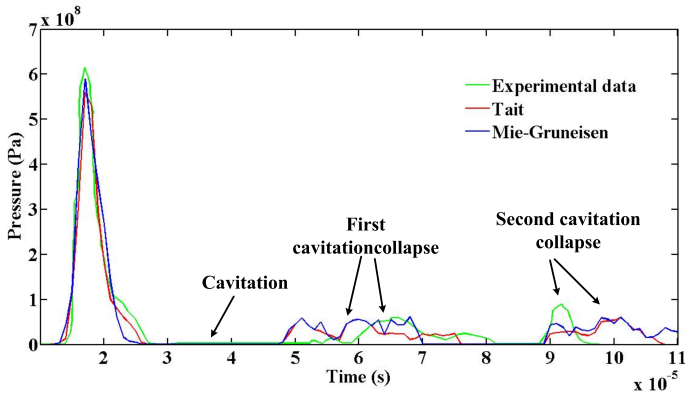

Figure 6.14 The pressure histories at mid-line wall of deformable cylinder using the experimental data [5] and the SPH method.

Table 6.5 Comparison of the simulation and experimental displacement at mid-line wall (mm), in which Error = $\frac{|Si-Ex|}{Ex}$.

Time (msec)	0.01	0.02	0.03	0.04	0.06	0.08	0.1	0.15
Ex (Experiment)	0.0	0.50	1.20	2.00	3.33	4.17	4.65	5.50
Si (Tait)	0.0	0.41	1.00	1.61	2.93	3.85	4.10	5.10
Si (Mie-Grüneisen)	0.0	0.42	1.00	1.70	2.94	3.86	4.12	5.20
Error (Tait) (%)	0.0	18.0	16.6	19.5	12.0	7.67	11.8	7.27
Error (Mie-Grüneisen) (%)	0.0	16.0	16.6	15.0	11.7	7.43	11.3	5.40

6.4 Summary

In this chapter, the SPH method in conjunction with a modified Schmidt model has been used to simulate a fully 3D underwater explosion in a both rigid and deformable (Al) tube. The proposed methodology has been implemented as part of a general 3D in-house SPH code that incorporates the Open-MP parallel programming interface to provide the computational efficiency required to conduct simulations with large numbers of particles. Various components of SPH code have been validated using a number of test cases, namely the Sjögreen test case, a 1D cavitating flow in an open tube test case, a 1D PETN detonation test case and a 3D high-velocity impact test case. After this comprehensive validation, the SPH code has been applied to the simulation of a fully 3D underwater explosion in a rigid cylinder and in a deformable Al tube. The numerical results show that these 3D

SPH predictions of an underwater explosion are in general agreement with other numerical simulations of the problem using alternative approaches, as well as with some available experimental data.

Chapter 7

3D granular impacts using CUDA parallel computing platform

In addition to the investigations of the landmine detonation and underwater explosion, the 3D granular impacts have also been conducted in this thesis. Rather than using the Open-MP programming interface, the CUDA parallel computing platform is used to study the 3D granular impact. The elastoplastic and phase-change models are validated using four test cases in this chapter: namely, the collapse of an axisymmetric sand, the impact force of sand on a rigid wall, head-on collisions of dense granular jets, and the impact of a granular jet with a wave structure on a granular film. The results of SPH simulations with the elastoplastic and phase-change constitutive material models for the four test cases are compared to available experimental data and to numerical data obtained using alternative simulation methodologies (e.g., discrete element method, material point method).

7.1 GPU implementation

7.1.1 GPU solution procedure

The application of SPH for the simulation of granular flow in three dimensions is computationally intensive owing to the large number of particles required for such simulations. From Chapter 4, we can find that the parallelized SPH code using Open-MP can only be 10 times more efficient than run on a CPU. As a consequence, to enable these types of simulations to complete in a reasonable execution time, it is imperative to accelerate the computational workload by parallelization of the SPH simulations on a graphics processing unit (GPU). The parallelization of the SPH methodology on a GPU is depicted in Fig. 7.1. There are a number of steps involved in the implementation of the SPH methodology on a GPU. Firstly, the data describing the initial configuration of the granular impact is loaded into the central

processing unit (CPU). Next, this information is transferred from the CPU to the GPU. The GPU is used to facilitate the following operations: building the neighborhood lists and searching these neighborhood sets (which necessarily involve dynamically changing lists of neighboring particles), determination of the particle interactions (i.e., the calculation of the rates of change of physical quantities), and update of the physical variables which involve the computation of sums over the dynamically evolving neighborhood sets. At the end of this computational process, the information computed by the GPU is transferred from the GPU to the CPU and the relevant numerical data is saved. All the SPH simulations of granular flow reported herein were conducted on a PC with a single NVIDIA Quadro K620 graphics processor. The performance of the in-house SPH code used for our simulations, such as the accuracy and computational efficiency, is described in detail in [75].

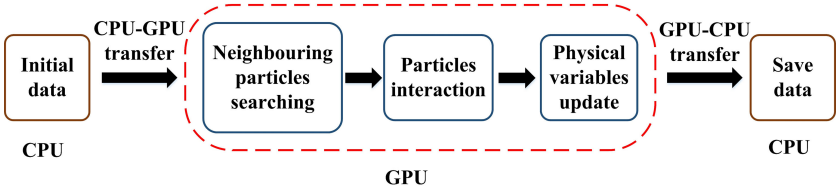

Figure 7.1 Flow diagram depicting the implementation of a 3D SPH methodology on a GPU.

7.1.2 Pseudocode for determination of particle interactions on GPU

The computation of the time development of the physical variables is a compute-intensive process that must be parallelized in order to obtain a good computational performance for a SPH simulation. In consequence, the use of the CUDA programming interface in our in-house SPH code is a key aspect in the acceleration of the computational workload on a GPU. A pseudocode for the algorithm used for the computation of the particle interactions on a GPU is summarized in Algorithm 1 below. The implementation utilizes the CUDA platform (viz., the parallel computing platform and application programming interface developed by NVIDIA for their GPUs).

Algorithm 1 Computation of all particle interactions for particle i

Output: Update the physical variables for particle i

```
1: _ global _ void ParticleInteraction_cuk(. . . );
2: index = blockIdx.x ∗ blockDim.x + threadIdx.x;
3: if (index < particle number) then
4:     Find the neighbour particles;
5:     Calculate the rate of change of the physical quantities;
6: end if
7: Update the physical variables;
```

7.2 Numerical cases

7.2.1 Axisymmetric collapse of dry sand

We first test the phase-change and elastoplastic constitutive models for SPH simulations of the 3D axisymmetric collapse of dry sand. Lube et al. [6] conducted experiments of the axisymmetric collapse of columns of dry sand that was initially contained within a cylindrical column resting on a flat surface (see Fig. 7.2). The nature and mode of collapse of these granular columns is determined by the initial column height-to-halfwidth ratio $a = h_0/d_0$.

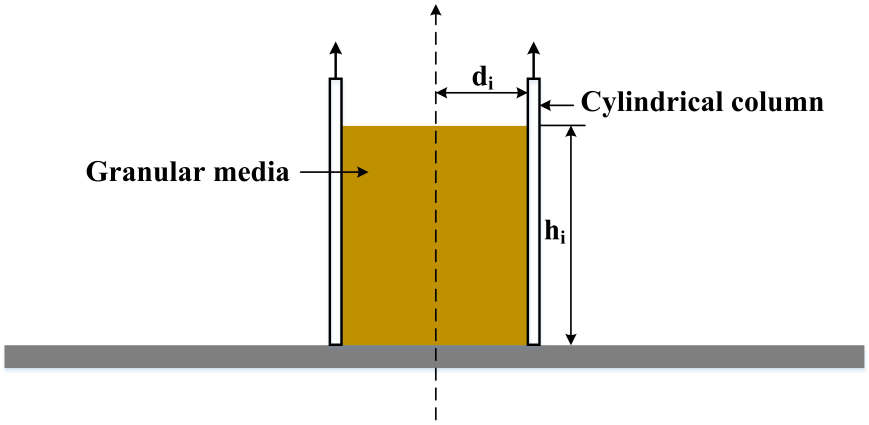

Figure 7.2 Initial setup of the experiment and simulation for the 3D axisymmetric collapse of dry sand, in which the subscript i denotes the initial state or the steady state.

Four different cases involving different ratios of a were simulated using our SPH code and the results of these simulations were compared to the experimental results in order to validate the two constitutive models. Table 7.1 summarizes the basic information for each simulation. The parameters for the elastoplastic and phase-change constitutive models are listed in Table 7.2. These parameters were used for all subsequent SPH simulations reported herein, unless noted otherwise.

The magnitude of the velocity of the granular collapse at two different ratios $a = 0.5$ and 4.0, obtained using the phase-change constitutive model, is shown in Fig. 7.3. It can be seen that in the final phase of the granular collapse, the top surface of the shorter and stouter sand column is flatter than that of the taller and more slender sand column. Qualitatively, it is noted that the overall general shape of the sand pile in the final phase (steady state) of collapse predicted by the simulation is similar to that obtained from the experimental measurements conducted by Lube et al. [6].

The stresses distributions of the sand collapse using the elastoplastic constitutive model are exhibited in Fig. 7.4. The stress in vertical direction yy is proportional to the depth

of the sand. This is consistent with the vertical stress distribution of the sand confined in a cylindrical column and subjected to a gravitational force. Furthermore, the numerical results for the runout distance d_∞ and the final height h_∞ obtained using the phase-change and elastoplastic constitutive models are summarized in Figs 7.5 and 7.6, respectively. Superimposed on these two figures are some experimental measurements of d_∞ and h_∞ obtained by Lube et al. [6]. A perusal of Figs 7.5 and 7.6 shows that the numerical predictions for d_∞ and h_∞ are generally in good conformance with the experimental results. Finally, it is noted that the quality of the current numerical simulations of 3D granular collapse obtained using the SPH framework with both the phase-change and elastoplastic constitutive models are comparable to the 2D sand collapse simulations obtained by Dunatunga and Kamrin [9] using the MPM framework with the phase-change constitutive model.

Table 7.1 Summary of the initial configuration used for four different simulations of the 3D axisymmetric collapse of dry sand.

Case	h_0 (mm)	d_0 (mm)	$a = h_0/d_0$	Initial particle space (mm)	Particles number
1	0.10	0.20	0.5	4.00	482,430
2	0.20	0.20	1.0	5.00	451,969
3	0.40	0.20	2.0	6.25	530,109
4	0.80	0.20	4.0	8.00	475,329

Table 7.2 The parameters of the elastoplastic and phase-change constitutive models for the sand collapse problem [9].

			Elastoplastic constants			Phase-change parameters			
ρ_0 (kg m^{-3})	E (MPa)	ν	ϕ (°)	ψ (°)	c (kPa)	ρ_c (kg m^{-3})	ξ (m$^{1/2}$ kg$^{-1/2}$)	μ_s	μ_2
2450	20.0	0.30	37.0	0.0	0.0	1500	1.1233	0.64	0.84

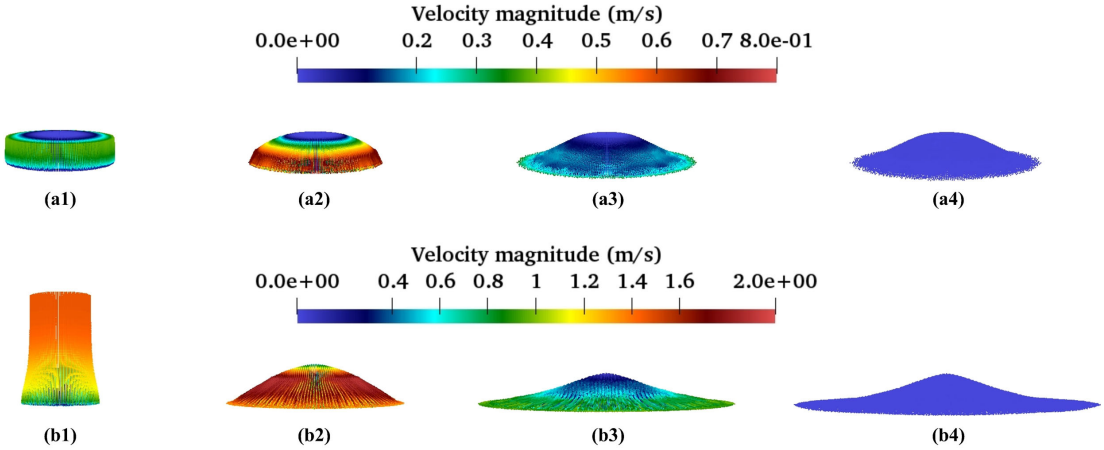

Figure 7.3 Predictions of time development of 3D sand collapse obtained using the phase-change model for $a = 0.5$ (a1–a4) and 4.0 (b1–b4).

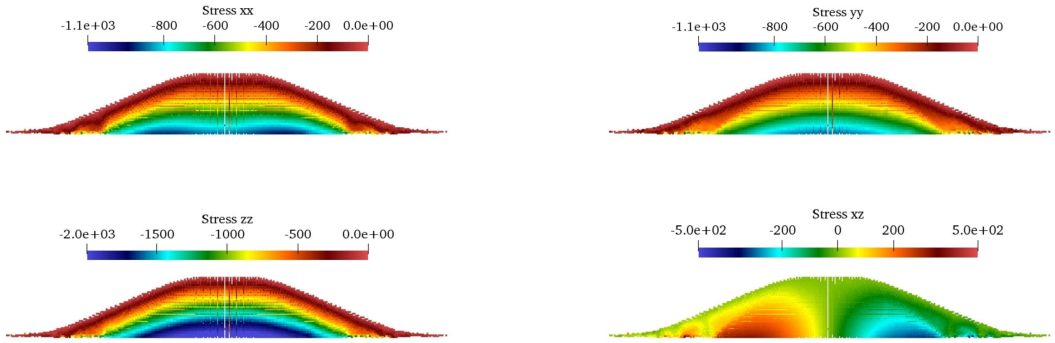

Figure 7.4 The predicted stresses distributions obtained in the SPH framework using the elastoplastic constitutive model for $a = 0.5$.

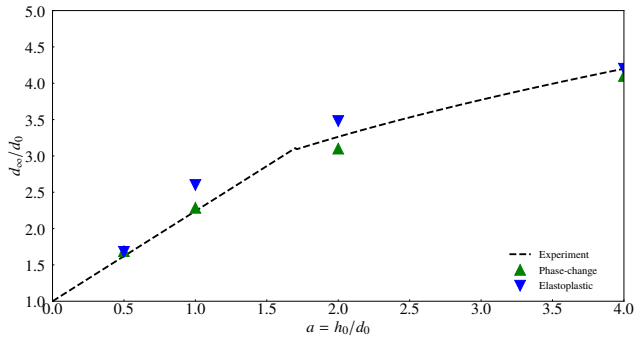

Figure 7.5 Predicted and experimental non-dimensionalized runout distance d_∞ versus initial aspect ratio a Experimental results are taken from Lube et al. [6].

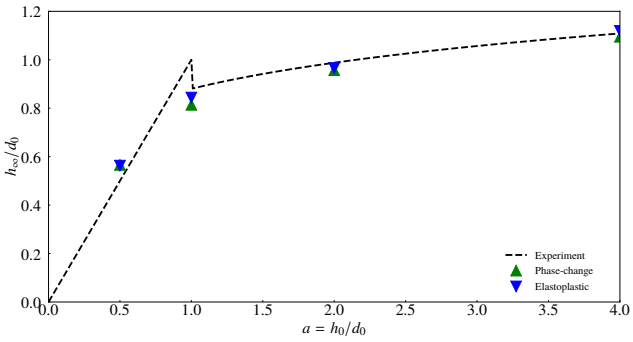

Figure 7.6 Predicted and experimental non-dimensionalized final height h_∞ versus initial aspect ratio a. Experimental results are taken from Lube et al. [6].

We close this subsection with an evaluation of the computational efficiency of our GPU-accelerated SPH code. To this purpose, we will measure the compututational efficiency of the implementation of our GPU-accelerated SPH code in terms of frames per second (FPS), which is the number of computational time steps executed in one second of wall-clock time (see Table 7.3 which summarizes the FPS and total wall-clock execution time T for four test cases involving the simulation of the collapse of a sand pile with an initial aspect ratio of $a = 0.5$). The total physical time of the simulation for all the test cases summarized in Table 7.3 is fixed at a value 0.1 s. A careful examination of this table shows that the FPS decreases as the number of particles used in the simulation increases. More specifically, it is seen that for the case that uses nearly 500,000 particles in the simulation, the FPS achieved ($\approx$ 6.8 time steps per second) is still very good. As mentioned previously, the simulations reported here were conducted on a PC with a single NVIDIA Quadro K620 graphics processor. It is expected that the computational performance reported here will be significantly improved on a more powerful NVIDIA graphics processor, such as the NVIDIA GeForce RTX 2080 Ti.

In order to characterize the acceleration in computational performance provided by the use of a GPU, the SPH simulations summarized in Table 7.3 were also conducted on a PC with a single CPU (AMD Opteron Processor 6320). The speed-up in computational performance between the GPU and CPU is defined as

$$S_p = \frac{\text{FPS on a single GPU}}{\text{FPS on a single CPU}} \,. \tag{7.1}$$

Note that the time required for the input of the data files and the output of the simulation results is excluded from the execution time. The speed-up in the computational performance of the SPH code executed on a single GPU versus that on a single CPU is displayed in Fig. 7.7 for five test cases (four of which have been summarized in Table 7.3). It is seen that a speed-up of up to about a factor of 160 is achieved as the number of particles N used in the

Table 7.3 Computational efficiency of the GPU-accelerated SPH code for simulation of sand collapse with an aspect ratio of $a = 0.5$.

Case	Initial particle spacing (mm)	Number of particles	FPS (s^{-1})	T (s)
1	6.25	170,221	22.32	127
2	5.00	286,333	12.19	288
3	4.00	482,430	6.78	653
4	3.00	752,187	3.96	1324

simulation increases to about 750,000. The speedup suggests our GPU-accelerated SPH implementation has achieved a high parallel computational efficiency.

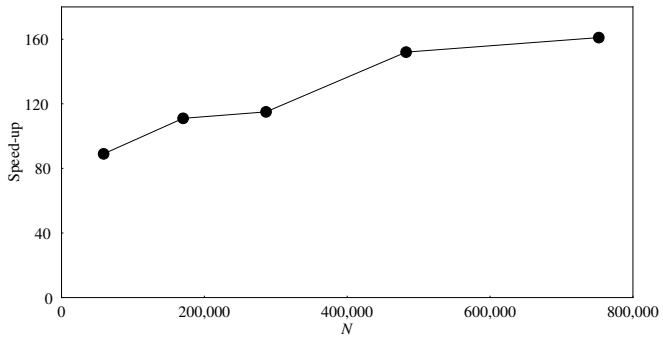

Figure 7.7 The speed-up on a single GPU compared to that on a single CPU of SPH simulations as a function of the number of particles N used in the simulation.

7.2.2 Impact force of sand on a rigid wall

Having completed the validation of the phase-change and elastoplastic constitutive models in the SPH framework using a case study involving the axisymmetric collapse of dry sand, this numerical framework will now be applied to investigate the phenomenon of granular impacts. Moriguchi et al. [102] conducted experimental measurements of the impact force exerted on a rigid wall resulting from the impingement of dry Toyoura fine sand released from an inclined flume. The sand was initially confined inside a box at the top of the flume. This material was released through a side door, and the sand impacted a rigid wall at the bottom of the flume. The impact force exerted by the sand on the rigid wall was measured as a function of time using a sensor attached to the wall barrier.

In this subsection, we will conduct a 3D numerical simulation of this experiment using SPH with the phase-change constitutive model. The initial configuration for the simulation is shown in Fig. 7.8. The length and height of the sand box are 50 cm and 30 cm, respectively. The total mass of the sand contained initially in the box is 50 kg. The density of the granular material (sand) is $\rho_0 = 1340$ kg m^{-3} and the critical density is $\rho_c = 500$ kg m^{-3}. The initial particle spacing used in the simulation is 10 mm. A total of 123,012 particles were used in the SPH simulation. Three layers of dummy particles are used to impose the no-slip boundary condition along the solid wall of the incline. The total physical time simulated using the SPH methdology was 3 s. The computational (wall-clock) time required to complete this simulation was 72 minutes.

The results for the simulation of granular impact down a 45° inclined flume obtained using SPH with the phase-change constitutive model is presented in Fig. 7.9. The sand moves downward gradually owing to the gravitational force. The magnitude of the velocity (speed) of the sand increases from zero to almost 4.5 m s^{-1} during this movement. After about 0.70 s after the initial release, the sand impacts the rigid wall and stops almost immediately after the impact. In consequence, the sand at the bottom of the flume accumulates at the rigid wall and this pile of sand grows in size with increasing time. At the end of the process, the pile of sand reaches the top of the wall barrier and flows out of the flume. This dynamic behavior of the sand obtained from the numerical simulations is in general agreement with both the experimental measurements reported by Moriguchi et al. [102] and the simulations conducted by Neto and Borja [47]. The dynamic behavior of the sand obtained in the SPH framework using the elastoplastic constitutive model is similar to that obtained using the phase-change constitutive model. However, it is noted that using the elastoplastic constitutive model, the sand is predicted to impact the rigid wall at 0.65 s after the initial release, which occurs earlier than the prediction provided by the phase-change constitutive model.

The impact force exerted by the sand on the rigid wall is calculated using equation (2.23). This equation required the specification of the normal vector $\boldsymbol{n} = (n^\alpha)$. For the current case, the vector normal to the rigid wall at the bottom of the flume for an inclination angle of 45° is $\boldsymbol{n} = \left(\frac{\sqrt{2}}{2}, 0, \frac{\sqrt{2}}{2}\right)$. The relative error between the numerical prediction F_w and the experimental value F_E of the impact force is determined using

$$R_{\text{err}} = \frac{|F_W - F_E|}{F_W} \,. \tag{7.2}$$

Figure 7.10 exhibits the predicted time variation of the impact force obtained from our SPH simulations using both the phase-change and elastoplastic constitutive models. The predicted peak impact force obtained using the phase-change constitutive model is 192 N. This predicted value for the peak impact force is larger than the measured value of the peak impact force obtained by Moriguchi et al. [102]. More specifically, the overprediction

of the peak impact force is about 3.2% (viz., the relative error is 0.032). It is noted that the prediction of the peak impact force obtained from our SPH simulations with the phase-change constitutive model is significantly better than that obtained from either our SPH simulations with the elastoplastic constitutive model or the numerical simulations conducted by Neto and Borja [47]. In the latter two cases, the predicted peak value of the impact force was about 212 N which significantly overpredicts the measured value of the peak impact force.

After the rapid initial increase to its peak value, the impact force decreases gradually to value of about 160 N. This decrease occurs because some of the sand flows out of the bottom boundary and the velocity of the sand is reduced after its initial impact with the rigid wall. In general, it is noted that SPH simulations with the phase-change constitutive model is capable of capturing the dynamical behavior of the impact of the sand against the rigid wall. Furthermore, these simulations give generally good predictions for the time variation of the impact force. The slight overestimation of peak impact force is probably due to force contribution from the soil viscosity and the boundary implementation used here. The effects of the soil viscosity, which has the tendency to slow down the granular flow and reduce the impact force, has not been incorporated in our numerical simulations. In addition, it is expected once a more appropriate model for the calculation of the stress tensor of the boundary particles has been developed, its inclusion in our numerical simulation will lead probably to more accurate predictions of the impact force.

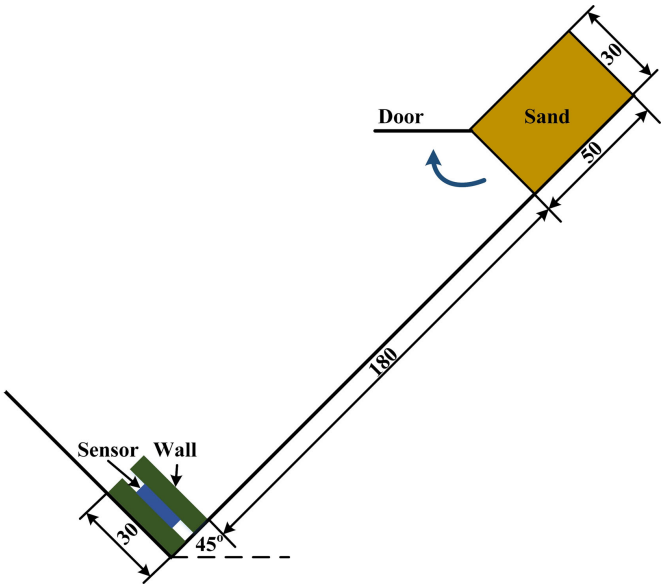

Figure 7.8 The initial configuration of sand on an inclined flume. All the dimensions shown here are in cm.

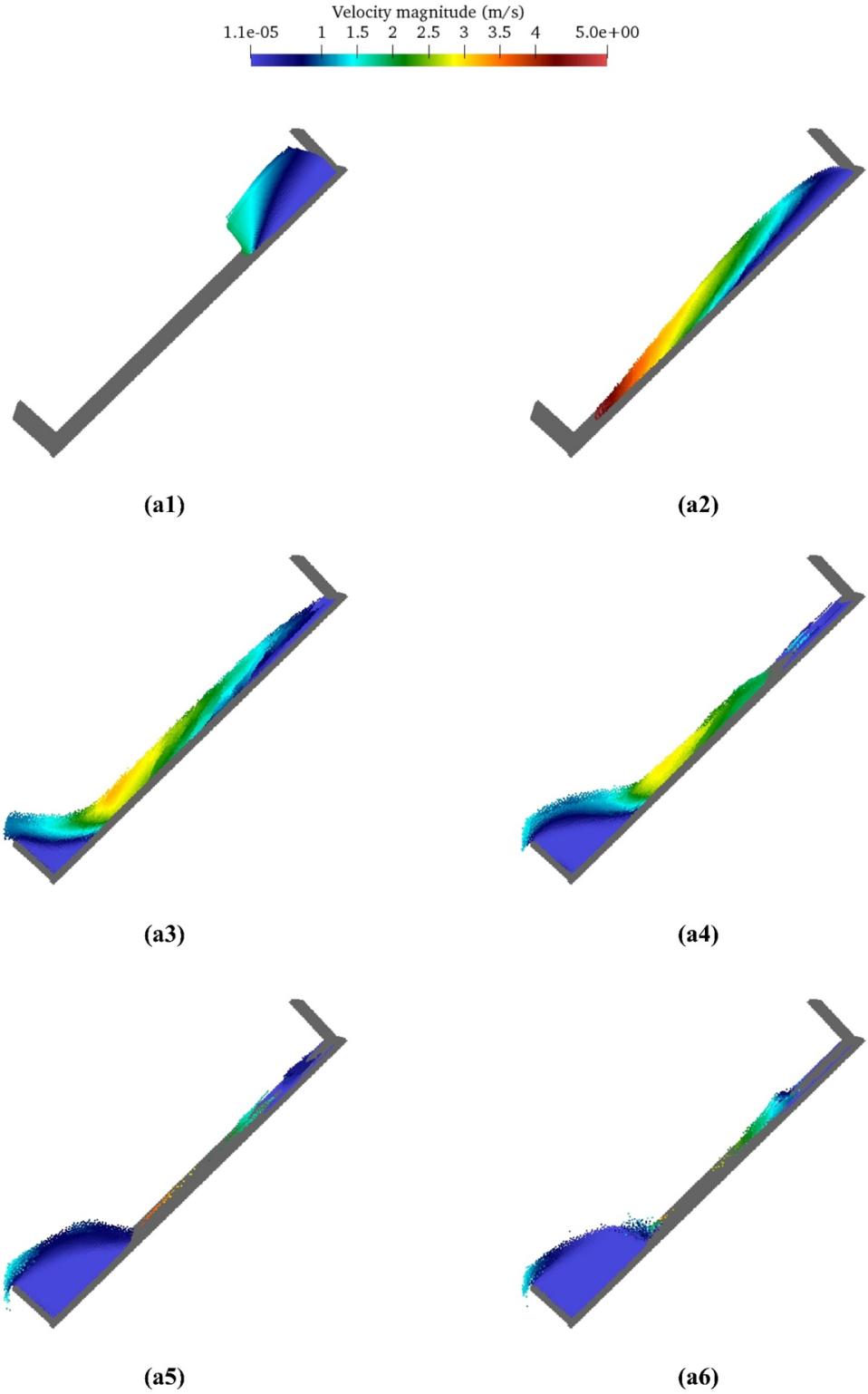

Figure 7.9 The magnitude of the velocity of granular impact on 45° inclined flume obtained using SPH with the phase-change constitutive model at six different times: namely, at 0.2 s (a1), at 0.6 s (a2), at 1.0 s (a3), at 1.4 s (a4), at 1.8 s (a5), and at 2.2 s (a6).

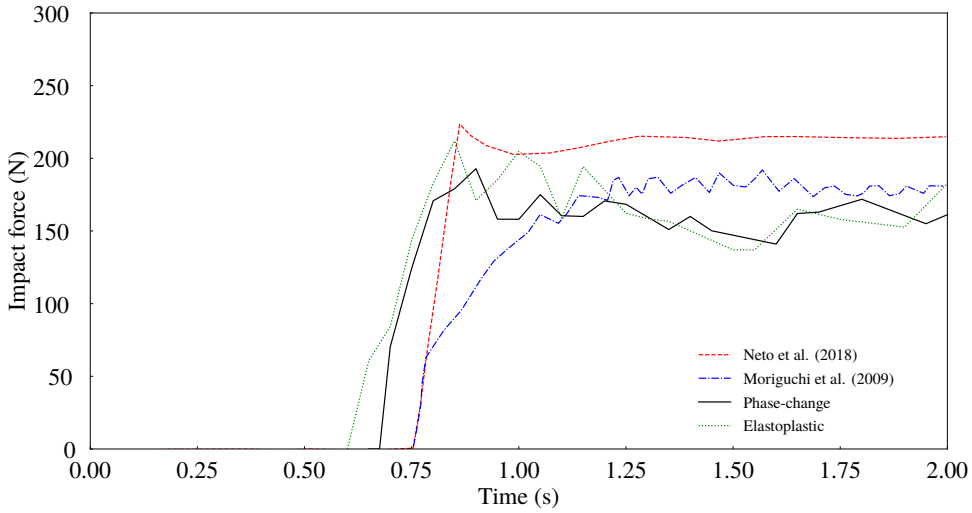

Figure 7.10 Time variation of the impact force for a flume inclination of 45°.

7.2.3 Head-on collisions of dense granular jets

In this subsection, we investigate the 3D head-on collisions of dense granular jets. A study of the physical mechanisms involved in the collisions of granular jets will enhance our understanding of the loads applied to structures by the impact of granular matter on them at high velocity. Ellowitz [62] conducted 2D simulations of head-on collisions of dense granular jets having equal speeds using DEM. Here, we extend this effort to consider fully 3D simulations of dense granular jet collisions using the SPH framework. To this purpose, two granular jets having different sizes will be considered in our simulations: namely, the diameter of the first jet is taken to be $2R$ and that of the second jet is taken to be $2kR$, where $0 \leq k \leq 1$. The centers of these two jets are assumed to be aligned, and their initial velocities are both v_0 in magnitude. These two jet velocities are in opposite directions, so that the two jets undergo a head-on collision. The ejecta angle ψ_0, which is the maximum angle between the tangent line of the surface of the jet to the horizontal direction, and the velocity u_0 of the impact center point at the interface of the two jets are used to characterize the impact process (see Fig. 7.11). The initial configurations used for three different simulation scenarios for head-on collisions of the granular jets are summarized in Table 7.4.

Figure 7.12 shows the predicted results obtained using SPH with the phase-change constitutive model for the head-on collision of two granular jets with the initial configuration specified by scenario 1 (cf. Table 7.4). It is noted that the ejecta angle of the granular jet with the larger diameter increases during the impact process, and its configuration after the impact is similar to the 2D geometry described in Ellowitz [62]. The impact center

Table 7.4 Initial configuration for three different simulations of head-on collisions of dense granular jets.

Scenario	R (mm)	k (mm)	v_0 (m s^{-1})	Initial particle space (mm)	Particles number
1	0.10	0.50	10.0	4.00	369,000
2	0.10	1.00	10.0	4.00	592,800
3	0.10	0.25	10.0	4.00	314,400

drifts at a constant speed of about $u_0 = 0.14$ m s^{-1}, which is consistent with the simulations described in [62]. Figure 7.13 exhibits the stress and strain distributions obtained using SPH with the phase-change constitutive model at a time of 0.02 s. A persual of this figure shows that the stress in the horizontal direction assumes the largest values within the impact area. The shear strain and stress in the yz direction are antisymmetric with respect to horizontal x direction.

The effect of different diameters of the two jets (as characterized by the coefficient k) on the velocity of the impact center has also been studied. To this purpose, the initial configurations for the colliding granular jets are summarized in scenarios 2 and 3 (cf. Table 7.4). The constant velocity u_0 of the impact center is 0 m s^{-1} for scenario 2 where the radii of the two jets were equal (viz., $k = 1$) and 3.96 m s^{-1} for scenario 3 where the radius of one jet is 1/4 that of the other jet (viz., $k = 0.25$). It seen that a smaller value for k results in a larger value for the velocity u_0 of the impact center, a result that is in conformance with the numerical simulations conducted by Ellowitz [62]. The results of our numerical simulations have shown that the application of the SPH methodology with the phase-change constitutive model provides a good alternative scheme to study impact of two granular jets.

In order to demonstrate the ability of the proposed SPH methodology to capture phase

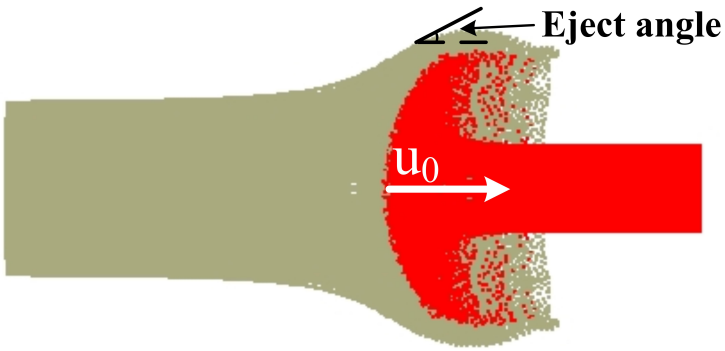

Figure 7.11 A sketch of the ejecta angle and the velocity u_0 of the impact center.

changes in the collision of two granular jets, we set the initial density of the disconnected granular jets to have a value of $\rho = 1200$ kg m^{-3}. This value for the initial jet density is less than the critical density which has a value of $\rho_c = 1500$ kg m^{-3}. Otherwise, initial conditions for this case are exactly the same as those of scenario 3. The results of the simulation of the impact of the two granular jets for this case obtained using SPH with the phase-change constitutive model are displayed in Fig. 7.14. An examination of this figure shows that the two disconnected jets undergoes a process of densification after they collide with the each other. This simulation highlights the ability of the SPH methodology to model large inhomogeneous deformations of the granular material. These results suggest that the effects of the granular particle size and fracture on the interaction of high-velocity granular slugs can be investigated using the proposed SPH methodology.

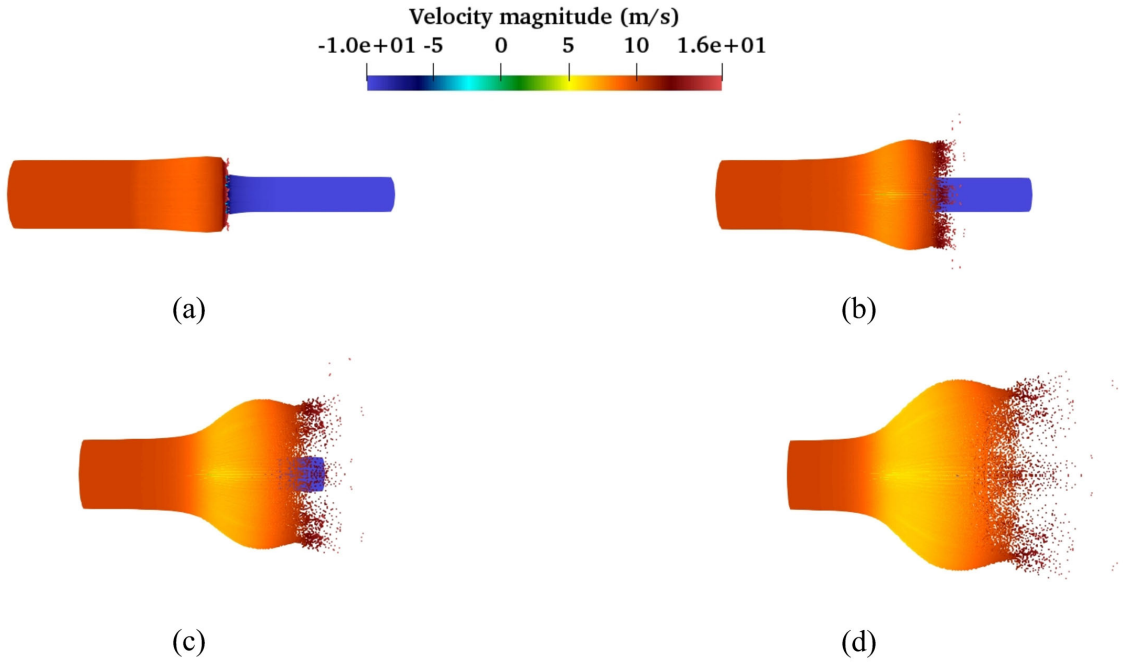

Figure 7.12 The magnitude of the velocity arising from the head-on collision of two dense granular jets predicted using SPH with the phase-change constitutive model for an initial configuration given by scenario 1.

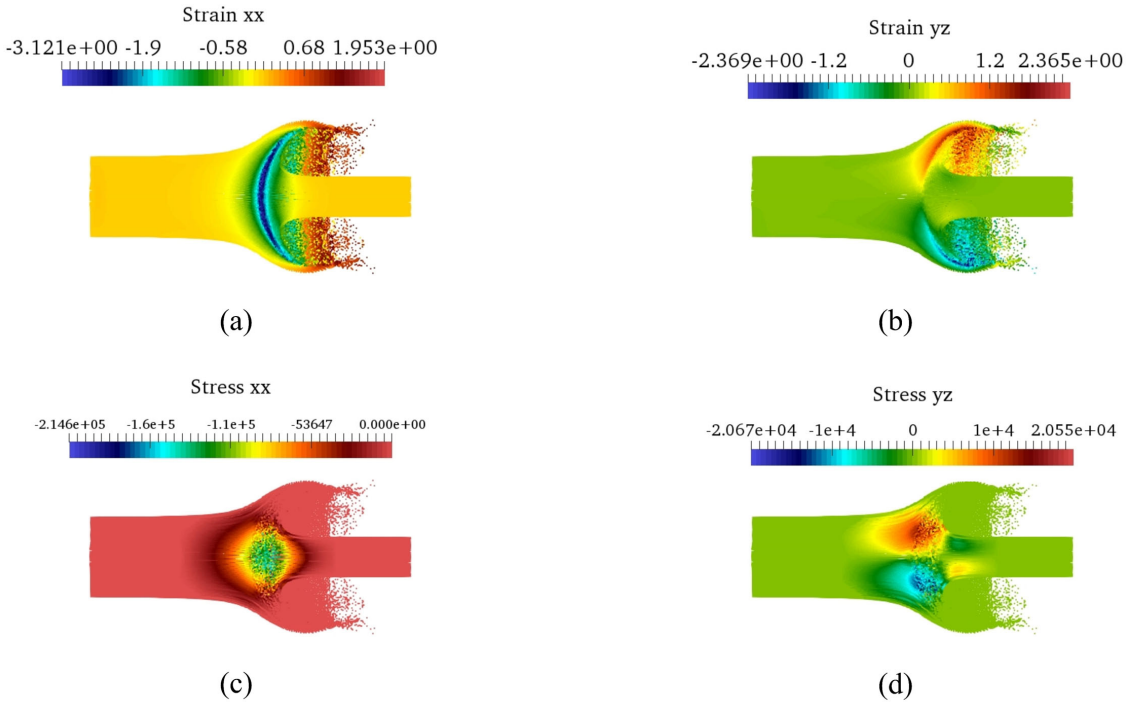

Figure 7.13 The stress and strain distributions arising from head-on granular impact obtained using SPH with the phase-change constitutive model.

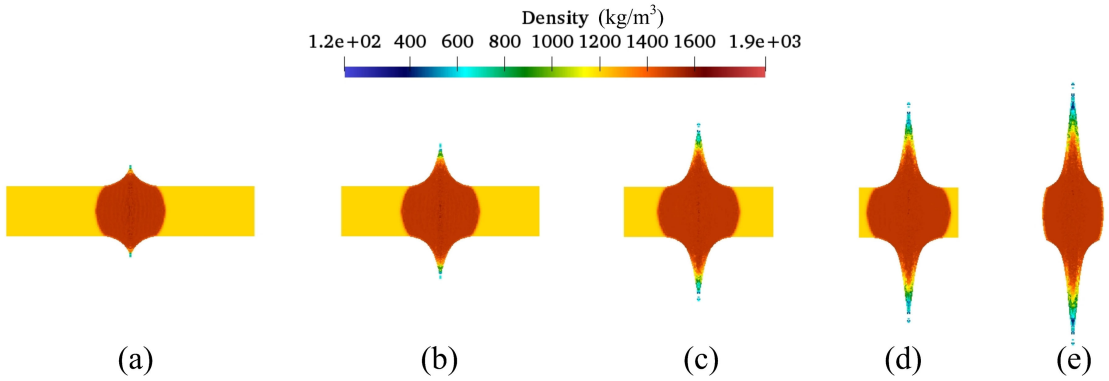

Figure 7.14 Numerical simulation of the process of densification of two colliding granular jets obtained using SPH with the phase-change constitutive model.

7.2.4 The impact of granular jet with a wave structure on a granular film

An experimental study of the liquid-like wave structures on a granular film resulting from a granular jet impact has been described by Shi et al.[103]. In this study, the initial

configuration of the particles is a sinusoidal wave. In particular, the horizontal motion of the center particles at the jet exit is characterized by

$$y = A_0 \sin(2\pi f_0 t) \ , \tag{7.3}$$

where A_0 and f_0 are the amplitude and frequency of the initial granular jet, respectively, and t is the time. In this subsection, we simulate the liquid-like wave structure on a granular film using the SPH methodology with both the phase-change and elastoplastic constitutive models.

To this purpose, the wave structure generated by an amplitude of $A_0 = 0.002$ m and a frequency of $f_0 = 160$ Hz for the initial granular jet has been investigated using the SPH methdology. The initial particle spacing is 0.002 m and 800,000 particles were used in this simulation. The initial velocity of the granular jet is 4.0 m s^{-1}. Figure 7.15 exhibits the experimental wave structure on the granular film measured by Shi et al. [103] and that obtained from the SPH simulations using both the elastoplastic and phase-change constitutive models. It is noted that the wave structures obtained from the two simulations are in very good agreement with the experimental results.

The reason for the wave structures seen in Fig. 7.16 is that the initial configuration of the granular media is antisymmetric with respect to vertical z-direction and the periodic oscillation of the resulting disturbance results in the generation of wave structure. Furthermore, the effects of the amplitude and the frequency of the disturbance in the granular jet on the wave structure have also been investigated using SPH similations. The results of these investigations are summarized in Fig. 7.16. In particular, Fig. 7.16 (a1–a4) exhibit the wave structures for a frequency of $f_0 = 160$ Hz for a series of increasing values of the amplitude A_0: namely, for $A_0 = 0.0005$ m, 0.001 m, 0.002 m, and 0.003 m. Similarly, Fig. 7.16 (b1–b4) display the wave structure for an amplitude of $A_0 = 0.002$ m for a series of increasing frequencies f_0: namely, for $f_0 = 80$ Hz, 120 Hz, 160 Hz, and 240 Hz. A careful examination of these results shows that the wave structure disappears when the amplitude of the disturbance decreases below a certain value as the disturbance then becomes too small to generate a wave structure (cf. Fig. 7.16 (a1)). The wavelength of the wave structure on the granular film increases with a decrease in the frequency of the disturbance as is evident from a perusal Fig. 7.16 (b1–b4). The results reported here demonstrate that the SPH methodology used in conjunction with the phase-change and elastoplatic constitutive models can be used to predict the nature of the wave structures on a granular film.

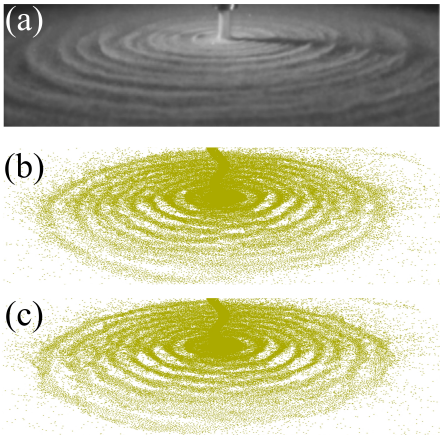

Figure 7.15 Wave structures on a granular film obtained from (a) an experimental study [7] and from SPH simulations with (b) the phase-change and (c) the elastoplastic constitutive models. The numerical simulations were conducted with initial amplitude of $A_0 = 0.002$ m and a frequency of $f_0 = 160$ Hz.

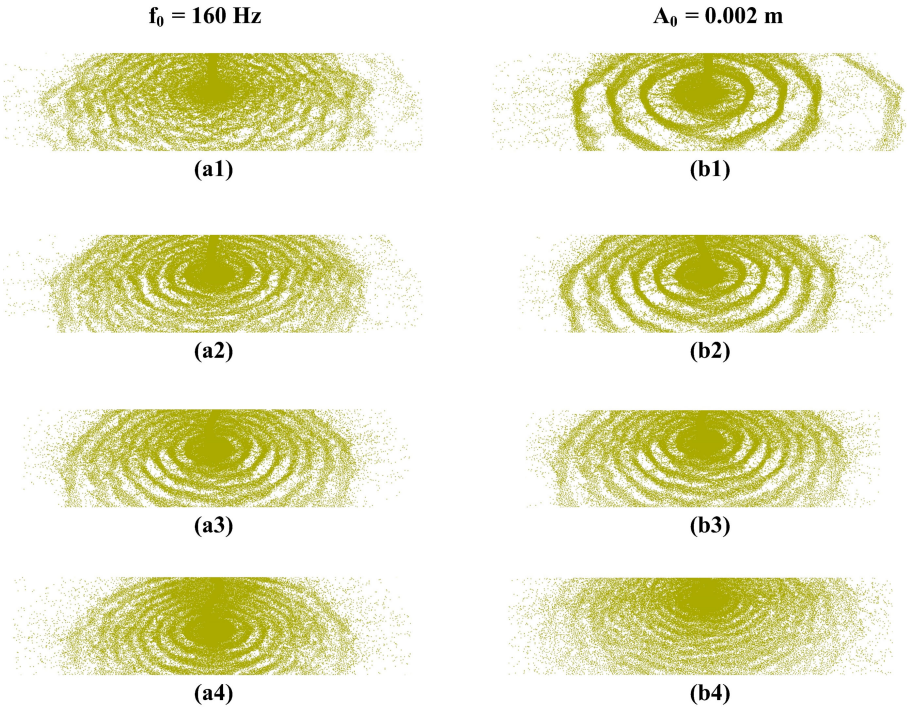

Figure 7.16 Wave structures on a granular film obtained at an initial frequency of $f_0 = 160$ Hz and for amplitudes of $A_0 = 0.0005$ m (a1), 0.001 m (a2), 0.002 m (a3), and 0.003 m (a4) and at an initial amplitude of $A_0 = 0.002$ m and for frequencies of $f_0 = 80$ Hz (b1), 120 Hz (b2), 160 Hz (b3), and 240 Hz (b4).

7.3 Summary

In this chapter, the elastoplastic and phase-change constitutive models are employed to study the 3D granular impacts. The CUDA parallel programming interface for an NVIDIA GPU has been used to improve the computational efficiency of the SPH computations for granular flows. To demonstrate the feasibility of the proposed approach, SPH simulations were conducted for four different cases involving granular flow. The results of these simulations have been compared to available experimental data and to numerical data obtained from alternative simulation methdologies, which shows that the SPH method can tackle the granular impacts problems well.

Chapter 8

Conclusions and future plan

8.1 Conclusions and novelties

The applications of the SPH method in conjunction with the Open-MP and CUDA parallel programming interfaces on the 3D landmine detonation, the underwater explosion, and the granular impacts have been presented in the thesis. The conclusions and novelties are summarized as follows:

1) Firstly, the in-house SPH code was parallelized using the Open-MP programming interface to achieve a high computational efficiency. The 3D shaped-charge detonation has been tested to evaluate the computational performance of the parallel in-house SPH code. The numerical results show that the computational time reduces rapidly with the increase of the threads, and the speedup ratio can increase to around 10 when using 24 threads. Thus, the Open-MP programming interface can be employed to parallelize the most time-consuming sections in the SPH code so that the calculation efficiency of the SPH program can be enhanced significantly.

2) Secondly, the elastoplastic and the hypoplastic constitutive models were incoporated in SPH to simulate 2D and 3D landmine detonations. These two constitutive models have been validated by the sand collapse problem. Then the 2D and 3D landmine detonation and their effects on structures have been studied using the SPH method in conjunction with these two models. Both of the elastoplastic and hypoplastic constitutive models are appropriate for the 3D landmine detonation simulation. The numerical solutions such as the shape of soil ejecta and the heights of the soil fragmentation at representative times are in good agreement with the experimental results, which shows that the SPH method can deal with the extremely large deformation problems very well. To our best knowledge, this is the first time these two constitutive models are implemented in SPH to investigate the landmine detonation problems.

3) Afterwards, the 3D underwater explosion within a cylindrical rigid and aluminum

tube has been investigated. The numerical results are compared against the experimental data and other available numerical results, which shows that the SPH method is suitable for predicting the underwater explosion and the deformation of the structures. The cavitation phenomenon in an underwater explosion in a cylinder (rigid or deformable) is well predicted generally using the SPH method in conjunction with the modified Schmidt cavitating model. Predictions of the pressure distribution and the deformation of the structure obtained from the SPH method are generally in reasonable to good conformance with experimental measurements as well as with other numerical simulations. To the best of our knowledge, this appears to be first time that a fully explicit 3D underwater explosion in either a rigid or a deformable cylinder incorporating properly the cavitation phenomenology has been successfully simulated using the SPH method.

4) Finally, fully 3D granular impact problems involving large deformations can be addressed successfully using the SPH methodology with either the phase-change or the elastoplastic constitutive models. To the best of our knowledge, this is the first time that the phase-change constitutive model has been implemented within SPH framework and successfully used for the simulation of 3D granular impact problems. The SPH methodology can be used to efficiently simulate granular impact problems with a large number of particles on readily available commodity GPUs. The 3D impact of a granular jet with a wave structure on the granular film and the head-on collisions of dense granular jets have been successfully simulated using the SPH methodology for the first time.

8.2 Future plan

The future research can be conducted in the following aspects. In the aspect of applications,

1) More constitutive models, such as the cam-clay and the modified cam-clay constitutive models [104], can be implemented in the in-house SPH code to investigate the dynamic behavior of soil explosion further.

2) The solid impact Cowper-Symonds model will be implemented and incorporated into our SPH code. The damage to various structures arising from an underwater explosion will be conducted using these models and validated using available experimental data in order the assess the capabiity of the modeling scheme to predict structural damage.

3) The SPH method can be coupled with the conventional FEM method to investigate the fluid-structure interactions, in which SPH is utilized to model fluid flow, while FEM is employed to simulate the dynamic response of thin-walled structures.

4) The CUDA parallel computing platform and programming model, which facilitates the implementation of parallelization of the present SPH solver on GPUs, will be implemented to simulate explosion in soil in three dimensions involving large number of particles.

In the theoretical aspect,

1) The more general technique which can tackle the interfaces in multiphase flows with large density ratio within the SPH framework with higher accuracy and stability will be investigated in the future.

2) The implementation of the boundary condition will be studied further to obatin the numerical results with higher accuracy.

3) More robust approach for the evolution of the smoothing length h will be proposed for the simulations of the problems with shock wave.

References

[1] S. E. Rigby, S. D. Fay, S. D. Clarke, A. Tyas, J. J. Reay, J. A. Warren, M. Gant, I. Elgy, Measuring spatial pressure distribution from explosives buried in dry Leighton Buzzard sand, International Journal of Impact Engineering 96 (2016) 89–104, ISSN 0734-743X.

[2] F. Plassard, J. Mespoulet, P. Hereil, Hypervelocity impact of aluminium sphere against aluminium plate: Experiment and LS-DYNA correlation, in: Proceedings of the 8th European LS-DYNA Users Conference, Strasbourg, France, 23–24, 2011.

[3] A. Jafarian, A. Pishevar, An exact multiphase Riemann solver for compressible cavitating flows, International Journal of Multiphase Flow 88 (2017) 152–166.

[4] T. Liu, B. Khoo, W. Xie, Isentropic one-fluid modelling of unsteady cavitating flow, Journal of Computational Physics 201 (1) (2004) 80–108.

[5] J. A. Wardlaw, R. McKeown, A. Luton, Coupled hydrocode prediction of underwater explosion damage, Tech. Rep., Naval Surface Warfare Center, Indian Head MD, 1998.

[6] G. Lube, H. E. Huppert, R. S. J. Sparks, M. A. Hallworth, Axisymmetric collapses of granular columns, Journal of Fluid Mechanics 508 (2004) 175–199.

[7] Z. H. Shi, W. F. Li, Y. Wang, H. F. Liu, F. C. Wang, DEM study of liquid-like granular film from granular jet impact, Powder Technology 336 (2018) 199–209.

[8] C. Peng, W. Wu, H. S. Yu, C. Wang, A SPH approach for large deformation analysis with hypoplastic constitutive model, Acta Geotechnica 10 (6) (2015) 703–717.

[9] S. Dunatunga, K. Kamrin, Continuum modelling and simulation of granular flows through their many phases, Journal of Fluid Mechanics 779 (2015) 483–513.

[10] D. M. Bergeron, R. Walker, C. Coffey, Detonation of 100-gram anti-personnel mine surrogate charges in sand, a test case for computer code validation, National Defence, Defence Research Establishment Suffield, 1998.

[11] S. D. Clarke, S. D. Fay, J. A. Warren, A. Tyas, S. E. Rigby, J. J. Reay, R. Livesey, I. Elgy, Geotechnical causes for variations in output measured from shallow buried charges, International Journal of Impact Engineering 86 (2015) 274–283.

[12] J. M. Brett, G. Yiannakopolous, A study of explosive effects in close proximity to a submerged cylinder, International Journal of Impact Engineering 35 (4) (2008) 206–225.

[13] T. Rabczuk, T. Belytschko, Cracking particles: a simplified meshfree method for arbitrary evolving cracks, International Journal for Numerical Methods in Engineering 61 (13) (2004) 2316–2343.

[14] T. Rabczuk, P. M. A. Areias, T. Belytschko, A meshfree thin shell method for non-linear

dynamic fracture, International Journal for Numerical Methods in Engineering 72 (5) (2007) 524–548.

[15] T. Rabczuk, T. Belytschko, A three-dimensional large deformation meshfree method for arbitrary evolving cracks, Computer Methods in Applied Mechanics and Engineering 196 (29-30) (2007) 2777–2799.

[16] T. Rabczuk, G. Zi, S. Bordas, H. Nguyen-Xuan, A simple and robust three-dimensional cracking-particle method without enrichment, Computer Methods in Applied Mechanics and Engineering 199 (37-40) (2010) 2437–2455.

[17] T. Rabczuk, S. Bordas, G. Zi, On three-dimensional modelling of crack growth using partition of unity methods, Computers & Structures 88 (23-24) (2010) 1391–1411.

[18] R. A. Gingold, J. J. Monaghan, Smoothed particle hydrodynamics: theory and application to non-spherical stars, Monthly notices of the Royal Astronomical Society 181 (3) (1977) 375–389.

[19] L. B. Lucy, A numerical approach to the testing of the fission hypothesis, The Astronomical Journal 82 (1977) 1013–1024.

[20] J. Swegle, D. Hicks, S. Attaway, Smoothed particle hydrodynamics stability analysis, Journal of Computational Physics 116 (1) (1995) 123–134.

[21] J. P. Morris, Analysis of smoothed particle hydrodynamics with applications, Monash University Australia, 1996.

[22] J. J. Monaghan, SPH without a tensile instability, Journal of Computational Physics 159 (2) (2000) 290–311.

[23] C. Zhang, X. Y. Hu, N. A. Adams, A generalized transport-velocity formulation for smoothed particle hydrodynamics, Journal of Computational Physics 337 (2017) 216–232.

[24] W. K. Liu, S. Jun, Y. F. Zhang, Reproducing kernel particle methods, International journal for numerical methods in fluids 20 (8-9) (1995) 1081–1106.

[25] J. Chen, J. Beraun, T. Carney, A corrective smoothed particle method for boundary value problems in heat conduction, International Journal for Numerical Methods in Engineering 46 (2) (1999) 231–252.

[26] M. B. Liu, G. R. Liu, Restoring particle consistency in smoothed particle hydrodynamics, Applied numerical mathematics 56 (1) (2006) 19–36.

[27] J. Shao, H. Li, G. Liu, M. Liu, An improved SPH method for modeling liquid sloshing dynamics, Computers & Structures 100 (2012) 18–26.

[28] D. Violeau, B. D. Rogers, Smoothed particle hydrodynamics (SPH) for free-surface flows: past, present and future, Journal of Hydraulic Research 54 (1) (2016) 1–26.

[29] S. Adami, X. Y. Hu, N. A. Adams, A generalized wall boundary condition for smoothed particle hydrodynamics, Journal of Computational Physics 231 (21) (2012) 7057–7075.

[30] L. D. Libersky, A. G. Petschek, T. C. Carney, J. R. Hipp, F. A. Allahdadi, High strain Lagrangian hydrodynamics: a three-dimensional SPH code for dynamic material response, Journal of computational physics 109 (1) (1993) 67–75.

[31] P. Randles, L. D. Libersky, Smoothed particle hydrodynamics: some recent improvements and applications, Computer methods in applied mechanics and engineering 139 (1-4) (1996) 375–408.

[32] G. R. Johnson, Numerical algorithms and material models for high-velocity impact computations, International Journal of Impact Engineering 38 (6) (2011) 456–472.

[33] T. Rabczuk, J. Eibl, Simulation of high velocity concrete fragmentation using SPH/MLSPH, International Journal for Numerical Methods in Engineering 56 (10) (2003) 1421–1444.

[34] T. Rabczuk, J. Eibl, Modelling dynamic failure of concrete with meshfree methods, International Journal of Impact Engineering 32 (11) (2006) 1878–1897.

[35] T. Rabczuk, J. Eibl, L. Stempniewski, Numerical analysis of high speed concrete fragmentation using a meshfree Lagrangian method, Engineering fracture mechanics 71 (4-6) (2004) 547–556.

[36] K. MAEDA, M. SAKAI, Development of seepage failure analysis procedure of granular ground with Smoothed Particle Hydrodynamics (SPH) method, Journal of applied mechanics 7 (2004) 775–786.

[37] H. H. Bui, R. Fukagawa, K. Sako, S. Ohno, Lagrangian meshfree particles method (SPH) for large deformation and failure flows of geomaterial using elastic–plastic soil constitutive model, International Journal for Numerical and Analytical Methods in Geomechanics 32 (12) (2008) 1537–1570.

[38] W. Chen, T. Qiu, Numerical simulations for large deformation of granular materials using smoothed particle hydrodynamics method, International Journal of Geomechanics 12 (2) (2011) 127–135.

[39] C. Peng, W. Wu, H. S. Yu, Hypoplastic constitutive model in SPH, in: Computer methods and recent advances in geomechanics-Proceedings of the 14th International Conference of International Association for Computer Methods and Recent Advances in Geomechanics, IACMAG, 1863–1868, 2014.

[40] C. Peng, X. G. Guo, W. Wu, Y. Q. Wang, Unified modelling of granular media with Smoothed particle hydrodynamics, Acta Geotechnica 11 (6) (2016) 1231–1247.

[41] X. Lai, B. Ren, H. Fan, S. Li, C. Wu, R. A. Regueiro, L. Liu, Peridynamics simulations of geomaterial fragmentation by impulse loads, International Journal for Numerical and Analytical Methods in Geomechanics 39 (12) (2015) 1304–1330.

[42] B. Ren, H. F. Fan, G. L. Bergel, R. A. Regueiro, X. Lai, S. F. Li, A peridynamics-SPH coupling approach to simulate soil fragmentation induced by shock waves, Computational Mechanics 55 (2) (2015) 287–302.

[43] H. F. Fan, G. L. Bergel, S. F. Li, A hybrid peridynamics – SPH simulation of soil fragmentation by blast loads of buried explosive, International Journal of Impact Engineering 87 (2016) 14–27, ISSN 0734-743X.

[44] H. F. Fan, S. F. Li, A Peridynamics-SPH modeling and simulation of blast fragmentation of soil under buried explosive loads, Computer Methods in Applied Mechanics and Engineering 318 (2017) 349–381.

[45] H. Fan, S. Li, Parallel peridynamics-SPH simulation of explosion induced soil fragmentation by using OpenMP, Computational Particle Mechanics 4 (2) (2017) 199–211.

[46] E. J. Fern, K. Soga, The role of constitutive models in MPM simulations of granular column collapses, Acta Geotechnica 11 (3) (2016) 659–678.

[47] A. H. F. Neto, R. I. Borja, Continuum hydrodynamics of dry granular flows employing multiplicative elastoplasticity, Acta Geotechnica 13 (5) (2018) 1027–1040.

[48] H. H. Bui, K. Sako, R. Fukagawa, J. Wells, SPH-based numerical simulations for large deformation of geomaterial considering soil-structure interaction, in: The 12th International Conference of International Association for Computer Methods and Advances in Geomechanics (IACMAG), vol. 1, 570–578, 2008.

[49] R. Pramanik, D. Deb, Implementation of smoothed particle hydrodynamics for detonation of explosive with application to rock fragmentation, Rock Mechanics and Rock Engineering 48 (4) (2015) 1683–1698.

[50] Y. S. Shin, Ship shock modeling and simulation for far-field underwater explosion, Computers & Structures 82 (23-26) (2004) 2211–2219.

[51] J. Kim, H. Shin, Application of the ALE technique for underwater explosion analysis of a submarine liquefied oxygen tank, Ocean Engineering 35 (8-9) (2008) 812–822.

[52] Y. Wang, C. Liao, J. Wang, W. Wang, Numerical study for dynamic response of marine sediments subjected to underwater explosion, Ocean Engineering 156 (2018) 72–81.

[53] Z. Zhang, C. Wang, L. Wang, A. Zhang, V. V. Silberschmidt, Underwater explosion of cylindrical charge near plates: Analysis of pressure characteristics and cavitation effects, International Journal of Impact Engineering 121 (2018) 91–105.

[54] J. Swegle, S. Attaway, On the feasibility of using smoothed particle hydrodynamics for underwater explosion calculations, Computational Mechanics 17 (3) (1995) 151–168.

[55] M. Liu, G. Liu, K. Lam, Investigations into water mitigation using a meshless particle method, Shock Waves 12 (3) (2002) 181–195.

[56] X. H. Zhao, G. H. Wang, W. B. Lu, P. Yan, M. Chen, C. B. Zhou, Damage features of RC slabs subjected to air and underwater contact explosions, Ocean Engineering 147 (2018) 531–545.

[57] A. Zhang, W. Yang, C. Huang, F. Ming, Numerical simulation of column charge underwater explosion based on SPH and BEM combination, Computers & Fluids 71 (2013) 169–178.

[58] J. Y. Chen, F. S. Lien, Simulations for soil explosion and its effects on structures using SPH method, International Journal of Impact Engineering 112 (2018) 41–51.

[59] J. Y. Chen, C. Peng, F. S. Lien, Simulations for three-dimensional landmine detonation using the SPH method, International Journal of Impact Engineering 126 (2019) 40–49.

[60] G. R. Liu, M. B. Liu, Smoothed particle hydrodynamics: a meshfree particle method, World Scientific, 2003.

[61] F. Pacheco-Vázquez, J. Ruiz-Suárez, Impact craters in granular media: Grains against grains, Physical Review Letters 107 (21) (2011) 218001.

[62] J. Ellowitz, Head-on collisions of dense granular jets, Physical Review E 93 (1) (2016) 012907.

[63] P. A. Cundall, O. D. Strack, A discrete numerical model for granular assemblies, Geotechnique 29 (1) (1979) 47–65.

[64] T. Harada, S. Koshizuka, Y. Kawaguchi, Smoothed particle hydrodynamics on GPUs, in: Computer Graphics International, vol. 40, SBC Petropolis, 63–70, 2007.

[65] A. C. Crespo, J. M. Dominguez, A. Barreiro, M. Gómez-Gesteira, B. D. Rogers, GPUs, a new tool of acceleration in CFD: Efficiency and reliability on smoothed particle hydrodynamics methods, PloS One 6 (6) (2011) e20685.

[66] J. J. Monaghan, Simulating free surface flows with SPH, Journal of computational physics 110 (2) (1994) 399–406.

[67] S. Shao, E. Y. Lo, Incompressible SPH method for simulating Newtonian and non-Newtonian flows with a free surface, Advances in water resources 26 (7) (2003) 787–800.

[68] F. Fleissner, A. Lehnart, P. Eberhard, Dynamic simulation of sloshing fluid and granular cargo in transport vehicles, Vehicle system dynamics 48 (1) (2010) 3–15.

[69] P. W. Cleary, G. Savage, J. Ha, M. Prakash, Flow analysis and validation of numerical modelling for a thin walled high pressure die casting using SPH, Computational Particle Mechanics 1 (3) (2014) 229–243.

[70] Z. P. Wei, R. A. Dalrymple, A. Hérault, G. Bilotta, E. Rustico, H. Yeh, SPH modeling of dynamic impact of tsunami bore on bridge piers, Coastal Engineering 104 (2015) 26–42.

[71] H. N. Polwaththe-Gallage, S. C. Saha, E. Sauret, R. Flower, W. Senadeera, Y. Gu, SPH-DEM approach to numerically simulate the deformation of three-dimensional RBCs in non-uniform capillaries, Biomedical engineering online 15 (2) (2016) 161.

[72] M. Shadloo, G. Oger, D. Le Touzé, Smoothed particle hydrodynamics method for fluid flows, towards industrial applications: Motivations, current state, and challenges, Computers & Fluids 136 (2016) 11–34.

[73] J. J. Monaghan, An introduction to SPH, Computer Physics Communications 48 (1) (1988) 89–96.

[74] N. Frontiere, C. D. Raskin, J. M. Owen, CRKSPH–a conservative reproducing kernel smoothed particle hydrodynamics scheme, Journal of Computational Physics 332 (2017) 160–209.

[75] L. Zhan, C. Peng, B. Y. Zhang, W. Wu, Three-dimensional modeling of granular flow impact on rigid and deformable structures, Computers and Geotechnics 112 (2019) 257–271.

[76] J. J. Monaghan, Smoothed particle hydrodynamics, Reports on progress in physics 68 (8) (2005) 1703.

[77] M. B. Liu, Z. L. Zhang, D. L. Feng, A density-adaptive SPH method with kernel gradient correction for modeling explosive welding, Computational Mechanics .

[78] J. Gray, J. Monaghan, R. Swift, SPH elastic dynamics, Computer Methods in Applied Mechanics and Engineering 190 (49) (2001) 6641–6662.

[79] T. Rabczuk, T. Belytschko, S. P. Xiao, Stable particle methods based on Lagrangian kernels, Computer methods in applied mechanics and engineering 193 (12-14) (2004) 1035–1063.

[80] G. Oger, M. Doring, B. Alessandrini, P. Ferrant, An improved SPH method: Towards higher order convergence, Journal of Computational Physics 225 (2) (2007) 1472–1492.

[81] W. F. Chen, E. Mizuno, Nonlinear analysis in soil mechanics, Elsevier Amsterdam, 1990.

[82] W. Wu, D. Kolymbas, Numerical testing of the stability criterion for hypoplastic constitutive equations, Mechanics of Materials 9 (3) (1990) 245–253.

[83] X. T. Wang, W. Wu, An Updated Hypoplastic Constitutive Model, Its Implementation and Application, in: Bifurcations, Instabilities and Degradations in Geomaterials, Springer, 133–143, 2011.

[84] W. Wu, E. Bauer, A simple hypoplastic constitutive model for sand, International Journal for Numerical and Analytical Methods in Geomechanics 18 (12) (1994) 833–862.

[85] G. R. Johnson, W. H. Cook, A constitutive model and data for metals subjected to large strains, high strain rates and high temperatures, in: Proceedings of the 7th International Symposium on Ballistics, vol. 21, The Hague, The Netherlands, 541–547, 1983.

[86] J. H. Tillotson, Metallic equations of state for hypervelocity impact, Tech. Rep., GENERAL DYNAMICS SAN DIEGO CA GENERAL ATOMIC DIV, 1962.

[87] E. L. Lee, C. M. Tarver, Phenomenological model of shock initiation in heterogeneous explosives, The Physics of Fluids 23 (12) (1980) 2362–2372.

[88] D. Steinberg, Spherical explosions and the equation of state of water, Tech. Rep., Lawrence Livermore National Laboratory, CA (USA), 1987.

[89] P. Wang, A. Zhang, F. Ming, P. Sun, H. Cheng, A novel non-reflecting boundary condition for fluid dynamics solved by smoothed particle hydrodynamics, Journal of Fluid Mechanics 860 (2019) 81–114.

[90] W. Xie, T. Liu, B. Khoo, Application of a one-fluid model for large scale homogeneous unsteady cavitation: The modified Schmidt model, Computers & Fluids 35 (10) (2006) 1177–1192.

[91] R. Chandra, Parallel programming in OpenMP, Morgan kaufmann, 2001.

[92] B. Chapman, G. Jost, R. Van D P, Using OpenMP: portable shared memory parallel programming, vol. 10, MIT press, 2008.

[93] C. Wang, W. Xu, S. Yuen, Penetration of shaped charge into layered and spaced concrete targets, International Journal of Impact Engineering 112 (2018) 193–206.

[94] T. Vu-Bac, N L, X. Y. Zhuang, T. Nguyen-Thoi, T. Rabczuk, A software framework for probabilistic sensitivity analysis for computationally expensive models, Advances in Engineering Software 100 (2016) 19–31.

[95] K. M. Hamdia, M. Silani, X. Y. Zhuang, P. F. He, T. Rabczuk, Stochastic analysis of the fracture toughness of polymeric nanoparticle composites using polynomial chaos expansions, International Journal of Fracture 206 (2) (2017) 215–227.

[96] K. M. Hamdia, H. Ghasemi, X. Y. Zhuang, N. Alajlan, T. Rabczuk, Sensitivity and uncertainty analysis for flexoelectric nanostructures, Computer Methods in Applied Mechanics and Engineering 337 (2018) 95–109.

[97] G. Lube, H. E. Huppert, R. S. J. Sparks, A. Freundt, Collapses of two-dimensional granular columns, Physical Review E 72 (4) (2005) 041301.

[98] E. Roger, Mines buried in dry and saturated soils: blast experiments, soil modeling and simulations, Ph.D. thesis, Grenoble Alpes, 2015.

[99] F. V. Sirotkin, J. J. Yoh, A smoothed particle hydrodynamics method with approximate Riemann solvers for simulation of strong explosions, Computers & Fluids 88 (2013) 418–429.

[100] G. Chambers, H. Sandusky, F. Zerilli, K. Rye, R. Tussing, J. Forbes, Pressure measurements on a deforming surface in response to an underwater explosion in a water-filled aluminum tube, Shock and Vibration 8 (1) (2001) 1–7.

[101] G. R. Cowper, P. S. Symonds, Strain-hardening and strain-rate effects in the impact loading of cantilever beams, Tech. Rep., Brown University, Providence RI, 1957.

[102] S. Moriguchi, R. I. Borja, A. Yashima, K. Sawada, Estimating the impact force generated by granular flow on a rigid obstruction, Acta Geotechnica 4 (1) (2009) 57–71.

[103] Z. Shi, W. Li, H. Liu, F. Wang, Liquid-like wave structure on granular film from granular jet impact, AIChE Journal 63 (8) (2017) 3276–3285.

[104] R. I. Borja, C. Tamagnini, Cam-Clay plasticity Part III: Extension of the infinitesimal model to include finite strains, Computer Methods in Applied Mechanics and Engineering 155 (1-2) (1998) 73–95.

Appendix A

The derivation details of the discretized governing equations

A.1 Continuity equation

The continuity equation is

$$\frac{d\rho}{dt} = -\rho\frac{\partial v^\beta}{\partial x^\beta} \,. \tag{A.1}$$

As

$$\frac{\partial(\rho v^\beta)}{\partial x^\beta} = v^\beta\frac{\partial \rho}{\partial x^\beta} + \rho\frac{\partial v^\beta}{\partial x^\beta} \,, \tag{A.2}$$

the term on the RHS of Eq. (A.1) can be written as

$$-\rho\frac{\partial v^\beta}{\partial x^\beta} = v^\beta\frac{\partial \rho}{\partial x^\beta} - \frac{\partial(\rho v^\beta)}{\partial x^\beta} \,. \tag{A.3}$$

Using the SPH discretization equation for the function derivative,

$$\langle\nabla f(\boldsymbol{x}_i)\rangle = -\sum_{j=1}^{N} f(\boldsymbol{x}_j)\nabla W_{ij}\frac{m_j}{\rho_j} \,, \tag{A.4}$$

the two terms on the RHS of the Eq. (A.3) can be discretized as

$$-\frac{\partial(\rho_i v_i^\beta)}{\partial x_i^\beta} = \sum_{j=1}^{N}\rho_j v_j^\beta\frac{\partial W_{ij}}{\partial x_i^\beta}\frac{m_j}{\rho_j} \,, \tag{A.5}$$

$$v_i^\beta\frac{\partial \rho_i}{\partial x_i^\beta} = -v_i^\beta\sum_{j=1}^{N}\rho_j\frac{\partial W_{ij}}{\partial x_i^\beta}\frac{m_j}{\rho_j} \,. \tag{A.6}$$

Combining Eq. (A.5) and Eq. (A.6) yields

$$\frac{d\rho_i}{dt} = -\rho_i\frac{\partial v_i^\beta}{\partial x_i^\beta} = \sum_{j=1}^{N} m_j v_{ij}^\beta\frac{\partial W_{ij}}{\partial x_i^\beta} \,. \tag{A.7}$$

A.2 Momentum equation

The momentum equation is shown in the following,

$$\frac{dv^{\alpha}}{dt} = \frac{1}{\rho}\frac{\partial \sigma^{\alpha\beta}}{\partial x^{\beta}} \,. \tag{A.8}$$

With the Eq. (A.4), the summation form of the term on the RHS of the above equation can be obtained as

$$\frac{\partial \sigma_i^{\alpha\beta}}{\partial x_i^{\beta}} = \sum_{j=1}^{N} \frac{m_j}{\rho_j} \sigma_j^{\alpha\beta} \frac{\partial W_{ij}}{\partial x_i^{\beta}} \,. \tag{A.9}$$

Because

$$\nabla 1 = \sum_{j=1}^{N} \frac{m_j}{\rho_j} \frac{\partial W_{ij}}{\partial x_i^{\beta}} = 0 \,, \tag{A.10}$$

the term on the LHS of the following equation can be written as

$$\sum_{j=1}^{N} \frac{m_j}{\rho_j} \frac{\sigma_i^{\alpha\beta}}{\rho_i} \frac{\partial W_{ij}}{\partial x_i^{\beta}} = \frac{\sigma_i^{\alpha\beta}}{\rho_i} \sum_{j=1}^{N} \frac{m_j}{\rho_j} \frac{\partial W_{ij}}{\partial x_i^{\beta}} = 0 \,. \tag{A.11}$$

The discretized momentum equation can be obtained through combining Eq. (A.9) and Eq. (A.11)

$$\frac{dv_i^{\alpha}}{dt} = \sum_{j=1}^{N} m_j \frac{\sigma_i^{\alpha\beta} + \sigma_j^{\alpha\beta}}{\rho_i \rho_j} \frac{\partial W_{ij}}{\partial x_i^{\beta}} \,. \tag{A.12}$$

A.3 Energy equation

The following equation is the energy equation,

$$\frac{de}{dt} = \frac{\sigma^{\alpha\beta}}{\rho}\frac{\partial v^{\alpha}}{\partial x^{\beta}} \,. \tag{A.13}$$

Substituting the following formula to the Eq. (A.13),

$$\sigma^{\alpha\beta} = -p\delta^{\alpha\beta} + S^{\alpha\beta} \,, \tag{A.14}$$

the energy equation becomes

$$\frac{de}{dt} = \frac{-p}{\rho}\frac{\partial v^{\alpha}}{\partial x^{\alpha}} + \frac{S^{\alpha\beta}}{\rho}\frac{\partial v^{\alpha}}{\partial x^{\beta}} \,. \tag{A.15}$$

Since the shear stress $S^{\alpha\beta} = \mu\varepsilon^{\alpha\beta}$, in which μ is the viscosity, and $\varepsilon^{\alpha\beta}$ are the components of the shear strain rates. Consequently, the energy equation becomes

$$\frac{de}{dt} = \frac{-p}{\rho}\frac{\partial v^{\alpha}}{\partial x^{\alpha}} + \frac{\mu}{2\rho}\varepsilon^{\alpha\beta}\varepsilon^{\alpha\beta} \,. \tag{A.16}$$

Firstly,

$$\frac{-p}{\rho}\frac{\partial v^{\alpha}}{\partial x^{\alpha}} = \frac{p}{\rho^2}\frac{d\rho}{dt} \,, \tag{A.17}$$

Consider the function approximation of the continuity equation and Eq. (A.10) ,

$$\frac{d\rho}{dt} = -\rho_i \sum_{j=1}^{N} \frac{m_j}{\rho_j} v_j^{\beta} \frac{\partial W_{ij}}{\partial x_i^{\beta}} \,, \tag{A.18}$$

$$\sum_{j=1}^{N} \frac{m_j}{\rho_j} \frac{\partial W_{ij}}{\partial x_i^{\beta}} = 0 = \rho_i v_i^{\beta} \sum_{j=1}^{N} \frac{m_j}{\rho_j} \frac{\partial W_{ij}}{\partial x_i^{\beta}} \,, \tag{A.19}$$

Combining the two equations above yields

$$\frac{d\rho}{dt} = \rho_i \sum_{j=1}^{N} \frac{m_j}{\rho_j} v_{ij}^{\beta} \frac{\partial W_{ij}}{\partial x_i^{\beta}} \,. \tag{A.20}$$

Therefore, the term on the RHS of Eq. (A.17) can be rewritten as

$$\frac{p_i}{\rho_i^2}\frac{d\rho_i}{dt} = \frac{p_i}{\rho_i} \sum_{j=1}^{N} \frac{m_j}{\rho_j} v_{ij}^{\beta} \frac{\partial W_{ij}}{\partial x_i^{\beta}} \,, \tag{A.21}$$

As

$$\frac{\partial (pv^{\alpha})}{\partial x^{\alpha}} = p\frac{\partial v^{\alpha}}{\partial x^{\alpha}} + v^{\alpha}\frac{\partial p}{\partial x^{\alpha}} \,, \tag{A.22}$$

$$-p\frac{\partial v^{\alpha}}{\partial x^{\alpha}} = -\frac{\partial (pv^{\alpha})}{\partial x^{\alpha}} + v^{\alpha}\frac{\partial p}{\partial x^{\alpha}} \,. \tag{A.23}$$

Using the discretization of the function derivative, we can get

$$-\frac{p_i}{\rho_i}\frac{\partial v_i^{\alpha}}{\partial x_i^{\alpha}} = -\frac{1}{\rho_i} \sum_{j=1}^{N} \frac{m_j}{\rho_j} p_j v_j^{\beta} \frac{\partial W_{ij}}{\partial x_i^{\beta}} + \frac{v_i^{\beta}}{\rho_i} \sum_{j=1}^{N} \frac{m_j}{\rho_j} p_j \frac{\partial W_{ij}}{\partial x_i^{\beta}} \,. \tag{A.24}$$

Therefore, adding Eq. (A.21) and Eq. (A.24) together yields the discretized energy equation

$$\frac{\mathrm{d}e_i}{\mathrm{d}t} = \frac{1}{2} \sum_{j=1}^{N} m_j \frac{p_i + p_j}{\rho_i \rho_j} v_{ij}^{\beta} \cdot \frac{\partial W_{ij}}{\partial x_i^{\beta}} + \frac{1}{2\rho_i} S_i^{\alpha\beta} \varepsilon_i^{\alpha\beta} \,. \tag{A.25}$$

Appendix B

Kernel gradient correction

For the 2D problem, the gradient of a field function $f(\boldsymbol{x})$ can be represented as [40]

$$\nabla f(\boldsymbol{x}) = \nabla f(\boldsymbol{x}) - \nabla 1 \ . \tag{B.1}$$

The equation above can be approximated by using the kernel function,

$$\langle \nabla f(\boldsymbol{x}) \rangle = \int_{\Omega} f(\boldsymbol{x}') \nabla W d\boldsymbol{x}' - f(\boldsymbol{x}) \int_{\Omega} \nabla W d\boldsymbol{x}' \ . \tag{B.2}$$

The second-order Taylor expansion of the first term on the RHS is given by

$$\int_{\Omega} f(\boldsymbol{x}') \nabla W d\boldsymbol{x}' = f(\boldsymbol{x}) \int_{\Omega} \nabla W d\boldsymbol{x}' + \left(\int_{\Omega} (\boldsymbol{x}' - \boldsymbol{x}) \otimes \nabla W d\boldsymbol{x}' \right) \nabla f(\boldsymbol{x}) + \mathrm{O}\left(h^2\right) \ , \tag{B.3}$$

Substituting Eq. (B.3) to Eq. (B.2) yields

$$\langle \nabla f(\boldsymbol{x}) \rangle = \left(\int_{\Omega} (\boldsymbol{x}' - \boldsymbol{x}) \otimes \nabla W d\boldsymbol{x}' \right) \nabla f(\boldsymbol{x}) + \mathrm{O}\left(h^2\right) \ . \tag{B.4}$$

From Eq. (B.4), we can find that the kernel approximation of the gradient of $f(\boldsymbol{x})$ is second-order accurate if the following requirement can be satisfied.

$$\int_{\Omega} (\boldsymbol{x}' - \boldsymbol{x}) \otimes \nabla W d\boldsymbol{x}' = \begin{pmatrix} 1 & 0 \\ 0 & 1 \end{pmatrix} \ . \tag{B.5}$$

In order to confirm the C^1 consistency in SPH, the Eq. (B.5) should be satisfied in discrete particle approximation. Therefore, the corrected kernel gradient $\nabla_i^C W_{ij}$ is employed to achieve the requirement above.

$$\sum_{j=1}^{N} \left(\boldsymbol{x_j} - \boldsymbol{x_i} \right) \otimes \nabla_i^C W_{ij} \frac{m_j}{\rho_j} = \begin{pmatrix} 1 & 0 \\ 0 & 1 \end{pmatrix} \ , \tag{B.6}$$

where the $\nabla_i^C W_{ij} = \boldsymbol{L}(\boldsymbol{x_i})\nabla_i W_{ij}$. The renormalization matrix $\boldsymbol{L}(\boldsymbol{x_i})$ is in the following form.

$$L(r_i) = \begin{pmatrix} \sum_{j=1}^{N} x_{ji} \frac{\partial W_{ij}}{\partial x_i} \frac{m_j}{\rho_j} & \sum_{j=1}^{N} x_{ji} \frac{\partial W_{ij}}{\partial y_i} \frac{m_j}{\rho_j} \\ \sum_{j=1}^{N} y_{ji} \frac{\partial W_{ij}}{\partial x_i} \frac{m_j}{\rho_j} & \sum_{j=1}^{N} y_{ji} \frac{\partial W_{ij}}{\partial y_i} \frac{m_j}{\rho_j} \end{pmatrix}^{-1} . \tag{B.7}$$

The employment of the corrected kernel gradient in Eq. (B.7) ensures the C^1 consistency in the SPH method. The $\boldsymbol{L}(\boldsymbol{x_i})$ for 3D problems can be derived in the same manner.

Appendix C

Essentials of continuum mechanics

The deformation can be presented by giving the path of every particle X.

$$\boldsymbol{x} = \boldsymbol{x}(X, t) \ . \tag{C.1}$$

The velocity can be represented in terms of spatial coordinates and the time.

$$v_i = v_i(x_1, x_2, x_3, t) \ . \tag{C.2}$$

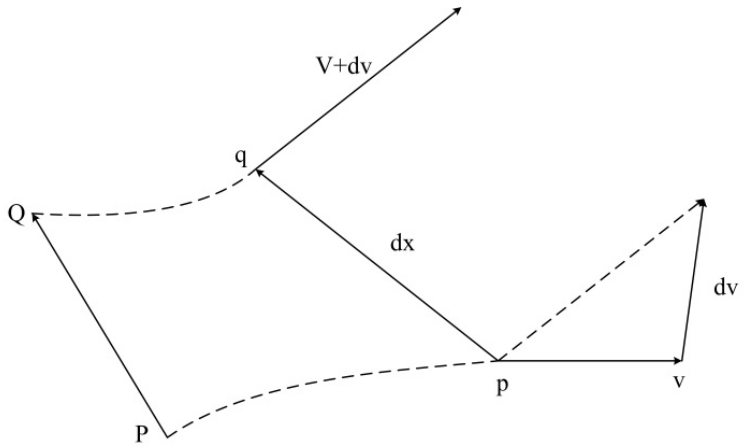

Figure C.1 The relative velocity of particle Q at point q to particle P at point p.

As can be seen from Fig. C1, the relative velocity at particle P relative to particle Q are given by

$$dv_i = \frac{\partial v_i}{\partial x_j} dx_j \ . \tag{C.3}$$

Therefore,

$$\boldsymbol{dv} = \boldsymbol{L} \cdot \boldsymbol{dx} \ , \tag{C.4}$$

in which L is termed as the spatial gradients of velocity.

$$\boldsymbol{L} = \boldsymbol{D} + \boldsymbol{W} \,, \tag{C.5}$$

$$\boldsymbol{D} = \frac{1}{2}(\boldsymbol{L} + \boldsymbol{L}^T) \,, \tag{C.6}$$

$$\boldsymbol{W} = \frac{1}{2}(\boldsymbol{L} - \boldsymbol{L}^T) \,. \tag{C.7}$$

$L_{km} = v_{k,m}$ can be divided into two parts: a symmetric tensor $\boldsymbol{D}$ called the rate of deformation tensor or the stretching tensor, a skew-symmetric tensor $\boldsymbol{W}$ called the spin tensor or vorticity tensor.

Appendix D

Incremental plastic strain derivation

The incremental plastic strain can be obtained by subtracting the deviatoric part of the elastic strain increment $\frac{1}{2G}(S_{ij}^{n+1} - S_{ij}^{R^n})$ from the total deviatoric increment $\Delta\varepsilon_{ij}^{'}$, i.e.,

$$\Delta\varepsilon_{ij}^{p} = \Delta\varepsilon_{ij}^{'} - \frac{1}{2G}(S_{ij}^{n+1} - S_{ij}^{R^n}) \,, \tag{D.1}$$

$$\Delta\varepsilon_{ij}^{'} = \frac{{}^{*}S_{ij}^{n+1} - S_{ij}^{R^n}}{2G} \,, \tag{D.2}$$

where $*$ denotes a trial stress value. Substituting Eq. (D.1) to Eq. (D.2), we can obtain

$$\Delta\varepsilon_{ij}^{p} = \frac{{}^{*}S_{ij}^{n+1} - S_{ij}^{n+1}}{2G} \,. \tag{D.3}$$

$S^{*} = \left(\frac{3}{2}{}^{*}S_{ij}^{n+1}{}^{*}S_{ij}^{n+1}\right)^{\frac{1}{2}}$ is defined as the effective trial stress. Substituting the following equation

$$S_{ij}^{n+1} = \frac{\sigma_y}{S^{*}}{}^{*}S_{ij}^{n+1} = m^{*}S_{ij}^{n+1} \tag{D.4}$$

into Eq. (D.3) gives

$$\Delta\varepsilon_{ij}^{p} = \left(\frac{1-m}{2G}\right){}^{*}S_{ij}^{n+1} = \left(\frac{1-m}{2Gm}\right)S_{ij}^{n+1} = d\lambda S_{ij}^{n+1} \,. \tag{D.5}$$

The definition of an increment in the effective plastic strain is

$$\Delta\varepsilon^{p} = \left(\frac{2}{3}\Delta\varepsilon_{ij}^{p}\Delta\varepsilon_{ij}^{p}\right)^{\frac{1}{2}} \,. \tag{D.6}$$

Squaring both sides of Eq. (D.5) leads to

$$\Delta\varepsilon_{ij}^{p}\Delta\varepsilon_{ij}^{p} = \left(\frac{1-m}{2G}\right)^{2}{}^{*}S_{ij}^{n+1}{}^{*}S_{ij}^{n+1} \,. \tag{D.7}$$

From Eq. (D.6)

$$\frac{3}{2}(\Delta\varepsilon^p)^2 = \left(\frac{1-m}{2G}\right)^2 \frac{2}{3}(S^*)^2\,, \tag{D.8}$$

we can obtain that

$$\Delta\varepsilon^p = \frac{1-m}{3G}S^* = \frac{S^* - \sigma_y}{3G}\,. \tag{D.9}$$

Therefore, the incremental plastic strain can be calculated through Eq. (D.9) conveniently.

Appendix E

The derivation of the proportionality factor

In order to use the Eq. (3.10), the change rate of the plastic multiplier $\dot{\lambda}_i$ must be determined. During plastic deformation, $f(\sigma^{\alpha\beta}) = 0$ is satisfied. Therefore, the total derivative of function f is

$$df = \frac{\partial f}{\partial \sigma^{\alpha\beta}} d\sigma^{\alpha\beta} = 0 \,. \tag{E.1}$$

This is known as the consistent condition for the perfectly plastic material. Then we can get the following equation based on Eq. (E.1),

$$f(\sigma^{\alpha\beta} + d\sigma^{\alpha\beta}) = f(\sigma^{\alpha\beta}) + df = f(\sigma^{\alpha\beta}) \,. \tag{E.2}$$

The premise of perfectly plastic constitutive relations assumes that the materials can undergo small plastic as well as elastic strains at each loading increment. Then the total strain increment tensor can be obtained by combining elastic with plastic strain.

$$\dot{\varepsilon}^{\alpha\beta} = \dot{\varepsilon}_e^{\alpha\beta} + \dot{\varepsilon}_p^{\alpha\beta} = \frac{\dot{S}^{\alpha\beta}}{2G} + \frac{1-2\mu}{3E}\dot{\sigma}^{\gamma\gamma}\delta^{\alpha\beta} + \dot{\lambda}\frac{\partial g}{\partial \sigma^{\alpha\beta}} \,. \tag{E.3}$$

E is the Young's modulus, K is the elastic bulk modulus, and G is the elastic shear modulus.

$$K = \frac{E}{3(1-2\mu)} \,, \tag{E.4}$$

$$G = \frac{E}{2(1+\mu)} \,. \tag{E.5}$$

The equation above can be rewritten by replacing $\dot{I}_1 = \dot{\sigma}^{\gamma\gamma}$.

$$\dot{\varepsilon}^{\alpha\beta} = \frac{\dot{S}^{\alpha\beta}}{2G} + \frac{\dot{I}_1}{9K}\delta^{\alpha\beta} + \dot{\lambda}\frac{\partial g}{\partial \sigma^{\alpha\beta}} \,. \tag{E.6}$$

Substituting $\dot{\sigma}^{\alpha\beta} = \dot{S}^{\alpha\beta} + \frac{1}{3}\dot{\sigma}^{\gamma\gamma}\delta^{\alpha\beta}$ to Eq. (E.6), the stress-strain relationship can be obtained as

$$\dot{\varepsilon}^{\alpha\beta} = \left(\frac{\dot{\sigma}^{\alpha\beta} - \frac{1}{3}\dot{\sigma}^{\gamma\gamma}\delta^{\alpha\beta}}{2G} + \frac{\dot{I}_1}{9K}\delta^{\alpha\beta}\right) + \dot{\lambda}\frac{\partial g}{\partial \sigma^{\alpha\beta}} \,. \tag{E.7}$$

Rearrange the above equation,

$$\dot{\sigma}^{\alpha\beta} = 2G\dot{\varepsilon}^{\alpha\beta} - 2G\dot{\lambda}\frac{\partial g}{\partial \sigma^{\alpha\beta}} + \frac{3K - 2G}{9K}\dot{I}_1\delta^{\alpha\beta} \,. \tag{E.8}$$

Multiply both sides of Eq. (E.8) by $\delta^{\alpha\beta}$ yields

$$\left(\dot{\varepsilon}^{\alpha\beta} - \dot{\lambda}\frac{\partial g}{\partial \sigma^{\alpha\beta}}\right)\delta^{\alpha\beta} = \frac{\left(\dot{\sigma}^{\alpha\beta} - (\dot{I}_1/3)\delta^{\alpha\beta}\right)\delta^{\alpha\beta}}{2G} + \frac{\dot{I}_1}{3K}\delta^{\alpha\beta}\delta^{\alpha\beta} \,. \tag{E.9}$$

Therefore,

$$\dot{I}_1 = 3K\left(\dot{\varepsilon}^{\gamma\gamma} - \dot{\lambda}\frac{\partial g}{\partial \sigma^{\alpha\beta}}\delta^{\alpha\beta}\right) \,. \tag{E.10}$$

The substitution of Eq. (E.10) into Eq. (E.8) gives

$$\dot{\sigma}^{\alpha\beta} = 2G\dot{e}^{\alpha\beta} + K\dot{\varepsilon}^{\gamma\gamma}\delta^{\alpha\beta} - \dot{\lambda}\left(\left(K - \frac{2G}{3}\right)\frac{\partial g}{\partial \sigma^{mn}}\delta^{mn}\delta^{\alpha\beta} + 2G\frac{\partial g}{\partial \sigma^{\alpha\beta}}\right) \,. \tag{E.11}$$

If the material is isotropic, the yield function can be expressed as: $f(I_0, \sqrt{J_2}, (J_3)^{1/3}) = 0$. For Drucker-Prager model, the yielding and plastic potential relations are generally given by the following equations.

$$f(\sigma^{\alpha\beta}) = F(I_1, \sqrt{J_2}) - K = 0 \,, \tag{E.12}$$

$$g(\sigma^{\alpha\beta}) = G(I_1, \sqrt{J_2}) - K = 0 \,. \tag{E.13}$$

The derivative of these functions with respect to the stress tensor can be obtained as follows:

$$\frac{\partial f}{\partial \sigma^{\alpha\beta}} = \frac{\partial f}{\partial I_1}\frac{\partial I_1}{\partial \sigma^{\alpha\beta}} + \frac{\partial f}{\partial \sqrt{J_2}}\frac{\partial \sqrt{J_2}}{\partial \sigma^{\alpha\beta}} = \frac{\partial f}{\partial I_1}\delta^{\alpha\beta} + \frac{1}{2\sqrt{J_2}}\frac{\partial f}{\partial \sqrt{J_2}}S^{\alpha\beta} \,, \tag{E.14}$$

$$\frac{\partial g}{\partial \sigma^{\alpha\beta}} = \frac{\partial g}{\partial I_1}\frac{\partial I_1}{\partial \sigma^{\alpha\beta}} + \frac{\partial g}{\partial \sqrt{J_2}}\frac{\partial \sqrt{J_2}}{\partial \sigma^{\alpha\beta}} = \frac{\partial g}{\partial I_1}\delta^{\alpha\beta} + \frac{1}{2\sqrt{J_2}}\frac{\partial g}{\partial \sqrt{J_2}}S^{\alpha\beta} \,. \tag{E.15}$$

Substituting Eq. (E.14) and Eq. (E.15) into Eq. (E.11) leads to

$$\dot{\sigma}^{\alpha\beta} = 2G\dot{e}^{\alpha\beta} + K\dot{\varepsilon}^{\gamma\gamma}\delta^{\alpha\beta} - \dot{\lambda}\left(3K\frac{\partial g}{\partial I_1}\delta^{\alpha\beta} + \frac{G}{\sqrt{J_2}}\frac{\partial g}{\partial \sqrt{J_2}}S^{\alpha\beta}\right) \,, \tag{E.16}$$

The $\dot{\lambda}$ can also be obtained through substituting Eq. (E.11) into Eq. (E.1).

$$\dot{\lambda} = \frac{3K\dot{\varepsilon}^{\gamma\gamma}\frac{\partial f}{\partial I_1} + \frac{G}{\sqrt{J_2}}\frac{\partial f}{\partial \sqrt{J_2}}S^{mn}\dot{\varepsilon}^{mn}}{9K\frac{\partial f}{\partial I_1}\frac{\partial g}{\partial I_1} + G\frac{\partial f}{\partial \sqrt{J_2}}\frac{\partial g}{\partial \sqrt{J_2}}} \,. \tag{E.17}$$

The yield function in soil model of the thesis is expressed based on the modified Von Mises criterion,

$$f(I_1, J_2) = \sqrt{J_2} + \alpha I_1 - k_c \ . \tag{E.18}$$

If the plastic flow rule is associated, then the plastic potential function of Drucker-Prager model is the same as yield function form.

$$g(I_1, J_2) = \sqrt{J_2} + \alpha I_1 - k_c \ . \tag{E.19}$$

Substituting equation Eq. (E.18) and Eq. (E.19) into Eq. (E.17), then we can get the change rate of the plastic multiplier,

$$\dot{\lambda} = \frac{3\alpha_\phi K \dot{\varepsilon}^{\gamma\gamma} + (G/\sqrt{J_2}) S^{\alpha\beta} \dot{\varepsilon}^{\alpha\beta}}{9\alpha_\phi^2 K + G} \ . \tag{E.20}$$